Determination of Diffusion Mechanisms in Battery Materials using Quasi-Elastic Neutron Scattering Techniques

Toby James Willis

ROYAL HOLLOWAY COLLEGE
UNIVERSITY OF LONDON

A DISSERTATION SUBMITTED TO THE UNIVERSITY OF LONDON
FOR THE DEGREE OF DOCTOR OF PHILOSOPHY

August 2016

Declaration of Authorship

I, Toby James Willis, hereby declare that this thesis and the work presented in it is entirely my own. Where I have consulted the work of others, this is always clearly stated.

Signed: ____________________

Date: ____________________

Abstract

The diffusion of ions within a battery material is inherently important to its capacity to charge and discharge electrons through a circuit during its normal operation. Understanding the pathways ions use to diffuse within a crystal structure, identifying where the barrier to movement is small, can inform the direction of future battery research. Two crystalline materials, $Na_{0.8}CoO_2$ and $Li_{0.29}La_{0.57}TiO_3$, have been studied using a combination of experimental and computational techniques due to their promising characteristics.

Na_xCoO_2 is closely related to the commercially dominant Li_xCoO_2 cathode material. They are intercalation materials with rigid CoO_2 layers that the Na or Li ions can diffuse between. The effect of ordering of the Na ions within a layer on the diffusion rate has been studied with molecular dynamics simulations by first principles density functional theory calculations using CASTEP. Clustering of ions is observed to enhance the diffusion rate by opening up short range pathways with a greatly reduced energy barrier to diffusion. The diffusion rate of $Na_{0.8}CoO_2$ was measured using quasi-elastic neutron scattering with the signal varying according to the self-correlation function, effectively providing a value for the average time an ion stays in one site between 'hops'.

$Li_{0.29}La_{0.57}TiO_3$ is a solid electrolyte with ionic conduction rates equivalent to liquid and polymer based systems. The use of a solid electrolyte has significant advantages, particularly its improved stability and safety. Using single crystal X-ray diffraction, structures of several crystals have been identified, including a completely novel Ruddlesden-Popper structure previously unreported in literature. Quasi-elastic neutron scattering over a large temperature range is used to measure the diffusion rate and activation energy. The hopping geometry is found to be consistent with the predictions of molecular dynamics simulations.

Acknowledgements

I am thankful for the opportunities I have had during my PhD. I have been able to carry out important and interesting research at Royal Holloway, ISIS and the ILL within a supportive and friendly group. The majority of my gratitude must go to my supervisor, Jon Goff, for his guidance and insight. I also owe a lot to Keith Refson who provided valuable teaching and insight into the use of DFT calculations, without which this thesis would not have been possible. I must thank Ross Stewart, my supervisor at ISIS, for his valuable discussions which helped advance my knowledge of neutron scattering.

The crystals my research was dependent upon were grown by Sivaperumal Uthayakumar. With you responsible I have known that I will always receive the highest quality samples. Thank you for your friendship and for taking the time to explain crystal growth to me.

My experiments at ISIS and the ILL have depended upon highly skilled instrument scientists. First and foremost, I would like to thank Franz Demmel for his help on OSIRIS with my two most important experiments. I would also like to thank Matthias Gutmann and Rob Bewley at ISIS, and Peter Fouquet and Dirk Honecker at the ILL.

From the start, Dan Porter and David Voneshen have helped me incredibly with their useful discussions and gentle tutoring, particularly in the first year or two of my PhD. Without Dan's training and support I would be a far less competent physicist. Without Dave to constantly ask ”does this make sense?” I would be buried under equations and theories.

To all of the PhD students I have come to know at Royal Holloway, it has been a pleasure. To James especially, thank you for putting up with me in the flat for so long! To David, thank you for enlightening me about the coming revolution and our other

political discussions. To Tom, Eron, Katie, Pardis, Rupert, Alex, Tim and everyone else, thank you for interesting chats at teatime and friendly games in the evening.

Finally, I would like to thank my friends and family for supporting me over the last 4 years. There have been some tough times, particularly during this last year, so it's great to know I have so many people I can depend upon. My parents especially deserve credit for their continual support, I'm sure that you can rest easy now I have a 'real' job!

Contents

List of Figures

List of Tables

1 Background

1.1 Battery Materials

The demand for portable energy storage has greatly increased with advances in technology. The key requirements are for stability, re-usability and energy density. Ionic batteries are the only realistic solution to this problem, with extensive research aimed at improving their characteristics. Lithium ion batteries dominate the market for portable devices [1] due to their unmatched combination of high energy and power density [2].

There is demand for better performance batteries for portable electronics with, for example, improved cyclability and safety. Furthermore, electric vehicles will require a large increase in battery production. Renewable energy industries, such as solar and wind power, will require energy storage on a much larger scale. Currently pumped hydro storage accounts for 99% of the total installed energy storage, however it has a very high capital cost, requires special geographic sites and has a very low energy density. Li-ion battery is considered a major candidate in future large-scale energy storage systems due to their high energy and power density, although has significant disadvantages such as high initial cost and requirement for sophisticated balance and charge control management[3].

Other potential systems particularly for medium scale usage, such as vehicles, includes fuel cells which are gaining popularity due to their high efficiency, cleanliness and cost-effective supply of power[4]. In comparison to Li-ion batteries, although a significant advantage of the hydrogen fuel cell is its energy density, meaning that a power pack can be smaller and lighter, they also have a much lower operating voltage of around 1.2V[5]. A significant problem is also the necessity to store hydrogen under high pressures to achieve high energy densities. Metal organic frameworks are considered appealing due to their high surface areas which facilitate the reversible adsorption of H_2 without the necessity of keeping the low density gas under pressure. Unfortunately there is a limitation, wherein the largest surface areas correspond to the heaviest MOF structures and therefore there is a trade-off between the volumetric and gravimetric capacities[6]. Hydrogen fuel cells continue to form an interesting an viable alternative to battery materials with significant advantages and disadvantages, but are not yet at a stage of maturation to replace Li-ion batteries in most situations.

However, further development of replacement systems is spurred on by the impending shortages of lithium [7]. Even if supply can keep up with demand [8], the price of Li is expected to multiply a factor of five between 2010 and 2020 [9]. Further complications occur as Li reserves are geographically more concentrated than oil which creates a considerable risk to societal infrastructure, which leads to a strong recommendation by Kushnir et al[10]. that alternatives are brought up to competitive readiness to mitigate this risk. Replacements will need an equivalent magnitude of capacity. The increased use of batteries in large scale static power storage devices, in conjunction with local and national power grids, opens up the possibility for cheaper battery materials with lower energy densities.

A battery can be divided simply into three separate parts; the anode, the cathode and the electrolyte. The anode and cathode are connected via an electrolyte which allows the movement of ions but inhibits the movement of electrons. When a circuit external to the electrolyte is connected, Figure 1, the anode oxidises and electrons move through the device, powering it, towards the cathode. In response, positive ions migrate across the electrolyte from the anode towards the cathode. If a power supply is inserted in place of the device, the system charges causing the cathode to oxidise and ions to migrate into the anode.

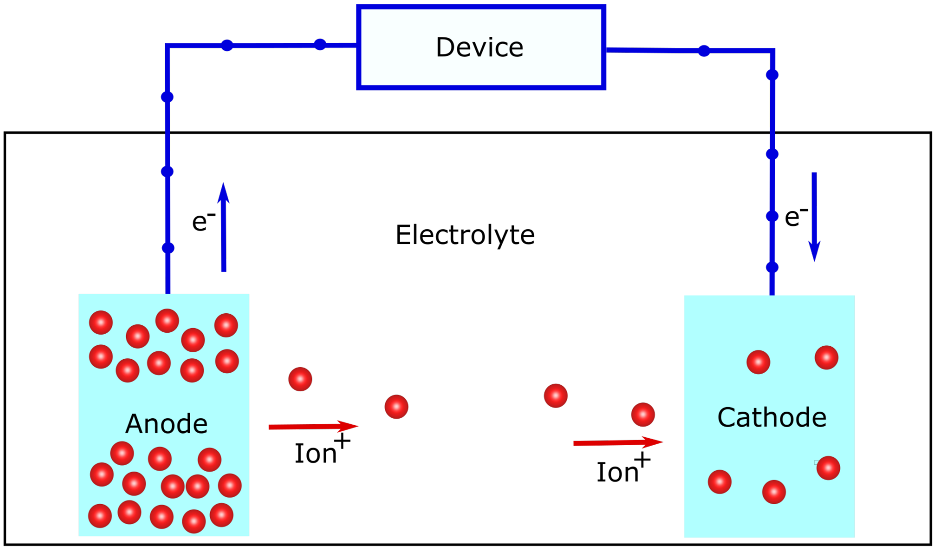

Figure 1: A layout of a simple rechargeable battery, with electrons discharging across a device between the anode and cathode. In response positive ions, red circles, migrate from the anode to the cathode material.

The key consideration for a battery system is how much energy it can store which is generally considered either in terms of the energy density per mass unit or the energy density per volume unit. There are three main electrochemical reactions used in ionic batteries to store energy. In the first two, energy is stored by alloying a material and by conversion, however despite their good capacities they are often not used due to their large volume expansion and irreversibility, respectively [11]. The third reaction is via intercalation which involves inserting ions into a solid host material. The suitability of the host material is decided by its ability to absorb electrons and ions, i.e. change valence states, and the availability of sites to store the intercalating ions.

The energy density of a rechargeable battery is determined by the specific capacity of the electrodes and the differential potential between them. This potential corresponds to the open circuit voltage which depends upon the electrochemical potentials of the anode and cathode materials. The choice of electrolyte also plays a role as they have a usable voltage range, called the electrolyte window, and any charge/discharge outside of this window will result in the formation of a surface layer [12]. The ionic conduction of a material is inherently linked to the diffusion. Determining the mechanisms that result in the fast uninhibited movement of ions in novel materials will identify those with the highest current output and will allow for the prediction of future materials.

1.1.1 Li Battery Materials

Li_xCoO_2 is the first and commercially most successful intercalation material used as a transition-metal-oxide (TMO) battery electrode. The layering of the compound is labelled according to the Delmas notation [13]. O3-Li_xCoO_2 consists of a repeating stack of three octahedral LiO_6 layers, shown in Figure 2a. The structure has trigonal symmetry with the Li ions able to move easily between the 2D planes and is considered to be very reversible as the CoO_2 layers maintain their structure for a wide range of Li concentrations.

The cathode material is considered the limiting factor in the capacity of a battery and, therefore, this is the focus of the majority of current research. A common anode material is graphite which has a high theoretical specific charge of 372 mAh/g [14]. In comparison, Li_xCoO_2 has a theoretical specific capacity of 274 mAh/g [2]. Li_xCoO_2 was originally introduced in 1980 by Mizushima et al. [15]. Research since then has been focussed on finding materials with equivalent or higher capacities, while improving the thermal stability, recyclability and cost.

A variety of substitutions have been considered in place of the Co, for example Li_xNiO_2 [16] and Li_xMnO_2 [17] which have equivalent theoretical specific capacities of 275 and 285 mAh/g, respectively. Both of these materials have tendencies for the tran-

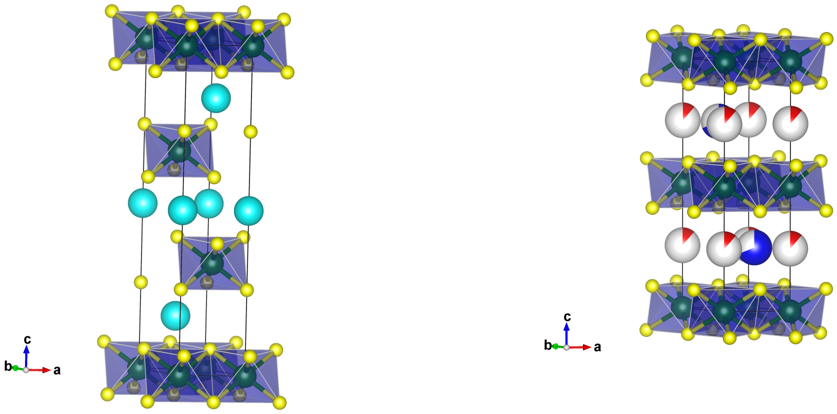

(a) Unit cell of O3-$LiCoO_2$.

(b) Unit cell of P2-$Na_{0.8}CoO_2$.

Figure 2: The widely used battery material O3-$LiCoO_2$, a), contains three octahedral LiO_6 layers per repetition unit perpendicular to the layers, while the related P2-$Na_{0.8}CoO_2$, b), contains two prismatic NaO_6 layers per repetition unit perpendicular to the layers, according to the Delmas notation [13]. Polyhedra are drawn around the CoO tetrahedra, with the Co coloured green and the O coloured yellow. In a) the Li ions are coloured pale blue while in b) the Na ions are coloured either red or blue dependent on whether they are in a high or low energy site, respectively. The high energy site in b) is occupied only when the total Na concentration per formula unit is < 1.

sition metal to drift into the Li plane during Li extraction changing the overall structure [18], which significantly effects reversibility. To improve the stability of these materials it was found that doping with different transition metals helped. $Li_xNi_{0.8}Co_{0.15}Al_{0.05}O_2$ has a capacity equivalent to Li_xCoO_2 at 279 mAh/g and greater stability than Li_xNiO_2 which has ensured its commercial success.

Research is also aimed at finding novel suitable electrolyte materials. A key consideration can be the ionic diffusion rate which has an effect on charge and discharge rates. For this reason common electrolytes are liquid based. Unfortunately there are inherent safety concerns using liquids as they may leak if the battery becomes damaged and the solutions can be corrosive. A general review of the electrolytes for Li based batteries is contained in Ref. [19]. One particular compound, $LiLaTiO_3$, shows great promise and has been studied greatly. At certain Li concentrations the diffusion rate is equivalent to liquid and polymer based systems [20].

Fast diffusion depends on the level of ordering within the system. The ionic conductivity has been studied with respect to the shared La/Li site [21] and it was found that the ordering negatively affected the conductivity. It has been suggested that the TiO_6 octahedra may deform and tilt opening up channels that would influence the Li ionic conductivity [22].

1.1.2 Na battery materials

Na^+ is a possible replacement for Li^+ ion [23]; it has a higher natural abundance than Li bringing down production costs. The Na^+ redox potential, $E^o_{(\mathrm{Na+/Na})}$ = -2.71 V, is only 0.3 V above lithium[24] which, combined with the heavier nucleus of Na, means that the energy densities are typically lower. However, Na may find a role in large scale energy storage and level loading where it is not necessary to physically move the material. Where the energy density is crucial, such as in microelectronics [25], Li will most likely still dominate. However, some Na ion batteries are approaching the energy densities of mainstream Li technology and, therefore, may be economically viable with costs expected to be at least 10% cheaper [26].

Initially Na battery materials were restricted to high temperatures, for example the NASICON materials [27]. Over time research into new materials has allowed them to operate at room temperature. Gains have particularly been made in the field of Na TMO's which follow the formula Na_xMO_2 where M is one or more transition metals.

A variety of Na TMO's are discussed as cathodes in a recent review article [28] as well as Na ion batteries in general [24, 29]. Electrochemical studies have been carried out on various compounds including $Na_{2/3}Mn_yCo_{1-y}O_2$ [30], $Na_xNi_{1/3}Co_{1/3}Fe_{1/3}O_2$ [31], $Na_xNi_{1/3}Fe_{1/3}Mn_{1/3}O_2$ [32], as well as $Na_{0.67}Fe_{0.5}Mn_{0.5}O_2$ which was found to have an energy density comparable to LiFePO4 [33]. Anode materials are discussed in [26].

Na_xCoO_2 is another viable TMO cathode material that has generated great interest [30, 34, 35]. Unlike the Li_xCoO_2 system, Na_xCoO_2 forms a P2-structure which has a repeating stack of two prismatic NaO_6 layers, Figure 2b. There are two energetically inequivalent sites for the Na ions; which, for compositions of $x < 1$ [36], allows the formation of a kaleidoscope of superstructures as Na ions spread out effectively in the layers. A useful comparison of Na TMO capacities can be found in [37] with a key figure shown in Figure 3. There is significant room for improvement in Na TMO capacities given the greater capacities of Li based materials (large right hand ellipse). The relatively small difference in standard potential between Li^+ and Na^+ results in only a small theoretical drop, as shown by the dashed ellipse. The structural dependence of the Na concentration has been investigated electrochemically [38] as well as by *in situ* X-ray [39] and de-intercalation by Bromine [40]. The concentration dependence has been discussed in relation to diffusion within the compound [41, 42, 43]. The properties of Na_xCoO_2 have been improved by using doped compositions, for example Ca doped [44] and Mn doped [45].

1.2 Solid State Diffusion

Solid state diffusion concerns the movement of ions within a fixed crystal structure. At temperatures far below the melting point of a crystal, ions may make non-periodic stochastic movements from one stable position to another. The temperature of the

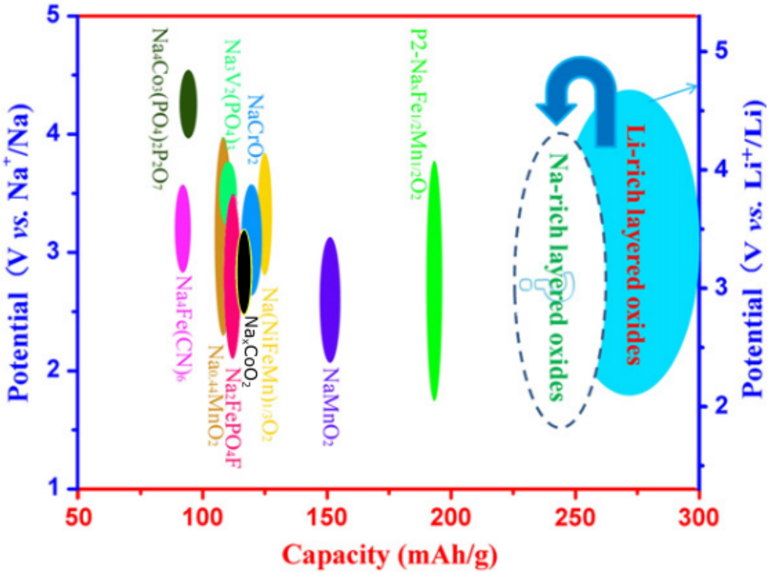

Figure 3: Comparison of the potentials of different Na based TMO compounds vs. their reversible capacities, created by Jian et al.[37]. Na_xCoO_2 is displayed in black. For reference, a region giving the potentials and reversible capacities of typical Li-rich layered oxides is outlined along with the optimal region for Na-rich layered oxides.

crystal will give rise to a distribution of ionic energies that are typically expressed via phonons and other displacements. An ion site is a potential energy well, so any movement away from the equilibrium position results in a restoring force. If an ion has sufficient energy that it can overcome the barrier between neighbouring sites, then a hop becomes possible.

The activation energy of a hop will be influenced by the general structure of the crystal; how closely packed the ions are, the presence of natural channels or planes for movements and the effect of vacancies in the material, causing variations in the local environment. The packing of the ions will be determined by the scale of their ionic radius and the strength of bonding present. Na_xCoO_2 and Li_xCoO_2 are examples of crystal structures that have a layered structure. The bonds between layers are weak and therefore the Na ions move within this layer but are prohibited from moving perpendicular to layers. Similarly in a $LiLaTiO_3$ crystal, the presence of the much larger La distorts the TiO_6 octahedra lowering the energy of some channels, reducing the barrier to Li migration.

For some structures diffusion can only occur when vacancies are present; if all sites are occupied within the crystal lattice then ions are unable to move. Typically this is because any possible interstitial sites are too close to neighbouring sites to allow their occupation. If vacancies are introduced onto the sites of the hopping species then immediately the neighbouring ions have somewhere to hop to.

1.2.1 Stochastic Diffusion

The diffusion of ions can be described as being stochastic, meaning that a probability distribution can be created to describe the development of the system with time. For solid state diffusion it is necessary to identify a set of all possible states. The probability of a single process is described by $\mathrm{P}_1(a_1t_1)$, where process a_1 occurs at time t_1. Joint probabilities can be used to describe each possible sequence of states: $\mathrm{P}_n(a_1t_1;...;a_nt_n)$, where a_1 occurs at time t_1, followed by a_2 occuring at t_2, and so on. A complete description can be found in the book of Hempelmann which has been used as a guide for this section [46].

A stochastic process is a Markov process, meaning that each transition event is independent of previous events. Any sequence can therefore be described by a starting single process probability and a sequence of conditional probabilities linking the possibility of a further event happening if a prior event has already occurred. The equation describing the sequence becomes:

$$P_n(a_1t_1;...;a_nt_n) = P_1(a_1t_1)p(a_1t_1|a_2t_2)...p(a_{n-1}t_{n-1}|a_nt_n), \tag{1}$$

where each conditional probabilities is given by a different factor p(...|...), which describes the probability of starting in an initial state, first half of the bracketed term, and ending in a final state, second half of the bracketed term. To take account of multiple pathways between initial and final sites it is necessary that the conditional probability obeys the Chapman-Kolmogoroff equation [47]. The conditional probability is adapted to sum over different intermediate steps, a':

$$P_2(a_{\text{initial}}, t_{\text{initial}}|a_{\text{final}}, t_{\text{final}}) = \sum_{a'} p(a_{\text{initial}}, t_{\text{initial}}|a't')p(a't'|a_{\text{final}}, t_{\text{final}}). \tag{2}$$

The Markov property allows this to be rewritten so that the probability of an ion being in a certain position after some time depends only on the combined probabilities of it being in an intermediate state at an initial time and the probability of the hop between the intermediate and final state. This can be expressed as:

$$P_1(a_{\text{final}}t_{\text{final}}) = \sum_{a'} p(a't'|a_{\text{final}}, t_{\text{final}})P_1(a't'). \tag{3}$$

The differential with respect to time yields a jump rate of ions.

$$\frac{\delta P_1(a_{\text{final}}t_{\text{final}})}{\delta t} = \sum_{a'} \dot{p}_t(a', a_{\text{final}})P_1(a', t) = \sum_{a' \neq a} \big\{\Gamma_{a'a}P(a', t) - \Gamma_{aa'}P(a, t)\big\}, \tag{4}$$

where Γ indicates a transition rate from a first state into a second state. The right hand side is known as the master equation and can be derived given that $\dot{p}_t(a', a_{\text{final}}) = \Gamma_{a'a}$ and that the probability of a state occurring at a certain time is negatively affected by it having already occurred. In the context of jump diffusion between sites, the master equation accounts for any differences in site energy between forward and back motions, as the hopping rates are governed by the detailed balance condition.

1.2.2 Diffusion Rates

The derivation of the jump rate of ions, Γ, from stochastic motions allows for the calculation of a diffusion rate. The mass of the diffusing particle, Li or Na ions, is considered large enough that hops only occur by thermally activated classical processes. A general equation for rate processes involving a potential barrier was proposed by Eyring who used a statistical interpretation [48]:

$$\Gamma = \frac{k_b T}{h}\frac{F'}{F}\text{exp}\left(\frac{-E_a}{k_b T}\right), \tag{5}$$

where T is temperature, k_b is the Boltzmann constant, h is the Planck constant, E_0 is the potential barrier given by the energy difference between the ground and activated states and F' and F are partition functions for the activated and initial state respectively. The partition functions are defined according to a quasi-chemical equilibrium between the ground and activated states wherein an equilibrium constant determines the fractional occupancies in each state. As a result the second factor describes the migration entropy, as the partition functions describe the states in thermodynamic equilibrium and therefore at maximum entropy, and the third factor describes the migration enthalpy. The partition functions can be rewritten in terms of the phonon frequency, v, along the hopping direction [49]:

$$\Gamma = \frac{k_b T}{h}\left(1 - \exp\left(\frac{-hv_0}{k_b T}\right)\right)\exp\left(\frac{-E_a}{k_b T}\right), \tag{6}$$

which in the limit of a small frequency, such that $hv_0 << kT$, reduces to:

$$\Gamma = v_0\text{exp}\left(\frac{-E_a}{k_b T}\right), \tag{7}$$

where v_0 is equivalent to a jump rate constant Γ_0. The inverse of the jump rate describes the mean residence time, τ, of an ion remaining on one site before hopping, which is thermally regulated by the exponential factor, obeying the Arrhenius law:

$$\tau = \tau_0\text{exp}\left(\frac{E_a}{k_b T}\right), \tag{8}$$

where τ_0 is a pre-exponential factor. Each possible hop has its own E_a dependent on local ordering. Reasons for variation include the local energy map dependent on the arrangement of nearest neighbours, the presence of multiple energetically distinct sites, and vibrational modes creating a dynamic ground state for the hopping ion. The Arrhenius law is considered to be macroscopic and is linked to diffusion by the Einstein-Smoluchowski relation:

$$D_{\mathrm{E-S}} = \frac{l^2}{2d\tau}, \tag{9}$$

where d is the dimensionality of the process and l is the average jump length. In gas or liquid systems l refers to the mean free path, however for crystalline materials l is controlled by the distance between sites.

1.2.3 Diffusion Mechanisms

Several mechanisms have been proposed by which diffusion is able to occur within crystalline materials [50]. The simplest is the vacancy mechanism in which ions diffuse by moving into neighbouring vacant lattices. An example is shown for a simple square lattice in Figure 4a. The red ion moves into an adjacent vacant site which has an equivalent energy. In a system with a high concentration of ions there is a high probability of sites being blocked so self-diffusion of a single ion will be low while self-diffusion of the hole will be much larger.

The interstitial method involves the presence of a secondary lattice of interstitial sites. An interstitial ion can hop from one interstice to another around the ions of the regular lattice. The hop of the red ion in Figure 4b is an example. As the ion moves on a secondary lattice there is a low probability of site blocking. Consequently this mechanism typically leads to fast diffusion rates.

A more complicated method is the interstitialcy mechanism, shown in Figure 4b. Initially the red ion, on the interstitial lattice, and the light blue ion, on the regular lattice, are neighbouring. They move in unison with the red ion assuming the light blue ions site on the regular lattice and the light blue ion hopping on to a new interstitial site. The disturbed ion can then displace another ion from the regular lattice via the interstitialcy mechanism.

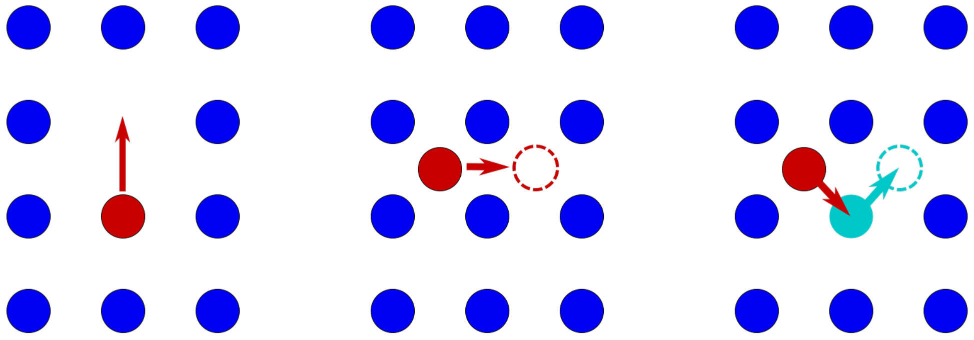

(a) Vacancy Hop Mechanism

(b) Interstitial Hop Mechanism

(c) Interstitialcy Hop Mechanism

Figure 4: A regular square lattice is formed by the blue ions. In a) the vacancy mechanism is displayed with the red ion hopping to a neighbouring vacant site. In b) the interstitial mechanism is displayed with the red ion hopping between sites on an interstitial lattice. In c) the interstitialcy mechanism is displayed. An ion on the interstitial lattice, red, displaces an ion on the regular lattice, light blue. The displaced ion hops onto an interstitial site.

1.2.4 Correlations

It is necessary to consider the effect of concentration on the diffusion of ions across a lattice. In a near empty lattice ion hops can be considered to be uncorrelated. As the concentration increases, a non-negligible chance is introduced that a neighbouring site will be blocked by another ion. The directionality of the next hop is dependent on the probability of sites being available. For the interstitial and interstitialcy mechanisms, all hop directions are equivalent in probability. For the vacancy mechanism, however, the reverse hop is always immediately available, increasing the probability of a hop in this direction. Compaan and Haven [51] introduce a factor, f, describing the correlation between successive jumps modifying the Einstein-Smoluchowski diffusion, Eq. (9), in comparison to the random walk diffusion, so that $D_{\mathrm{E-S}} = fD_{\mathrm{RW}}$. The correlation factor is given as:

$$f = \frac{1 + \langle \cos\theta_{i,i+1} \rangle}{1 - \langle \cos\theta_{i,i+1} \rangle} = \frac{\langle l^2 \rangle}{\langle l^2_{\mathrm{random}} \rangle}, \tag{10}$$

where $\theta_{i,i+1}$ is the angle between two successive steps of a particle and $\langle \cos\theta_{i,i+1} \rangle$ is the average of the angle between all individual successive hops. Values of f are typically less than 1 due to the always unblocked backward hop which results in a negative average. As a result, microscopic measurements, such as QENS, can overestimate diffusion rates in comparison to macroscopic measurements, such as tracer diffusion. Effectively the microscopic measurements observe every motion individually, forward and back, while the macroscopic measurements observe the net motion.

Equation (10) concerns only the spatial correlations between hops. An assumption of stochastic diffusion is that each hop is temporally uncorrelated as the mean residence time between hops is far greater than the hop time. In effect after each hop the ion stabilises on its new site. However, a molecular dynamics investigations by Morgan and Madden [52] into the relationship between atomic diffusion and ensemble transport mechanisms has shown a strong temperature dependence of f for certain crystal structures. Successive hops results in chains which are defined as being short and closed if they are strongly correlated, or as long and open if the hops are weakly correlated or uncorrelated. Temporal correlations lead to series of hopping events, known as cascades. The correlations within a system need to be judged carefully, particularly when comparisons are being made between microscopic and ensemble transport mechanisms.

2 Experimental Techniques

2.1 Crystallography

An energetically favourable arrangement of ions can be formed by any repeating unit cell, containing all of the ions necessary to describe the system. Crystallography is the science of the determination of crystalline atomic structures. The shape of the unit cell, and arrangement of ions within, sets the level of symmetry present in the crystal which is used to identify and describe every system. Inherently every crystal must have translational symmetry due to the periodic structure. Additionally almost all crystals will be described by other symmetry operations such as reflection, rotation, glide plane and screw axes. The methodology and notation to be used when determining crystal structure is contained within the International Tables of Crystallography [53].

The basic unit cell is described by one of 14 Bravais lattices that link all equivalent positions. The unit cell, and the distance between lattice points, is described by the three vectors **a, b, c** or by a combination of three scalars a, b, c and three angles α, β, γ. These are the lattice parameters of the system. The relationships between the different lattice parameters leads to 7 primitive lattice systems: Triclinic, Monoclinic, Orthorhombic, Tetragonal, Rhombohedral, Hexagonal and Cubic. The arrangement of ions within the unit cell gives further symmetry properties, dividing the classification of crystals into a total of 230 space groups [54]. The unit cell is typically chosen to describe the system using the minimum number of atoms or so that a high level of symmetry is preserved.

The position of any atom can be described as a discrete translation to obtain its lattice position and then its position within the unit cell itself, as shown in Figure 5.

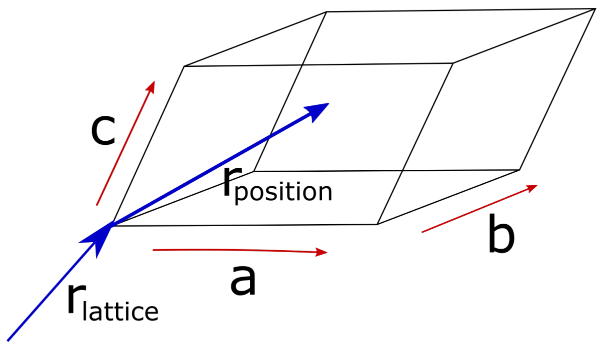

Figure 5: The atom position is described in terms of the unit cell vectors **a, b, c**. The position can be split into two parts; the location inside the unit cell and the location of the unit cell in the lattice.

Algebraically this can be written as:

$$\mathbf{R} = \mathbf{r}_{\text{lattice}} + \mathbf{r}_{\text{position}} = (x+m)\mathbf{a} + (y+n)\mathbf{b} + (z+o)\mathbf{c}, \tag{11}$$

where x, y, z are integer numbers and $0 \leq n, m, o < 1$, as shown in Figure 5. Due to the equivalence of points it is only necessary to discuss one unit cell and therefore the position of atoms need only be described by $\mathbf{r}_{\text{position}}$. It is usually not necessary to describe the location of every atom in a system as all equivalent symmetrical positions in a lattice are described by the Wyckoff positions [55]. Each different Wyckoff position is labelled by a letter with later letters indicating increasing numbers of symmetrical sites.

2.1.1 Crystal Growth

Extensive efforts go into creating crystals for experiments. A variety of methods are used to grow samples however as neutron experiments need large single crystals, a floating zone furnace [56] is used at Royal Holloway, shown in Figure 6a. The floating zone furnace consists of several heating lamps and elliptical mirrors that focus the light into a very small common region. Due to the highly localised heating a single crystal can be drawn out from a starting seed crystal by slowly moving a rod like sample through the focus.

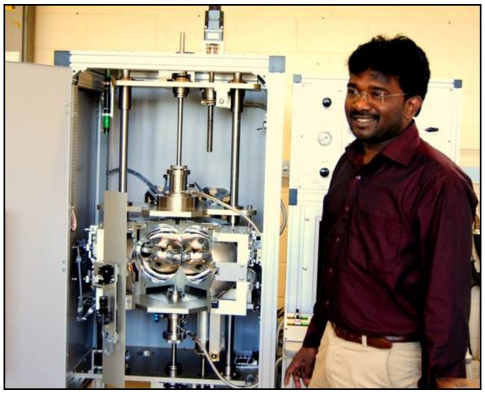

(a) Floating Zone Furnace

(b) A Na_xCoO_2 crystal.

Figure 6: a) The floating zone furnace at Royal Holloway and b) a crystal grown using the floating zone furnace, that has subsequently been cleaved into a large single crystal of ~ 4 cm.

The rod is grown from precursor chemicals, of high purity, which contain the appropriate ratios of elements that react to form the compound with the required stoichiometry. The polycrystalline sample is ground into a homogeneous fine powder before being heated in a box furnace above a certain temperature in a controlled atmosphere; this is known as calcination. The high temperature will allow the precursor compounds to break down, mix and form new bonds. At this point certain gases, such as CO_2, may form from the precursor elements and evaporate from the system. The sample may then be reground and the calcination process repeated.

After several cycles the powder will be homogeneously mixed and additional elements will have been removed leaving only the required crystal structure. The sample is compressed into a rod to remove air bubbles and other pockets that would impede the growth of a large single crystal from a single grain. Prior to the final growth, the crystal grains are enlarged by sintering the rod at high temperatures. The sample rod, known as the feed rod, and a chemically similar seed rod are placed so that the ends are in the focussed beam.

The brightness of the lamps is increased until the tips of the feed and seed rods begin to melt. The rods are then brought into close proximity and an interface forms between the two at the focal point of the lamps. The seed rod provides the initial crystal grain; the focus is slowly moved up the feed rod and, ideally, a single grain encompassing the whole of the sample crystallises on top of the seed. The growth of the structurally related Li_xCoO_2 by our group is explained in [57]. Sometimes it is necessary to cleave the sample by breaking it up along crystal faces. This is done to break apart separate crystallites and ensure that each piece is its own crystal, Figure 6b.

2.2 Scattering Cross-Sections

Thermal Neutron Scattering provides a powerful probe of atomic structures. The wavelength can be tailored to the order of inter-atomic distances by moderating the energy. Understanding the scattering allows the visualisation of the static and dynamic correlations in a sample material.

Scattering from a single nucleus is spherically symmetric when the wavelength of

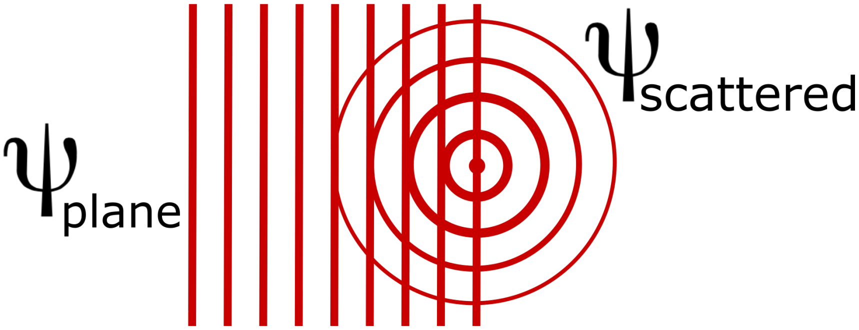

Figure 7: Spherical scattering, $\psi_{\text{scattered}}$, of a plane wave, ψ_{plane}, from a point-like object.

the probe is far greater than the size of the nucleus, Figure 7, i.e. the nucleus appears point-like. For elastic scattering of a plane wave, $\psi_{\text{plane}} = \exp(\mathrm{i}kx)$, the spherically symmetric scattered wave function is described by:

$$\psi_{\text{scattered}} = -\frac{b}{r}\exp(\mathrm{i}kr), \tag{12}$$

where the scattering length, b, determines the strength of the scattering, k is the wavevector, and r is a real space position. Neutrons lack a charge, therefore effectively ignoring the electron shells of atoms and instead scatter from the nuclei themselves via the strong force. The scattering length depends upon the isotope of the nucleus and varies seemingly randomly, which is why the lengths are determined experimentally [58]. For ions with unpaired electrons, scattering can also be caused by interactions between the magnetic moments of the atom and the neutron.

X-rays scatter from the electron cloud due to electromagnetic interactions. The strength of the scattering is determined by the size of the cloud and hence larger ions scatter more.

2.2.1 Total Scattering Cross-Section

The magnitude of the scattering by a sample is described by the cross section of the interaction. The total scattering cross section, σ_{Total} is the number of particles scattered in all directions divided by the initial flux. The differential of solid angle and energy is applied to the total scattering cross section to provide information about the spatial and temporal correlations, respectively [59]. The solid angle is described as a cone of area increasing away from the scattering focal point, Figure 8.

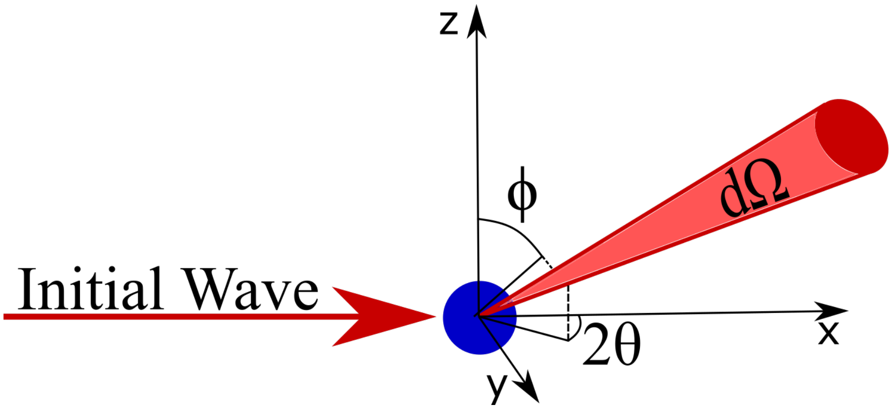

Figure 8: The scattering of an initial wave from a sample, blue, can be described by cones of solid angle $\mathrm{d}\Omega$ in directions given by $\mathrm{d}\theta$ and $\mathrm{d}\phi$, where the initial wave has a wavevector $\mathbf{k}_i$ and an energy E and the final wave has a wavevector $\mathbf{k}_j$ and an energy $E + \mathrm{d}E$.

The total scattering cross section can be written algebraically as:

$$\sigma_{\text{Total}} = \int_{E}^{E+\mathrm{d}E} \int_{\text{all directions}} \frac{\mathrm{d}^2\sigma}{\mathrm{d}\Omega\ \mathrm{d}E}\ d\Omega\ \mathrm{d}E, \tag{13}$$

where $\mathrm{d}\sigma$ is the cross section of scattering into a solid angle of $\mathrm{d}\Omega$ with an energy change of $\mathrm{d}E$. From the Van Hove formalism, the double differential cross section can be expressed for a system of N identical atoms of the same isotope as [60]:

$$\frac{\mathrm{d}^2\sigma}{\mathrm{d}\Omega\ \mathrm{d}E} = b^2\ \frac{k_f}{k_i}\ N\ S(\mathbf{Q},\omega). \tag{14}$$

S($\mathbf{Q}$,ω) is the scattering function of the system and details the level of scattering observed at particular point in reciprocal space, $\mathbf{Q}$, with the wave having energy $E = \hbar\omega$. $\mathbf{Q}$ is the change in momentum given by $\mathbf{Q} = \mathbf{k}_i - \mathbf{k}_f$ and the frequency ω provides the energy change d$E = \hbar\omega = \frac{\hbar^2}{2m_{\text{neutron}}}(k_i^2 - k_f^2)$ for neutron scattering. The scattering of any event can be described graphically in reciprocal space by a triangle of vectors, Figure 9. A description of the scattering in terms of reciprocal space is useful as this is what is measured, and it can be straight forwardly related to real space.

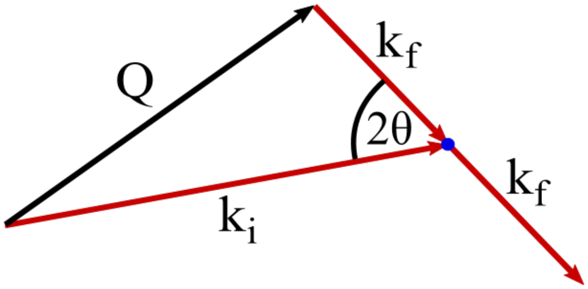

Figure 9: An initial wave, $\mathbf{k}_i$, scattered in a direction $\mathbf{k}_f$ will have a $\mathbf{Q}$ given by the difference of their vectors and an energy change proportional to the difference in the square of the magnitude of the vectors.

$\mathbf{Q}$ can be related to the real space planes of the crystal for elastic scattering by the formula:

$$\mathbf{Q} = 4\pi \sin\left(\frac{\theta}{\lambda}\right), \tag{15}$$

where $\lambda = \frac{2\pi}{|\mathbf{k}_i|} = \frac{2\pi}{|\mathbf{k}_f|}$ for elastic scattering and θ is the angle of the incident and final wave vectors with respect to the plane normal, hence the scattering has a deflection angle of 2θ. The coherence between atoms and the coherence of an atom with itself is best described by the pair correlation function $G(\mathbf{r}$,t), of which the scattering function is the Fourier transform. The two are related by the equation:

$$S(\mathbf{Q},\omega)=\frac{1}{2\pi\hbar}\int\int G(\mathbf{r},t)\exp(\ \mathrm{i}\ (\mathbf{Q}\cdot\mathbf{r}-\omega t))\mathrm{d}\mathbf{r}\mathrm{d}t. \tag{16}$$

2.2.2 Separation of Cross-sections

In a crystal system, it is not necessary to sum over all ions, since the calculation is simplified by factorisation by the unit cell. The scattering amplitude is then multiplied by a factor indicating the number of unit cells. This uses the concept of the crystal lattice which was discussed in section 2.1 as a way of describing a large system made up of a repeating arrangement of atoms. The pair correlation function is unaffected as the correlations between ions are preserved by the averaged cell. The elastic scattering for such a system at a point $\mathbf{Q}$ can be expressed as:

$$\frac{\mathrm{d}\sigma}{\mathrm{d}\Omega}=\left|\sum_j b_j\exp(\mathrm{i}\mathbf{Q}\cdot\mathbf{r_j})\right|^2, \tag{17}$$

where for each ion j at position $\mathbf{r}_j$, b_j is their scattering length.

Overall the crystal structure will have fixed sites, however those sites can be occupied by different isotopes according to some probability dependent on the system and the particular site. The introduction of random factors into the placement of ions leads to a separation of the total scattering function into a coherent and an incoherent part. Similarly, isotopes with non-zero nuclear spin states will have a random spin direction at temperatures above $\sim$1 K which will interact with the neutron spin.

The two scattering components provide information about different properties of the studied system. Coherent scattering provides a visualisation of interference effects within the material. These can be from Bragg scattering from the static crystallographic planes or they could be from collective motions within the material such as lattice vibrations. Incoherent scattering in comparison provides information about deviations from the average system and therefore can be used to study individual atoms [59].

Equation (17) provides a starting point to algebraically separate the coherent and incoherent cross sections. By taking the complex conjugate, the equation can be rewritten to express the scattering from the sum of pairs of sites:

$$\frac{\mathrm{d}\sigma}{\mathrm{d}\Omega} = \sum_{j}\sum_{j'}\langle b_j b_{j'}\rangle \exp(\mathrm{i}\mathbf{Q} \cdot (\mathbf{r}_j - \mathbf{r}_{j'})) \tag{18}$$

where $\langle b_j b_{j'}\rangle$ is the ensemble average for a random arrangement of isotopes on equivalent sites. The combination of the summations have two possibilities; either $j = j'$ or $j \neq j'$. In the first case $\langle b_j b_{j'}\rangle$ becomes $\langle b_j b_j\rangle = \langle b^2\rangle$ and in the second case $\langle b_j b_{j'}\rangle$ becomes $\langle b_j\rangle\langle b_{j'}\rangle = \langle b\rangle^2$. Using these relationships equation (18) can be rewritten as:

$$\frac{\mathrm{d}\sigma}{\mathrm{d}\Omega} = \sum_{j,j'}\langle b\rangle^2 \exp(\mathrm{i}\mathbf{Q} \cdot (\mathbf{r}_j - \mathbf{r}_{j'})) + \sum_{j}(\langle b^2\rangle - \langle b\rangle^2). \tag{19}$$

Equation (19) is separated into two parts; the first summation is dependent on the overall average scattering length of the system and therefore provides the coherent term. The second summation is over the mean squared difference between scattering lengths providing the incoherent term. The magnitude of the incoherent scattering depends on the range of isotopic scattering lengths for isotope incoherence and the nuclear spin for spin incoherence. It is easy to see how this second term would disappear if all isotopes were the same or if there was no magnetic moment due to nuclear spin. It would only be possible to get the first term to disappear if the average was close to 0. In reality this is only approximately the case with certain atoms such as vanadium which has a very low coherent scattering length.

2.2.3 Coherent Elastic Scattering

Coherent Scattering depends on the correlation between different nuclei at different times, and also for self-correlation the positions of the same nuclei at different times, making it important in highly ordered structures where the periodicity of the structure leads to interference effects. The level of scattering is determined as if all nuclei had the same scattering length b, written as $\sigma_{\mathrm{coh}} = 4\pi(\bar{\mathrm{b}})^2$. A structure factor $F(\mathbf{Q})$ can be written which entails the sum of the different scattering components within a unit cell.

$$F(\mathbf{Q}) = \sum_j b_j \exp(-\mathrm{i}\mathbf{Q} \cdot \mathbf{r}_j). \tag{20}$$

Using kinematic theory [61] the coherent scattering cross section can be expressed as:

$$\frac{\mathrm{d}\sigma}{\mathrm{d}\Omega} = \frac{N(2\pi)^3}{V} \sum_\tau |F(\mathbf{Q})|^2 \delta(\mathbf{Q} - \tau), \tag{21}$$

where the prefactor $\frac{N(2\pi)^3}{V}$ provides density information as N is the number of unit cells and V is the volume of each individual unit cell. There is a new summation over the quantity τ which is contained in a delta function that arises from the Fourier transform of an infinitely repeating crystal lattice. It ensures that Bragg scattering only occurs when $\mathbf{Q} = \tau$, where τ is a reciprocal lattice point given by $\mathrm{h}\mathbf{a}^* + \mathrm{k}\mathbf{b}^* + \mathrm{l}\mathbf{c}^*$. As a result diffraction occurs at points on a 3 dimensional grid corresponding to the integer spacings of the reciprocal lattice, as shown in Figure 10.

The reciprocal lattice point corresponds to scattering from a crystallographic plane of the lattice. The typical convention is to use Miller indices to express the planes [62]. A plane, is expressed as $\{h, k, l\}$ where h, k and l are integer multipliers of $\mathbf{a}$, $\mathbf{b}$ and $\mathbf{c}$, respectively, describing the vector orthogonal to the plane, as shown in Figure 11. This notation gives a direct link between the position of the reciprocal lattice point and the spacing of repeating crystallographic planes.

Eq. (20) and Eq. (21) refer to systems at zero temperature. In a realistic crystal system, for non-zero temperatures, atoms are not fixed in space but instead oscillate around their equilibrium positions. The Debye-Waller factor is introduced to account

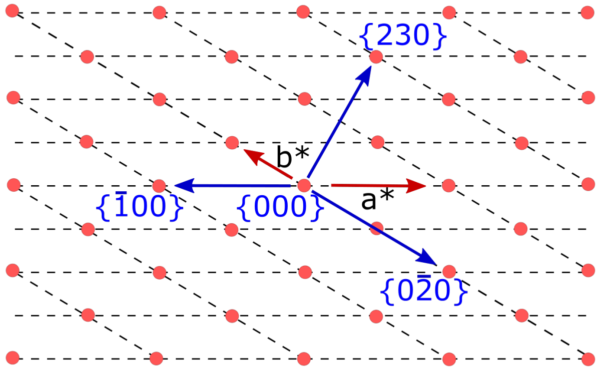

Figure 10: Bragg peaks from elastic scattering are shown by red circles on a 2D plane. A unit cell is underlayed by dashed black lines with the **a*** and **b*** vectors shown in red. Bragg peaks only occur at integer numbers of **a***,**b*** and **c***. The Miller indices of several Bragg peaks are shown in blue.

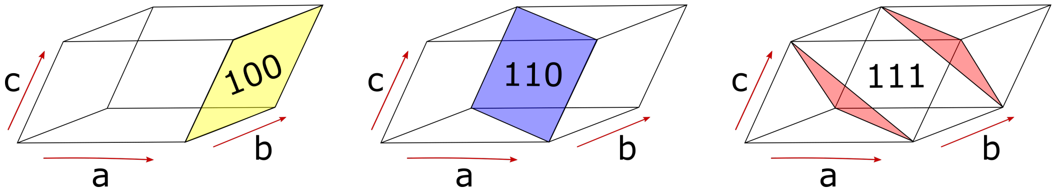

(a) {100} plane (b) {110} plane (c) {111} plane

Figure 11: Crystallographic planes given by their Miller Indices. The integer numbers refer to the reciprocal lattice vector orthogonal to the plane.

for the variations from the ideal system, particularly the variations in atomic position from the infinitely repeating crystal lattice as defined by the delta function of Eq. (21). The Debye-Waller factor alters the zero-temperature formula of Eq. (21) to give[63]:

$$\frac{\mathrm{d}\sigma}{\mathrm{d}\Omega} = \left[\frac{\mathrm{d}\sigma}{\mathrm{d}\Omega}\right]_{T=0} \times \exp\left(-\frac{\alpha T Q^2}{2}\right), \tag{22}$$

where α defines the variance of the atomic variations and T is the temperature of the system. Accordingly, the oscillations of atoms around their equilibrium positions suppress the scattering intensity in comparison to the ideal zero temperature system. As temperature increases the level of suppression increases exponentially. Importantly for scattering purposes, the Debye-Waller factor describes the suppression of scattering intensity as Q increases. As a result, measurements taken at high Q have a lower flux and, therefore, require longer measurement times.

Equation 22 describes a system of atoms that oscillate in a spherically symmetric manner around their equilibrium position. It should be appreciated that the structure of the crystal system may distort the oscillations of the ions from a spherical distribution. The anharmonicity can be compensated for by generalizing the exponents of the Debye-Waller factors to represent ellipsoids in Q_x, Q_y and Q_z[63]. Different atoms will also vibrate differently, for example due to their relative masses, which is compensated for by altering the constant α.

2.2.4 Incoherent Scattering

For crystals coherent scattering provides extremely focussed streams of neutrons corresponding to the reciprocal lattice vectors. In comparison, the incoherent scattering provides a general background of neutrons in all directions. This is because the incoherent scattering is dependent on random variations in the crystal structure and therefore only on the correlation of the position of the same nuclei at different times. In the case of a static system, the Fourier transform of a delta function at the origin, gives completely flat scattering that is independent of Q. The incoherent cross section of a material is given by $\sigma_{inc} = 4\pi(\overline{b^2} - (\bar{b})^2)$. The contrast in intensities between the incoherent and coherent scattering can lead to incoherent effects being overshadowed especially near to Bragg peaks.

The variations from the average scattering function can come as a result of either isotopic variation or an isotope having a non-zero spin state. Isotopic variation does not typically disrupt the unit cell of a material because a material's structure is dominated by its electronic nature. The addition or removal of extra neutrons from an ion will not change its position in a crystal structure as it will only cause a small change in the mass of the nucleus. This means isotopes will order randomly as the ground state energy will not be affected by their positions. For incoming neutrons, which interact via nuclear forces, the scattering length is different for each isotope.

2.2.5 Inelastic Scattering

As a probe interacts with the system, energy can be received or imparted through inelastic collisions. The energy transferred is related to the incoming and outgoing wave vectors of the probe. Neutrons are a particularly useful probe as for wavelengths equivalent to lattice spacings, their energy can be tailored to the energy of phonon excitations within the material. In comparison X-rays of the same wavelength will have energies 5 or 6 orders of magnitude larger [64]. The energy exchanged in an inelastic collision can be calculated easily for neutron scattering using the following equation:

$$\hbar\omega = \frac{\hbar^2}{2m_\mathrm{n}}(k_\mathrm{i}^2 - k_\mathrm{f}^2). \tag{23}$$

For coherent scattering the change of energy is related to the correlated motions of ions. These are generally lattice vibrations which are determined by the bonding within the crystal structure. These oscillatory motions cause scattering in specific areas of reciprocal space determined by the phonon dispersion. These regions are fixed because the incoming neutrons effectively gain or lose energy equivalent to the resonance of the atomic vibration.

The incoherent scattering depends only on correlations between the same particle at different times. These local motions depend upon the vibration of individual ions and occasional hops to vacant adjacent lattice sites.

2.3 Neutron Experimentation

An explanation of the quasi-elastic neutron scattering technique used within this thesis is described along with an explanation of the production of neutrons and the instrumentation necessary to analyse the scattering.

2.3.1 Quasi-Elastic Neutron Scattering

Quasi-Elastic Neutron Scattering (QENS) is a probe of the self-correlation function of the ions of the sample. That is the probability, P(**r**,t), that an atom in a position, **r**, will be in a position, $\mathbf{r}'$, at a later time, t. At a significantly low temperature, the ions in the sample will be largely immobile, as vibrations have been damped, so the self-correlation function will not be dependent on time. Higher temperatures increase the motions of the ions, including jumps between sites, adding a time-dependent component to the self-correlation function.

Incoherent QENS probes the stochastic motions of the ions, described in Section 1.2.1. The master equation, Eq. (4), can be expressed to describe simple translational jump diffusion by inserting a common mean residence time that ions reside in sites before hopping [46].

$$\frac{\delta P(\mathbf{r},t)}{\delta t} = \frac{-1}{z\tau}\sum_{j=1}^{z}\left\{P(\mathbf{r},t) - P(\mathbf{r}'_j,t)\right\}, \tag{24}$$

where $\mathbf{r}'_j$ is the new site location, after a hop with a jump vector $\mathbf{l}_j = \mathbf{r}'_j - \mathbf{r}$, τ is the mean residence time an ion stays on a site between hops and the summation is over all possible hops up to the coordination number z. Hence the jump rate is related to the mean residence time by $\Gamma = \frac{1}{z\tau}$. Using the Fourier transform

$$\int P(\mathbf{r},t)\ \exp(\mathrm{i}\ \mathbf{Qr})\ \mathrm{d}\mathbf{r} = P(\mathbf{Q},t), \tag{25}$$

the master equation can be converted to Fourier space, providing the self-part of the intermediate scattering function.

$$P(\mathbf{Q},t) = I_{\text{self}}(\mathbf{Q},t) = \exp\left(\frac{-t}{z\tau}\sum_{j=1}^{z}\big(1-\exp(-\mathrm{i}\ \mathbf{Q}.\mathbf{l}_j)\big)\right). \tag{26}$$

Considering $I_{\text{self}}(\mathbf{Q},t)$, a distinction can be made between rotational and translational diffusion. While for $I_{\text{self}}(\mathbf{Q},0)$ contributions to the scattering from rotational and translational diffusion are indistinguishable as the $I_{\text{self}}(\mathbf{Q},t)$ equals unity; however, when t goes towards infinity for the contribution from rotational diffusion converges to a finite value while the contribution from translational diffusion converges to zero.

This occurs as for rotational motion the hops are spatially restricted and the number of sites is finite, and hence this is referred to as localised motion. The Fourier transform of the localised motion consists of both elastic and quasi-elastic terms, while the Fourier transform of the translational motion with respect to time, of Eq. (26), yields only a quasi-elastic term for the incoherent scattering function at the heart of a QENS measurement.

$$S_{\text{incoherent}}(\mathbf{Q},\omega) = \frac{1}{\pi}\frac{\Gamma(\mathbf{Q})}{\Gamma(\mathbf{Q})^2+\hbar^2\omega^2}. \tag{27}$$

The importance of this equation is that it describes the scattering signal using only one parameter, the Lorentzian function $\Gamma(\mathbf{Q})$. Ideally the presence or lack of a elastic component can be used to identify whether the system comprises translational or rotational motion, however elastic components can also arise from other static ions in the crystal lattice. The Lorentzian function $\Gamma(\mathbf{Q})$ which is directly related to the mean residence time and the hop vector.

$$\Gamma(\mathbf{Q}) = \frac{\hbar}{z\tau} \sum_{j=1}^{z} \left(1 - \exp(-\mathrm{i}\ \mathbf{Q}.\mathbf{l}_j)\right) . \tag{28}$$

Lorentzians are used to calculate the quasi-elastic components associated with both the localised and translational. Specifically for localised motion, a function called the elastic incoherent structure factor (EISF) is used to determine the fraction of quasi-elastic intensity contained in the elastic peak[46]. Approximately this can be calculated by fitting any neutron spectra with a single Lorentzian plus the elastic contribution, however this approach can be limited due to the presence of other static incoherent scattering ions.

The description of the incoherent scattering pattern due to translational ionic diffusion was first formulated by Chudley and Elliot [65]. Initially the model was for simple liquid systems where diffusion would occur via uncorrelated instantaneous hops, between equivalent sites independent of other motions within the system. The model provides a very good approximation for the diffusion mechanisms in simple crystalline materials.

For a crystalline material, possible hopping vectors can often be identified by inspection, noting the availability of adjacent sites and any beneficial distortion along hopping paths. Figure 12a shows three of the simplest possible hops for the $Na_{0.8}CoO_2$ system. The dot products of each individual hop with **Q** gives a different sinusoidal component. At low **Q** all of the Lorentzian widths go to zero producing scattering that appears elastic. Away from Q=0, the width goes to zero in a manner that depends upon the hopping lattice in real space. The amplitude of the oscillations in width depends upon the mean residence time between hops. Short range hops will have a much large oscillation period in reciprocal space.

For a powder or polycrystalline sample, the crystallites, and therefore the hop vec-

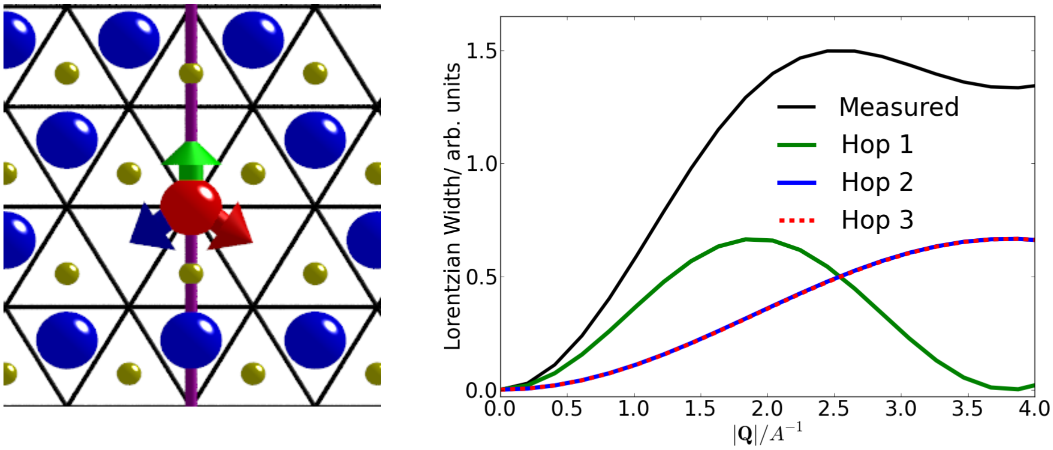

(a) Possible hop vectors

(b) Resulting Lorentzian

Figure 12: a) Hop vectors for a Na ion in a single crystal moving from a high energy site, red, to a low energy site, blue, with a purple line denoting the Q-cut direction, i.e. a line in Q space measured by detectors in real space. b) the resulting Lorentzian width predicted by the Chudley-Elliot model as a function of Q along the directions shown in a).

tors, are randomly orientated. The resultant Lorentzian is a spatial average of all hops dependent on the mean residence time and the magnitude of the hop vectors. For a single hop length, this simplifies Eq. (28) to:

$$\Gamma(Q) = \frac{\hbar}{\tau}(1 - \frac{\sin(Ql)}{Ql}). \tag{29}$$

Figure 13a shows an example of two different length hops, while Figure 13b shows how the resultant Lorentzian would appear based on Eq. (29). The time constant τ is kept the same for both hops, therefore differences in the magnitude and periodicity are solely caused by the hop length. The green hop has a shorter periodicity given that the direction of the hop is in the same direction as the Q-cut, whereas the other two hops have only a fraction of their motion in the direction of the Q-cut so appear to have a

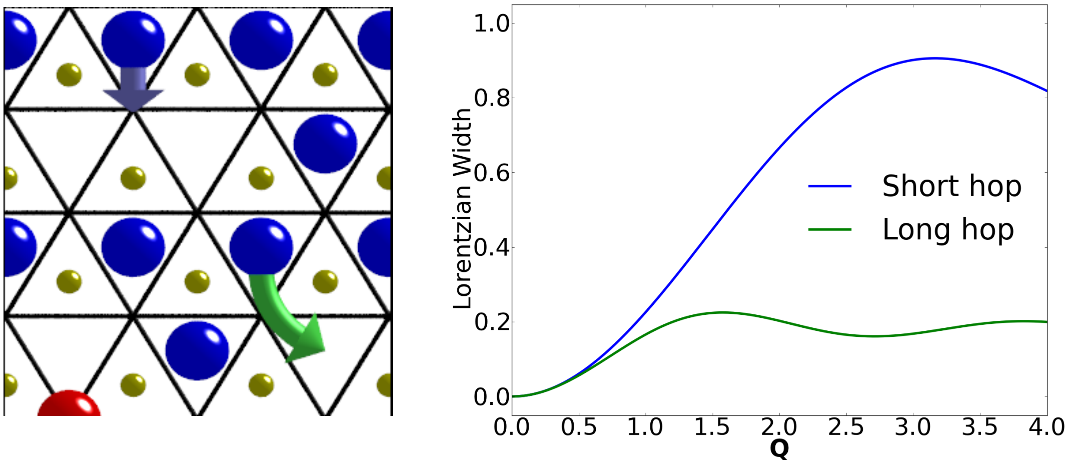

(a) Short and long hop vectors (b) Resulting Lorentzian

Figure 13: The resultant signal from QENS powder scattering according to the Chudley-Elliot formulism. The scattering is spherically symmetric from the sample depending only on the magnitude of Q. The scattering depends upon two factors; the hop length and the residence time, τ.

shorter hop.

If there are multiple types of hops, with different τ and hop lengths, then each can be described by its own Lorentzian function. Inequivalent site energies are caused by the local environment. If the hop length is unchanged then it will not be possible to separate out contributions and instead τ should be considered an average of mean residence times.

2.3.2 Neutron production from ISIS

ISIS is a world-class pulsed-neutron and muon source which has been operating for over 30 years with over 1000 proposals received annually in a wide variety of scientific fields [66]. Continual investment has seen the capabilities of ISIS increase greatly, particularly with the construction of a second target station and its instruments [67, 68]. Figure 14 shows the arrangement of the ISIS facility.

A description of the components of the spallation source is contained in reference [69]. However to summarise, H^- ions are created at an ion source before being bunched together using a radio frequency quadrupole accelerator. The discrete bundles are inserted into a linear accelerator, shown in red at the top of Figure 14, and the particles are accelerated to 70 MeV. The H^- ions are stripped of their electrons upon entering the synchrotron, which then accelerates them, as protons, up to 800 MeV. Fifty pulses a second leave the synchrotron with 40 of them going to target station 1 and 10 of them going to target station 2.

The protons collide with the tungsten target, chipping off spallation neutrons at high speed before absorbing into the nuclei of the target. The chipped off neutrons are at too high an energy to be useful for most applications however the absorbed protons promote neutrons to excited states. After a short period of time these neutrons can 'sweat' out, de-exciting the nuclei. These neutrons are at thermal energies and are then moderated to a particular temperature. Neutrons then travel along beam guides to the instruments.

2.3.3 OSIRIS

OSIRIS is an indirect geometry instrument [70] used for QENS experiments. The sample is exposed to the full range of neutrons produced at target (known as a white beam), although a chopper is used to prevent pulse overlap. Due to the pulsed nature of ISIS, the time the neutrons leave the target marks the fixed beginning of a measurement. The velocity of the neutrons will be dependent upon their thermal energies. This allows

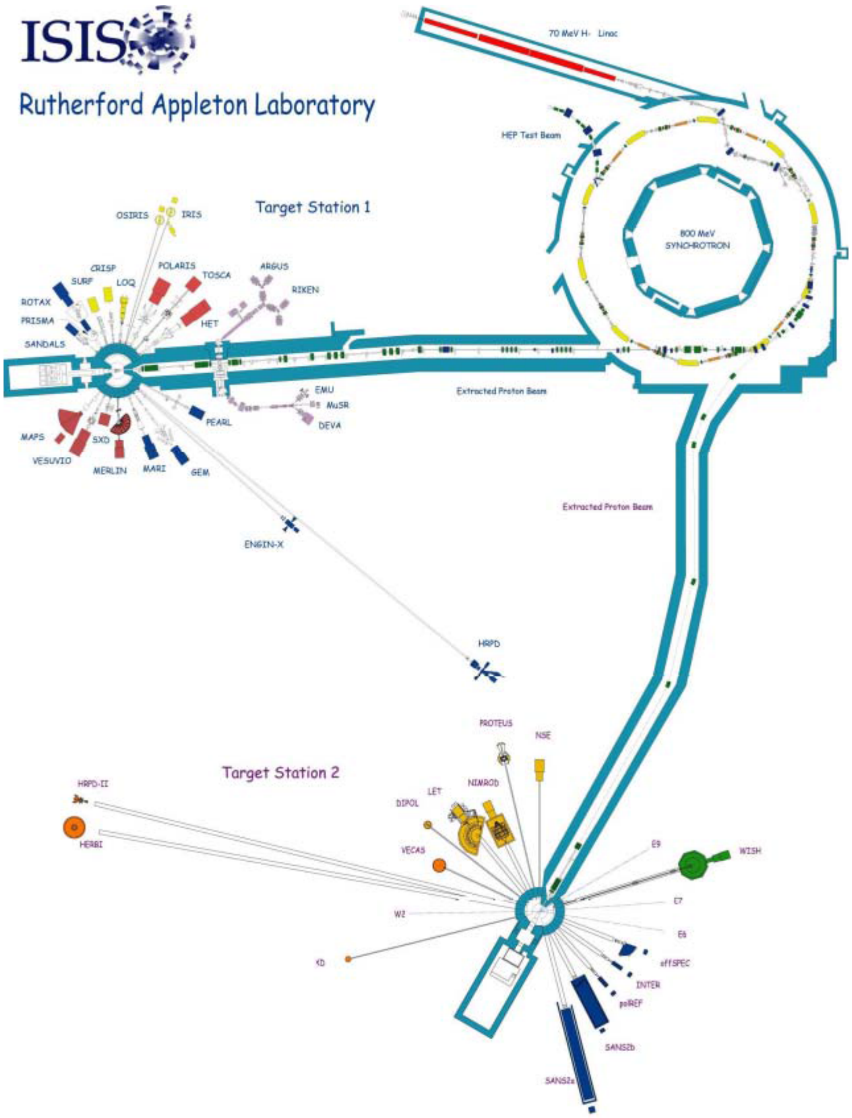

Figure 14: The ISIS facility at the Rutherford Appleton Laboratory [69]. A linear accelerator pumps protons into a synchrotron ring in bunches before they are guided towards either of the target stations. The protons collide with the targets producing neutrons which travel towards the instruments along the beam guides.

them to be sorted by monitoring the time it takes for them to reach the detectors from the target. The incident beam on OSIRIS is moderated by Hydrogen at 25 K. The long beam guide, 34 m, allows them to spread out in real space dependent on their respective velocities.

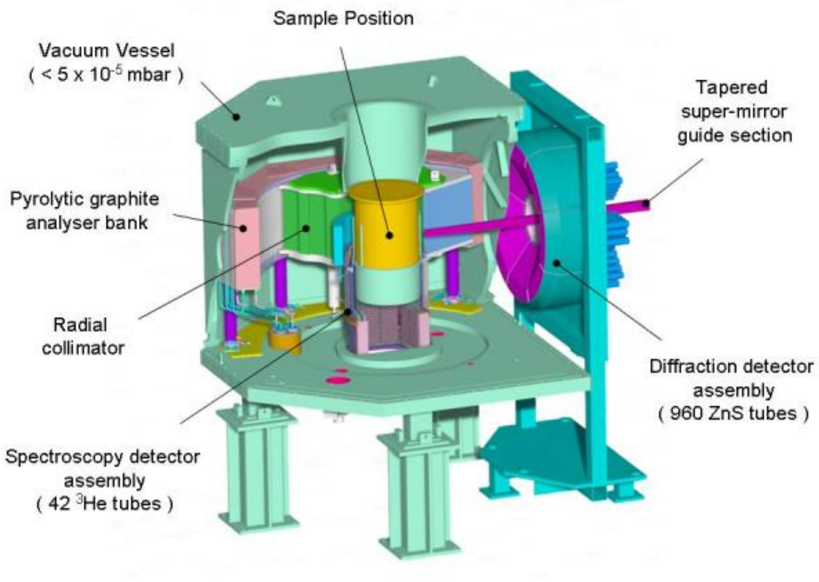

Figure 15: The OSIRIS instrument at ISIS [71]. The sample area is surrounded by collimators that reduce the background from the sample environment hitting the detectors. A bank of pyrolytic graphite Bragg scatters a single wavelength of neutrons into the detector banks located beneath the instrument. A diffraction setup is also present to allow characterisation of the sample.

OSIRIS has two completely different detector set ups as shown in Figure 15. It can run as a diffractometer due to a ring of detectors placed in a near backscattering position around the incident beam. By altering the chopper settings to change the energy range of the white beam, a large Q range can be measured which can be used to identify crystal structures.

The second setup involves a bank of 42 ^{3}He detectors which are arrayed from 11^o to 148^o in 2θ. These are the detectors that allow OSIRIS to function as a very low energy spectrometer which is its primary function. For spectroscopic measurements it is necessary that both $\mathbf{k}_i$ and $\mathbf{k}_f$ can be determined. Indirect spectrometers determine these by using an analyser crystal that can be aligned in such a way that it will Bragg scatter a certain wavelength towards the detectors. In the case of OSIRIS this is made of pyrolytic graphite which makes use of the [002] and [004] planes to scatter neutrons of 1.84 or 7.38 meV energies respectively. The reflection used is chosen by changing the chopper speed and phase to select a different section of the moderated pulse from the target. The setup is shown in Figure 16.

By knowing $\mathbf{k}_f$ and the time of flight, it is possible to determine $\mathbf{k}_i$ and any energy transfers that must have taken place. Any neutrons that have gained energy in interactions will arrive at the detector after, and any that have lost energy will arrive before elastically scattered neutrons.

Neutrons are reflected from a bank of analyser crystals into an array of detectors below the sample in close to back-scattering geometry, in order to achieve narrow resolution in energy transfer. Figure 17a shows the coverage of reciprocal space for elastic scattering for two orientations of the crystal. Although the $\mathbf{Q}$ position of each individual detector is equally spaced along the curve, there are more points at high $|\mathbf{Q}|$. Re-emphasising Figure 12; the orientation of the hopping pathways with respect to $\mathbf{Q}$ can lead to a large difference in the scale of the observed Lorentzian function, Figure 17b. The positioning of Aluminium powder Bragg lines are also shown as an example of how structural scattering may impede the measurement. Similarly Bragg peaks are possible at vertices of each hexagon in the grid.

Figure 17a is a prediction using the PG004 analyser reflection. Changing to the

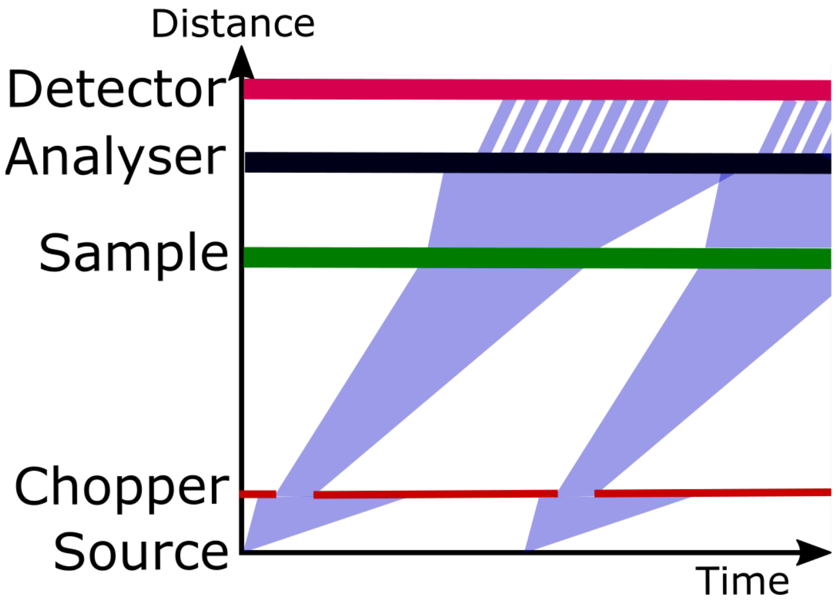

Figure 16: A distance vs time graph showing the energy selection of neutrons by the components of an indirect geometry spectrometer. The neutrons begin at a specific time at the target source. A specific range of velocities are chosen by the Chopper to prevent overlap. The neutrons hit the sample and scatter elastically and inelastically. The analyser crystal is aligned so that a strong Bragg reflection directs a single wavelength of neutrons into the detectors.

PG002 reflection will limit the **Q** range avoiding any elastic scattering due to planes with a spacing < 3.5 $\mathring{A}$. This has the advantage of lowering the background from multiple scattering, and this is beneficial when the QENS signal is small. Another advantage of this change is to improve the resolution of the system from 99 μeV to 25.4 μeV which is extremely useful in cases with small energy broadening. The disadvantage is that the Lorentzian width increases as $\mathbf{Q}^2$ for all models for small **Q**, and if the **Q** range is too short it will be difficult to distinguish between different hopping vectors.

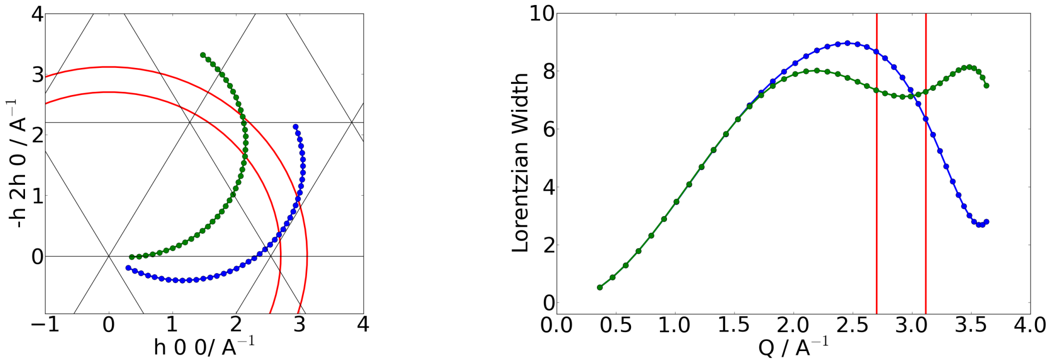

(a) 2 possible Q cuts with a hexagonal grid underlayed.

(b) Resulting Lorentzian from a Single Crystal

Figure 17: a) Two trajectories for elastic scattering in Q on OSIRIS using the PG004 analyser reflection. b) The resulting Lorentzian widths predicted by the Chudley-Elliot model for the hops shown in Figure 12a given a crystal in this orientation. Aluminium lines are shown in red.

2.4 X-ray Experimentation

X-ray diffraction is used in Chapter 7 to measure the crystal structure of several powder samples. Diffraction depends upon coherent scattering from crystal planes. An overview of the theory with respect to X-rays is given along with a description of the working of the Xcalibur Diffractometer used for these experiments.

2.4.1 X-ray Scattering

The interaction between X-rays and atoms is dependent upon electromagnetic forces between the probe and the orbital electrons. The scattering from X-rays is not point-like, differing from neutrons, and instead scatters off of the whole electron cloud. The formulation of the structure factor therefore depends not on the scattering length of the atoms, as in Eq. (20), but on the Q dependent atomic form factor [72]:

$$f(Q) = Zg(Q)r_e, \tag{30}$$

where Z is the atomic number, r_e is the Thomson scattering length and $g(Q)$ is the Fourier transform of the electron charge cloud. The magnitude of the scattering decreases monotonically with increasing θ and decreasing X-ray λ. Analytical approximations to $Zg(Q)$ for each atom are contained within the Volume C of the International Tables of Crystallography [73].

Simply put the electron cloud cannot be described as a point like object, particularly as the wavelength decreases, and therefore this changes the coherence of propagated waves. This contrasts heavily with the neutron scattering which is typically invariant with $\mathbf{Q}$ although a similar phenomenon is observed at high temperatures described by the Debye-Waller factor, which accounts for the loss of intensity due to the movement of ions around their nominal sites.

2.4.2 Xcalibur - Xray diffractometer

The Xcalibur X-ray diffractometer is a lab based source that produces X-rays from a Mo source. An image of the Xcalibur setup is shown in Figure 18. The X-rays are generated by accelerating electrons through a potential difference of the order of 10's of keV before colliding them into a metal target. Electrons in excited states then relax into lower states emitting X-rays at a specific energy according to the characteristic lines of the metal. An almost monochromatic beam is created by carefully tailoring the accelerating voltage [64]. Xcalibur uses the K_α line, 2p to 1s, of Mo which gives an almost monochromatic beam centred on 0.71069 $\mathring{A}$.

To enable the measurement of the total scattered volume, a goniometer with 4 axes of rotation is used which enables a sample to be rotated to almost any angle with respect

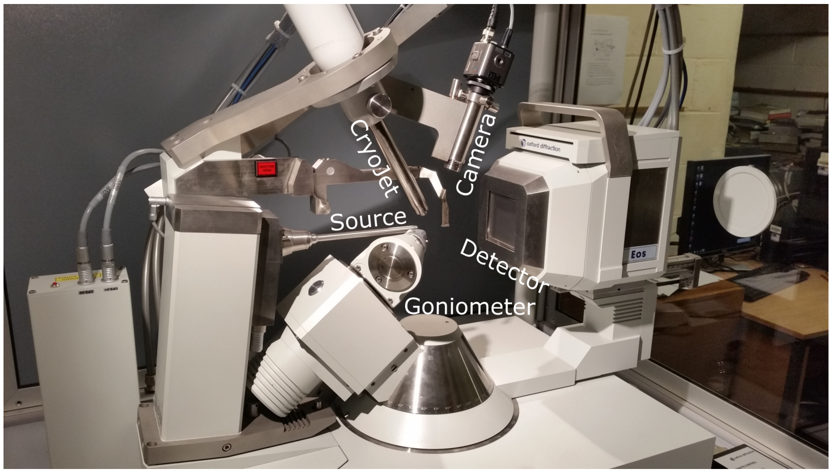

Figure 18: A picture of the Xcalibur X-ray diffractometer. The beam is generated in the housing on the left, while the CCD detector is on the right. The sample is mounted on the goniometer in the middle which is viewed by the camera, top right. Temperature is controlled via the CryoJet, top left.

to a detector [74]. Samples are typically measured in transmission mode and are up to 0.5 mm in size to enable transmission measurements. It is also possible to measure in reflection mode which allows larger samples, however it also severely limits the volume of reciprocal space that can be measured. A CCD camera is used to capture images of the scattered X-rays. Sequences of frames are analysed using the CrysAlis$^{\text{Pro}}$ software to identify and analyse diffraction patterns from the recorded peaks.

3 Computational Techniques

The use of sophisticated programs and high performance computers allows for the modelling of complex systems in condensed matter. Individual experimental techniques are limited to determining a few bulk or nano-scale properties at a time and, therefore, it is necessary to build up a picture of interactions within a system from a number of different techniques. The advent of *ab initio* calculations make it possible to model the interactions between atoms over small length scales without relying on experimentally determined parameters. The information gained can provide insight into processes and can help to explain interesting physical phenomena that are only hinted at in experiments.

Condensed matter physics, at low energies, is governed by the quantum mechanics of electrons and nuclei. Quantum electrodynamics is the best theory for describing the quantum mechanical interactions of phenomena not dependent on nuclear or gravitational forces. In principle any system can be modelled quantum mechanically by solving the Schrödinger equation:

$$H\Psi \;= (H_{\mathrm{K}} + H_{\mathrm{P}})\Psi \;=\; (E_{\mathrm{T}})\Psi, \tag{31}$$

where H is the Hamiltonian of the Schrödinger equation, H_{K} is the kinetic energy operator, H_{P} is the potential energy operator and Ψ is the many body wave function for all particles, $\Psi(\mathbf{r_1}, \mathbf{r_2}, ..., \mathbf{r_N})$, both electrons and nuclei. The kinetic energy can be calculated separately for each particle as a function of the wave function by the Equation:

$$H_{\mathrm{K}} = \; -\sum_{i=1}^{N} \frac{\hbar^2}{2m_i}\nabla_i^2, \tag{32}$$

where for each particle, i, the mass is given by m_i and ∇_i is a Laplace operator giving the derivative of the wave function with respect to position [75]. The potential energy of the system is more complex, depending upon the Coulomb interactions between particles. Its calculation can be summarised as follows:

$$H_{\mathrm{P}} = \sum_{i \neq j} \frac{e^2}{4\pi\epsilon_0} \frac{Z_i Z_j}{|\mathbf{r_i} - \mathbf{r_j}|}, \tag{33}$$

where $Z_{i,j}$ contains the scale and sign of each particle. If the two particles are both nuclei or both electrons then the interaction is repulsive whereas, if they are a nucleus and an electron, then the interaction is attractive. Studying Eq. (32) and Eq. (33) it is clear to see why almost all systems are analytically impossible to calculate. Although the kinetic energy contributions scale linearly with particle number, the potential energy contributions scale combinatorially. Additionally calculations of the Schrödinger equation must be carried out repeatedly throughout the real space volume of any system to completely specify state. This leads to the complete specification of the many-body wave function in Eq. (31), requiring $N_{\mathrm{points}}^{N_{\mathrm{electrons}}+N_{\mathrm{nuclei}}}$ complex numbers [75]. Sampling every 0.35Å across the unit cell of $\mathrm{NaCoO_2}$ requires calculating at ~ 3000 points and as the compound contains 8 nuclei and 108 electrons, this would require 10^{403} complex terms. This cost is obviously so prohibitive that only the simplest systems have been solved.

3.1 Density Functional Theory

Over the years there have been numerous attempts to simplify the solution to Eq. (31) so that materials can be studied effectively. Shortly after the formulation of the Schrödinger equation, Thomas [76] and Fermi [77] proposed independently a statistical model that represented the electronic structure as a density which was uniform over each small volume unit but varied from each volume unit to the next allowing the approximation of non-uniform electron distributions. Small improvements were made over the following decades. However it was not until 1964 that Density Functional Theory was introduced when Hohenburg and Kohn showed that the external potential of an inhomogeneous electron gas could be uniquely determined by the electron density and a constant [78].

When everything is in its ground state, the energy of the system depends only on the electron density making it a functional of the density, $E = F(n)$, and giving rise to the name Density Functional Theory (DFT). Fifty years after the publication by Hohenburg-Kohn paper, over 100,000 articles have been published using DFT in a wide range of fields indicating the unparalleled impact of DFT on the application of quantum mechanics to chemistry and physics [79]. Although there are many different implementations of DFT, this chapter will focus on the plane-wave basis set protocol used by the CASTEP code [80].

3.1.1 Approximations of the Schrödinger equation

Before the contributions of Hohenburg, Kohn and Sham can be explained, a number of approximations will be introduced to the Schrödinger equation. The clamped nuclei approximation [75] states that in comparison to the electrons the nuclei are considered to be stationary, therefore the kinetic energy of the nuclei terms can be removed. As a result of the negligible kinetic energies of the nuclei, the nucleus-nucleus repulsion terms are considered to be constant. For convenience this constant is subtracted from the total energy by introducing a final energy, $E = E_{\mathrm{T}} - \hat{\mathrm{V}}_{n-n}$. Clearly this approximation can only be valid for time independent calculations and the kinetic energy of nuclei is very important in MD and phonon calculations. It is useful to rewrite Eq. (31) in terms of the electron kinetic energy, the electron-electron repulsion,$\hat{\mathrm{V}}_{e-e}$, and an external potential due to the electron-nuclei interaction,$\hat{\mathrm{V}}_{ext}$:

$$\left(\sum_{i=1}^{N}\frac{1}{2}\nabla_i^2+\sum_{i\neq j}\frac{1}{2}\frac{1}{|\boldsymbol{r}_i-\boldsymbol{r}_j|}+\sum_{i,I}\frac{Z_I}{|\boldsymbol{R}_I-\boldsymbol{r}_i|}\right)\Psi = \;E\Psi, \tag{34}$$

where i and j are lists of all electrons, I and R_I is the list of nuclei and their positions. The range of constants preceding the kinetic and potential terms, Eq. (32) and Eq. (33), are simplified by converting into Hartree atomic units via the relationship, $E_{Hartree} = \frac{e^2}{4\pi\epsilon_0 a_0}$. The units were created to eliminate various universal constants and to avoid high powers of 10 in numerical work [81].

The second major assumption is the way that the wave functions are handled. In 1927, Hartree formulated an approximation where instead of using a many-body Hamiltonian, the interactions between electrons would be neglected and instead an approximate potential is added to correct for the lack of repulsive forces between electrons [82]. In effect the many-body wave function is replaced with a series of non-interacting single-electron wave functions and a compensating Hartree potential which depends on the total electronic density. Eq. (34) becomes:

$$\left(\sum_{i=1}^{N}\frac{\nabla_i^2}{2}+\int d\boldsymbol{r}'\frac{n(\boldsymbol{r}')}{|\boldsymbol{r}'-\boldsymbol{r}|}\;+\sum_{i,I}\frac{Z_I}{|\boldsymbol{R}_I-\boldsymbol{r}_i|}\right)\phi_i = \;E\phi_i, \tag{35}$$

where the second term of the LHS is the Hartree potential dependent on the electron density, $n(\boldsymbol{r}') = \sum_i |\phi_i(\boldsymbol{r})|^2$ for all occupied states and ϕ_i is the single electron wave function of the i^{th} electron related to the many body wave function by:

$$\Psi(\boldsymbol{r}_1,...,\boldsymbol{r}_n) = \phi_1(\boldsymbol{r}_1)...\phi_n(\boldsymbol{r}_n). \tag{36}$$

The treatment of the electrons as independent of each other, obtains the lowest ground state energy by filling one electron at a time from the lowest ground state eigenvalue available. This method of filling preserves the Pauli Exclusion Principle.

The wave functions of the electrons, including the spin, are described using a Slater determinant matrix. Each electron has a wave function which is described in the matrix by its quantum numbers n, m, m_l, m_s, and its real space coordinates and spin state [83].

The Hartree-Fock equation is obtained by adding an extra potential to Eq. (35) which prevents two electrons from occupying the same quantum state. The right hand potential is non-local as it involves an integration over $\mathbf{r}'$, complicating the solution. A derivation can be found in [75] however the Schrödinger equation becomes:

$$\left(\sum_{i=1}^{N}\frac{\nabla_i^2}{2}+\int d\boldsymbol{r'}\frac{n(\boldsymbol{r'})}{|\boldsymbol{r'}-\boldsymbol{r}|}\ +\sum_{i,I}\frac{Z_I}{|\boldsymbol{R}_I-\boldsymbol{r}_i|}\right)\phi_i-\sum_j\int d\boldsymbol{r'}\frac{\phi_j^*(\boldsymbol{r'})\phi_j(\boldsymbol{r})\phi_i(\boldsymbol{r'})}{|\boldsymbol{r}-\boldsymbol{r'}|}=\ E\phi_i, \tag{37}$$

where the sum of the final term is over occupied states with the same spin as ϕ_i. It should also be noted that the second term contains an integration over $\mathbf{r}'$ however this term describes the mean field and is local.

This presence of the non-local potential makes the solution to the Hartree-Fock equations too complex and instead in 1965 Kohn and Sham [84] postulated that the electrons could be replaced by a system of non-interacting electrons of the same density with an unknown additional term V_{xc} containing the exchange and correlation contributions within which would also contain any other differences that arise between the two interpretations, for example from the kinetic energy being modelled as a non-interacting system. The Kohn-Sham equations are expressed as a series of single electron wave functions, ϕ_i, that minimise the energy functional:

$$\left(\frac{\nabla_i^2}{2}+V_H(\boldsymbol{r})+V_{\text{ext}}(\boldsymbol{r})+V_{\text{xc}}(\boldsymbol{r})\right)\phi_i=\ E_i\phi_i. \tag{38}$$

The final term of the LHS contains everything that is not explained by the independent-electron approximation and has the form $V_{\text{xc}}=\left.\frac{\delta E_{\text{xc}}(n)}{\delta n}\right|_{n(\boldsymbol{r})}$. In theory there is an exact

E_{xc} that would describe any system. However, in practice, this is unknown and instead there are multiple approaches to creating the best match for the required calculation.

3.1.2 Exchange-Correlation Correction

The simplest method to model the contribution from exchange and correlation is the Local Density Approximation, LDA, which was first described by Ceperley and Alder [85]. LDA calculates the exchange correlation energy at different points using the assumption that the energy per electron is equal to the same energy that electron has if it were in a homogeneous electron gas of the same energy [84], stated as:

$$E_{\mathrm{xc}}\big[n(\boldsymbol{r})\big] = \int \epsilon_{\mathrm{xc}}\big(n(\boldsymbol{r})\big)\ n(\boldsymbol{r})\ d\boldsymbol{r}. \tag{39}$$

The correlation term, ϵ_{xc}, needs to be numerically calculated using a Monte Carlo method. It is considered that this produces an accurate representation except where the density varies rapidly. A detailed description of the early progress in defining suitable E_{xc} values for the local density approximation is given in a review article by Jones and Gunnarsson [86].

Comparisons of the ground state potentials derived from exact numerical and LDA calculations have shown a substantial systematic error in the LDA value although the error in the exchange-correlation energy is smaller, typically underestimated by around 10% [87]. This error leads to over-binding of bonds [88]. For accurate modelling of systems it is necessary to use better approximations to the ground state potential. A widely used solution is the Generalised Gradient Approximation, GGA, which models the differential of the density at each point.

GGA considers the gradient of the electron density allowing for non-locality in the description of exchange and correlation [89]. GGA first developed as a gradient correction to the LDA method [90]and there have since been many approaches to model the density. The methods of calculating the parameters differ between approaches and can be a source of additional bias. The order of the equation which calculates the density fluctuation also changes between approaches. However, typically, they tend not to go beyond second order equations. The Exchange-Correlation energy can be expressed as:

$$E_{\mathrm{xc}}^{\mathrm{GGA}}\big(n(\boldsymbol{r})\big) = \int \epsilon_{xc}\big(n(\boldsymbol{r}), \nabla n(\boldsymbol{r})\big)\; n(\boldsymbol{r})\; d\boldsymbol{r}. \tag{40}$$

The calculations contained in this thesis used the spin polarised Perdew-Burke-Ernzerhof generalized gradient approximations [91]. More functionals have been proposed creating a ladder of functional forms increasing in complexity of which LDA and GGA are the two lowest rungs respectively [92].

3.1.3 Bloch's theorem

The use of periodic boundary conditions removes the necessity to have a large number of ions to simulate a near infinite cell. Instead the smallest number of ions that represent the properties of the system are chosen and then replicated. For the direct, real space, lattice the repeating unit is the unit cell. For the reciprocal space the repeating unit is the Brillouin zone. The origin of the repeating unit in reciprocal space is the Brillouin zone centre, and the border between repeating units is the Brillouin zone boundary. Interactions continue across the boundaries creating an infinite volume. Using Bloch's Theorem, the electron wave functions can be described according to its repeated position within the lattice as:

$$\phi_k(\boldsymbol{r}_{\mathrm{position}} + \boldsymbol{r}_{\mathrm{lattice}}) = \exp(ik(\boldsymbol{r}_{\mathrm{lattice}})\phi_k(\boldsymbol{r}_{\mathrm{position}}), \tag{41}$$

where $\boldsymbol{r}_{\mathrm{lattice}}$ is the lattice position and $\boldsymbol{r}_{\mathrm{position}}$ is the position within that repeated unit cell, defined in Section 2.2. The same point in two adjacent unit cells is therefore scaled only by a exponential factor that depends on the value of $\boldsymbol{r}_{\text{lattice}}$. To enhance the speed of calculations the Hamiltonian of the Kohn-Sham equation is rewritten in terms of cell periodic quantities. A periodic function $u_k(\mathbf{r})$ is introduced which allows Eq. (41) to be restated as:

$$\phi_k(\boldsymbol{r}_{\text{position}}) = \exp(ik.\boldsymbol{r}_{\text{position}})u_k(\boldsymbol{r}_{\text{position}}). \tag{42}$$

The wave vector **k** features prominently in these equations and therefore it makes sense to consider the reciprocal lattice of the simulated cell. In Section 2.1 the reciprocal lattice is discussed in relation to diffraction. The energy of the system is sampled at regular positions across reciprocal space, known as k points, according to the shape and size of the Brillouin zone. These are chosen using the Monkhorst and Pack formalism [93] which uses a regular grid in 3D space. A compromise is needed when modelling a system between the quality of the sampling and the calculation time. Increasing the number of k points increases the accuracy in the energy, but takes longer to calculate. Larger real space cells require fewer k points than smaller cells, as the size of the Brillouin zone in reciprocal space is smaller.

3.1.4 Plane Wave Basis Set

It is essential to have a well described electron orbital as this will directly affect bond lengths and other interactions. Basis sets are used to model the single electron wave function as they are easily combined to create a numerical representation of an orbital.

$$u_k(\boldsymbol{r}) = \sum_{i=1}^{N} c_{k,i}\ f_i(\boldsymbol{r}), \tag{43}$$

where for each single electron wave function, a series of functions f_i, up to a finite number $i = N$, are used to describe the orbital. The periodic function, u_k, naturally fits into this formulation to ensure the periodic boundary conditions of the system are maintained. There are several different functions that can be used as basis sets, however, only the plane wave basis set is discussed here:

$$u_k(\boldsymbol{r}) = \sum_G c_k(G)\, \exp(\mathrm{i}G.\boldsymbol{r}), \tag{44}$$

where G is a regular grid of points in reciprocal space related to integer value spacings of the reciprocal lattice. The greatest advantage of the plane wave basis set formalism is that basis sets have the same form as a Fourier series. If Eq. (44) is substituted into Eq. (42) then an equation for each orbital in terms of plane waves is derived:

$$\phi_k(\boldsymbol{r}) = \sum_G^{|G|<G_{\max}} c_k(G)\, \exp(\mathrm{i}(k+G)\ .\ \boldsymbol{r}). \tag{45}$$

$G_{\max}$ is a limiting value that can be altered to converge the system energy to a desired accuracy. This truncation is possible as the coefficients of the plane wave with small kinetic energy have a much greater contribution than those with large kinetic energy. The relationship with a Fourier series allows for the quick transformation into real space coordinates as required by the Kohn-Sham equations. In reciprocal space, Eq. (38) becomes:

$$\sum_{G'} \Big(\frac{|k+G|^2 \delta_{GG'}}{2} + V_H(G-G') + V_{\mathrm{ext}}(G-G') + V_{\mathrm{xc}}(G-G') \Big) c_{i,k+G} = \ E_i c_{i,k+G}. \tag{46}$$

The Hamiltonian matrix can be solved by diagonalisation [94]. The use of Fast Fourier Transforms, first proposed by by Cooley and Tukey, greatly speeds up calculation of the matrix by reducing the number of procedures in a $N \times N$ matrix proportionally from N^2 to $NlogN$ [95]. A description of the Fast-Fourier-Transform method and its history is given by Cooley et al. [96].

The limiting factor $G_{\max}$ is often written in terms of a plane-wave cut-off energy that is given by:

$$E_{\mathrm{c}} = \frac{\hbar^2 G_{\max}^2}{2m_e}. \tag{47}$$

In reciprocal space this draws a boundary similar to that of the Ewald sphere within which any lattice point G producing energies less than E_c is kept.

3.1.5 Pseudopotentials

The accurate modelling of electron wave functions is of paramount importance in determining the bonding between ions. Early in the 20^{th} century the work of Lewis [97], and others, suggested that the chemical bonding could be described by a non-interacting kernel of electrons surrounded by a shell of interacting electrons. Today, this reasoning forms the basis of the theory for pseudopotentials which was proposed in 1959 by Phillips and Kleinman [98].

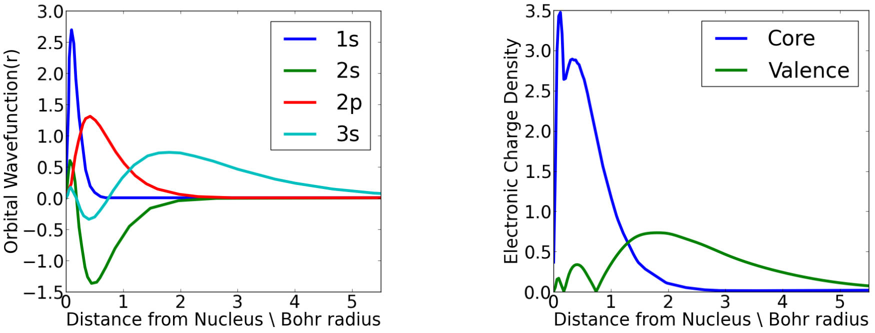

(a) Orbital probability distributions.

(b) Electron charge density.

Figure 19: Approximations of the probability distributions for the electron orbital wave functions of a Na atom, adapted from [99]. Na ions have a total of 11 electrons, arranged with 2, 2, and 6 electrons into the core 1s, 2s and 2p orbitals respectively, while the single valence electron is in the 3s orbital. The charge density of the core electrons is shown to be centred close to the nuclei while the density of the valence electron is centred further out.

Approximations of the electron orbital wave functions of an isolated Na atom are shown in Figure 19a. Different electron orbitals localise over a wide range of distances from the nuclei. Typically though, the higher the orbital the further it localises away. Figure 19b splits these orbitals into core, tightly bound, and valence, non-local, orbitals. In this case the 1s, 2s and 2p orbitals form the core and the valence region is formed by the single electron in the 3s orbital. In most ions the core contains the majority of electrons and is considered to have a negligible role in bonding and can be removed or neglected by the use of pseudopotentials, speeding up calculations.

A pseudopotential is created by defining a pseudization region, from the nucleus origin to a cut-off value r_c, within which the wave function is modelled by a smooth and nodeless function, while outside it agrees with the all electron wave function [99]. This pseudo-wave function is defined to be a solution of the Kohn-Sham equations, given a particular pseudopotential. The contribution of the core electrons is contained within the pseudo-wave function, and therefore a condition is that the electron density between $0 < r < r_\mathrm{c}$ is equivalent to that calculated by the all electron wave function.

The value of r_c must be carefully chosen to reflect the distinction between core and valence electrons. A low value may create a more accurate but expensive calculation while a high value may be inaccurate, leading to poor modelling of bonds between ions. The value depends on the locality of the orbitals involved in bonding determined by calculating the all electron wave function in isolation. Beyond the cut-off the potential should coincide with the Coulomb potential of the nucleus with a charge state given by the number of valence electrons [99].

Pseudopotentials are designed with a given hardness in mind. This can be interpreted as how well the pseudopotential matches the real wave function particularly close to the nuclei. In general a hard pseudopotential will require a larger number of plane waves to describe it and therefore a higher cutoff energy. A soft pseudopotential can be effective in describing a system if the interactions between neighbouring ions are sufficiently damped at the distance at which the real wave function begins to differ from that of the pseudopotential.

In this thesis Vanderbilt type [100] ultrasoft pseudo-potentials have been used. They are designed to minimise the amount of computational resources used by having a low cut-off energy, being highly transferable and being able to produce metallic, ionic and covalent bonding behaviour. The low calculation cost is achieved by neglecting the condition that the electron density between $0 < r < r_\mathrm{c}$ is equivalent for the all electron wave function and the pseudo-wave function. Instead an augmentation charge is added that represents the missing density, and has non-zero values only within $0 < r < r_\mathrm{c}$. The augmentation charge however leads to some further complications when it comes to defining the plane wave cutoff G_max. For this purpose a standard grid is used in relation to the G values of the pseudopotential and a larger fine grid is used in relation to the augmentation charge.

3.2 CASTEP

CASTEP is one of the leading codes for the calculation of the properties of materials from first principles. It has been used to simulate a wide range of properties including structure, energetics, vibrational and electronic response [101]. In this thesis CASTEP has been useful in calculating the ground state structures of materials and carrying out molecular dynamics and transition state search calculations. The following is a description of the underpinnings of the various types of calculation necessary for this task.

3.2.1 Single Point Energy Calculation

Single Point Energy Calculations are the simplest of the tasks carried out in CASTEP and the methods used underpin all other calculations. Their purpose is to calculate the energy of a fixed system of ions by creating a self-consistent solution that minimises the Kohn-Sham functional.

The procedure for solving the Kohn-Sham equations begins by stating the coordinates of the nuclei and calculating the nuclear potential. A first guess for the electron density is then added based on the densities expected for completely isolated ions [75]. The total potential can be calculated from the resultant Hartree and exchange-correlation potentials. The solutions of the Kohn-Sham equation provide the wave functions that are then used to create the next electronic density. The Self Consistent Field (SCF) cycles continue until the new density equals the old density to a given accuracy, known as the electron energy tolerance.

The method of electronic relaxation used by CASTEP based on iterative SCF cycles is described fully in Ref.[102]. The number of cycles is reduced by introducing a stabilising mixing term. After each renewal of the cycle a portion of the old electronic density is mixed in with the newly calculated density. This serves to prevent the system oscillating between two slowly converging positions. The mixing proportion should be carefully chosen as it is dependent on the particular atoms of the system. The possible mixing schemes are Linear, Kerker, Broyden and Pulay mixing with Pulay being the most efficient. In the Pulay scheme the new input density is obtained from a linear combination of several previous steps. It is controlled by the mixing amplitude, the cut off $G_{\max}$, and the number of previous steps.

In metallic systems the occupation of bands can change depending on the position within the Brillouin zone. Unlike with insulators, it is necessary to include partial occupancies to eliminate discontinuous changes that occur in the energy when an energy band crosses the Fermi surface. In CASTEP this is handled by applying a Gaussian smearing to each energy level. The occupancy of each level is determined dependent on how much of the Gaussian is above the Fermi level. This effectively gives the electrons a finite temperature [103].

To test the accuracy of any calculation it is necessary to investigate the values used to define the simulation. In section 3.1.4 the necessity of a suitable cut off energy, E_c, is stated given it affects the generation of wave functions built from plane wave basis sets. The outputs of calculations with differing E_c can be compared, and the value considered rigorous if the outputs are converged within a suitable criterion. Similarly, tests are carried out on the size of the standard grid, the fine grid and the spacing of k points along each reciprocal lattice vector.

Parameters associated with the mixing of the electronic and spin properties of the material between SCF cycles are also tested. Instead of converging with respect to the total energy, the convergence will be with respect to the number of SCF cycles. This is particularly important for simulations where many similar calculations are being carried out, which all involve their own series of SCF cycles, for example at each step of a molecular dynamics simulation.

3.2.2 Geometry Optimisation

A Geometry Optimisation calculation attempts to optimise the positions of all nuclei to find the global ground state. The atoms are moved according to the forces applied on to them by the neighbouring atoms. The forces can be calculated as a derivative of the total energy with respect to the ionic positions:

$$\boldsymbol{F}_I = -\frac{dE_\mathrm{total}}{d\boldsymbol{R}_I}. \tag{48}$$

Importantly this is the derivative of the total energy including the electrostatic repulsion between ions, V_{n-n}, that was subtracted from the Kohn-Sham equations previously. The Hellmann-Feynman theorem [104, 105] proved that the force could be calculated from the derivative of the average energy of the system, $\hat{\mathrm{E}} = \int \phi^* H \phi dr$, as follows:

$$\frac{dE_{total}}{d\boldsymbol{R}_I} = \int \phi^* \frac{\partial H}{\partial \boldsymbol{R}_I} \phi \; d\boldsymbol{r} + \int \frac{\partial \phi^*}{\partial \boldsymbol{R}_I} H \phi \; d\boldsymbol{r} + \int \phi^* H \frac{\partial \phi}{\partial \boldsymbol{R}_I} \; d\boldsymbol{r}. \tag{49}$$

Using the property of the Hamiltonian as a self adjoint operator it can be shown that the last two terms will cancel each other out. The derivative of the Hamiltonian is then related to the potential by $\frac{\partial H}{\partial \boldsymbol{R}_I} = \frac{\partial V}{\partial \boldsymbol{R}_I}$, therefore the force can be rewritten solely in terms of an integral of the derivative of the potential:

$$\boldsymbol{F}_I = -\int \phi^* \frac{\partial H}{\partial \boldsymbol{R}_I} \phi \; d\boldsymbol{r} = -\int \phi^* \phi \frac{\partial V}{\partial \boldsymbol{R}_I} d\boldsymbol{r} = -\int \frac{\partial V}{\partial \boldsymbol{R}_I} d\boldsymbol{r}. \tag{50}$$

Applying this to the Kohn-Sham equations stated earlier, only two potentials are found to provide contributions to the force; the electrostatic potential between ions, V_{n-n}, and the external potential:

$$\boldsymbol{F}_I = -\int d\boldsymbol{r} \frac{dV_{\mathrm{ext}}}{d\boldsymbol{R}_I} n(\boldsymbol{r}) - \frac{dV_{n-n}}{d\boldsymbol{R}_I}. \tag{51}$$

In CASTEP, the optimisation of ionic positions is carried out using the Broyden-Fletcher-Goldfarb-Shannon, BFGS, algorithm to find the minimum energy geometry [106]. This method uses a quasi-Newtonian method to simultaneously relax the internal coordinates and lattice parameters of a crystal under pressure while preserving the symmetry of the structure.

The BFGS algorithm calculates the inverse of the Hessian matrix that approximates the shape of the enthalpy surface around a minimum. The exact nature of this matrix is unknown; therefore a guess is iteratively improved with each step. After each shift in the ionic coordinates a new SCF cycle is begun to calculate the new electron density and consequently the new forces. It is important to have a good starting point as it is possible for a calculation to become trapped in a local minimum if the starting setup is not close enough to the global minimum.

It is possible to apply constraints to a system undergoing a geometry optimisation. These can include preventing the movement of particular ions in certain directions. Generally, they involve fixing the lattice parameters of the simulated cell. A reason for this might be to enforce an experimentally discovered unit cell. There are many other methods to calculate the minimum energy geometry, however, the low memory version of the BFGS method [107] is the only other method used in this thesis.

3.2.3 Transition State Searches

Diffusional events in a crystalline material occur by discrete hopping events where both the start and end points are local minima. A Transition State Search can be applied to diffusional processes to find the minimum path energy between two local minima. The increase in the total energy of the system when the transitioning ion is at the saddle point of the path is equivalent to the activation energy of the hop event. For a successful calculation it is necessary that both end points are at minima which can be achieved by carrying out geometry optimisations of an initial and final guess.

The simplest method to find a transition state would be to sample the potential energy between the respective positions. If this method were to take into account deviations from the straight through path then the calculation could easily become intensive. Several methods have been proposed to reduce the resources required, for example the Nudged Elastic Band, NEB, method [108] which applies geometry optimisations, with certain constraints, to several positions along the predicted pathway. The advantage of this system is that it relies on information that is readily available in a typical DFT calculation and that it provides a nice output of the shape of the energy barrier.

Further efficiency savings are made by methods that limit the amount of calculations away from saddle point. The synchronous-transit method constructs a predicted pathway to identify the rough position of the saddle. The transition state is then progressively bound by optimising intermediate structures above and below the saddle point [109]. The most successful methods use a combination of a linear interpolation to provide an accurate guess for the saddle point before using quadratic interpolation to refine the position [110]. An in-depth discussion of the various methods is given in Ref. [111].

3.2.4 Molecular Dynamics

The prime motivation for using CASTEP in this thesis is to carry out Molecular Dynamics (MD) simulations. The motions in a system are simulated by studying the positioning of ions during a series of steps in time, ideally revealing correlated and uncorrelated behaviour. The velocity of the ions is dependent on their kinetic energy, and the temperature of the system, while the potential energy landscape determines the forces acting of the ions. New ionic positions are calculated at each time step, typically a few fs, from Newton's equations of motion using the Velocity Verlot algorithm [112]. Over a suitably long simulation time the natural oscillations of the system should be apparent, including the phonon displacements of nuclei, as well as any diffusive processes.

The system at each time step can be considered a different microscopic state, with a probability distribution given by the statistical ensemble. From statistical mechanics, physical quantities can be calculated by taking arithmetic averages of the instantaneous values generated from the molecular dynamics trajectories [113]. Ideally as the simulation time increases the calculated quantity will converge towards the measured thermodynamic property. In practice the simulation time is limited by the size of the simulated cell and the desired accuracy of the model. Additionally, the simulation time needs to be significantly longer than the physical process in question in order to study it.

There are two general methods for performing *ab initio* MD simulations; the Born-Oppenheimer and the Car-Parrinello methods, which differ in how they generate new electronic wave functions at each step. In the Car-Parrinello approach the electronic wave function is propagated over each step as classical degrees of freedom [114]. In comparison the Born-Oppenheimer method solves the Kohn-Sham equations at each time step allowing for longer time steps, which has a competitive overall efficiency despite taking slightly longer to calculate each individual time step [115] . The Born-Oppenheimer method is considered more accurate due to the recalculation of the wave function at each step in comparison to the approximate wave function used by the Car-Parrinello approach [116].

Improvements to the Born-Oppenheimer approach have been made, and applied to CASTEP, by extrapolating both the wave function [117] and the charge density [118] between steps. The extrapolations provide a major increase to the speed of the calculations by providing a good starting point at each time step. A consequence of this is that the quality of the starting point will be related to the length of the time step. This leads to longer time steps resulting in longer calculations.

MD calculations in this thesis were carried out in the canonical ensemble, preserving the number of ions, volume of the cell and temperature of the system. The temperature is controlled isothermally via a Langevin Thermostat [119]. CASTEP also offers NVE, NPH, and NPT ensembles, however, the first two were excluded as thermal control was required, and the last was considered too computationally expensive as it would require the varying of the lattice parameters, which causes additional complications due to altering the k-point and fine grid spacing.

A choice was made to regulate the temperature of the system by the Langevin method which applies a correction factor to Newton's equations resulting in stochastic dynamics instead of a Nosé-Hoover chain [120] which attaches a chain of non-interacting particles to each interacting particle. The rate over which the Langevin correction is applied corresponds to a time factor which is set to be longer than the interesting dynamics.

4 Review of Ordering in Na_xCoO_2

4.1 Hexagonal Structure

The structure of Na_xCoO_2 has been extensively studied as a function of both concentration and temperature. As well as being a viable battery material, Na_xCoO_2 has been investigated for its favourable thermoelectric properties [121], its interesting charge order dependent magnetic structures [122] and due to the presence of superconductivity in certain hydrated samples [123]. This chapter contains an extensive review of the prior studies of the concentration and temperature dependent structure of Na_xCoO_2.

The basic structure depends upon CoO_2 layers, and can form different stacking sequences dependent on the growth conditions [124]. Four single phase structures are possible; O3, O'3, P'3, and P2; with the O3 phase closely resembling the commonly used battery material, Li_xCoO_2. Using first principles and Monte Carlo approaches, Wang et al. [125] have shown that for concentrations of Na between $0.336 < x < 0.876$, the P2 structure is energetically favourable.

The P2 structure has hexagonal symmetry, $P6_3/mmc$, which is the space group 194 [126] shown in Figure 20. The Na ions are sandwiched between octahedral CoO_2 layers. The fully occupied Na_1CoO_2 system has all Na ions situated on the 2d Wyckoff position giving the stacking order ACBCABCB as shown in Figure 20c. This site is labelled the Na2 site conventionally and will be coloured blue in all diagrams.

The introduction of Na vacancies enables the possibility of a second stable site between adjacent Co ions, which is equally spaced between the 6 neighbouring O ions. This site is the 2b Wyckoff position and is labelled as the Na1 site and will be coloured red in all diagrams. The occupancies of the two sites are unequal due to the proximity of the Co ions. It is impossible for a Na1 ion to be directly next to a Na2 ion due to

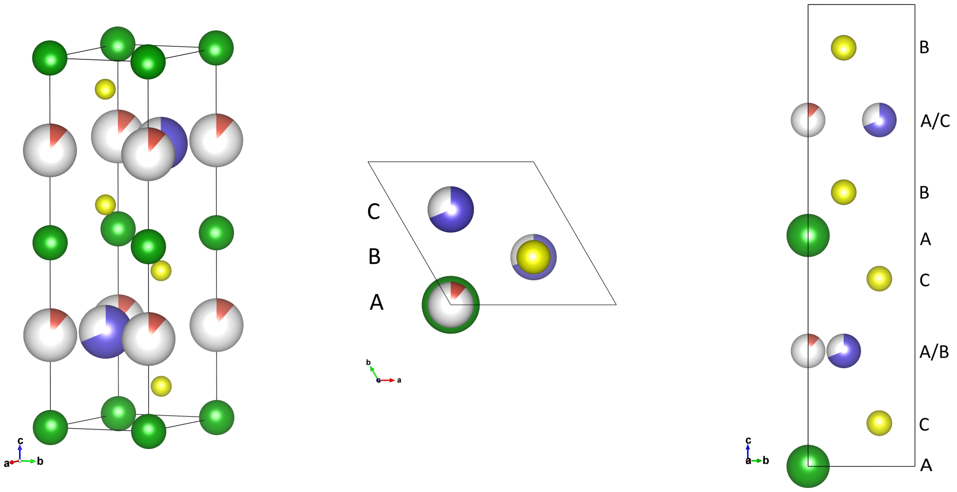

(a) $Na_{0.8}CoO_2$ unit cell.

(b) $Na_{0.8}CoO_2$ horizontal plane.

(c) $Na_{0.8}CoO_2$ vertical plane.

Figure 20: A unit cell of $Na_{0.8}CoO_2$ in the disordered phase is shown in a). The horizontal plane, b), and the vertical plane, c), are shown with the stacking order labelled alongside. The structure is P2 hexagonal with $P6_3/mmc$ symmetry. Partial occupancies of Na ions are shown with ions stable on the lower energy sites, blue, or the higher energy sites, red. This is due to the symmetrical positioning of oxygen ions, yellow, adjacent to them. The red sites are higher in energy due to the adjacent Co ions.

Coulomb repulsion [127]. The Coulomb repulsion also stops Na ions from moving into the symmetrical site between the oxygen positions.

4.2 Ordering Principles

There is an increase in potential energy for an Na ion in the Na2 site compared to the Na1 site, due to the proximity of the Co ions, leading to a clear preference for the majority of ions to be on the Na2 site. The promotion of Na ions from Na2 sites to Na1 sites can lead to an increase in average Na-Na distances, resulting in an overall lower potential energy. At low temperatures, systems order into ground states minimising the potential energy contributions from the Na-Na bonds by ordering into long range repeating structures.

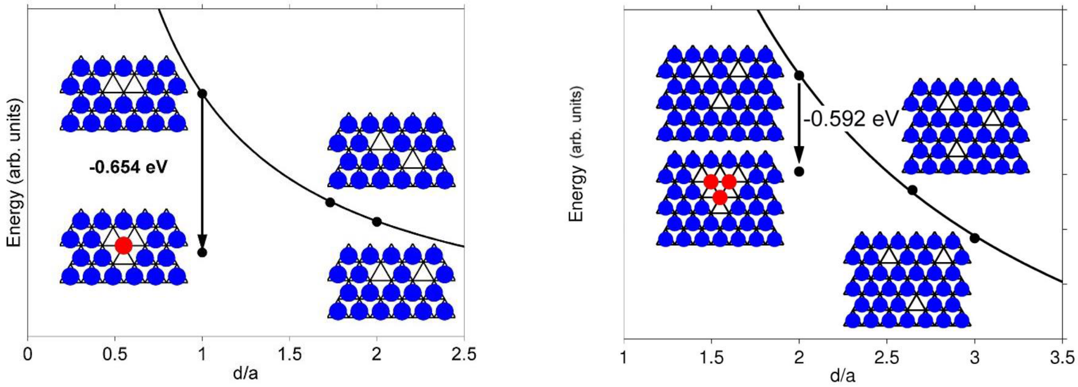

(a) Di-vacancy formation energy (b) Tri-vacancy formation energy

Figure 21: Graphs detailing the energy loss due to the formation of vacancy clusters [36]. The potential energies associated with different ionic arrangements are given, outlining the formation energies of Di-vacancy clusters a) and tri-vacancy clusters b).

Roger et al. [36] have shown in Figure 21a that an energy reduction is caused by promoting a single Na2 ion to the Na1 site. Two vacancies are required to be neighbours and therefore this is termed a di-vacancy cluster. The energy reduction occurs as the increased energy due to the Co ions adjacent to the Na ion is smaller than the decreased energy caused by the increased separation of the Na ion nearest neighbours.

Figure 21b shows the formation of a tri-vacancy cluster which involves the proximity of 3 vacancies and the promotion of 3 Na ions into Na1 sites. The energy reduction is less than in the di-vacancy case due to the interaction between the promoted ions. The Figure shows that the energy of the cluster is slightly higher than simply separating out the vacancies. At very high concentrations of Na it would not be expected that tri-vacancy clusters form. For suitably high temperature systems, the thermal energies could allow these clusters to form for short periods of time.

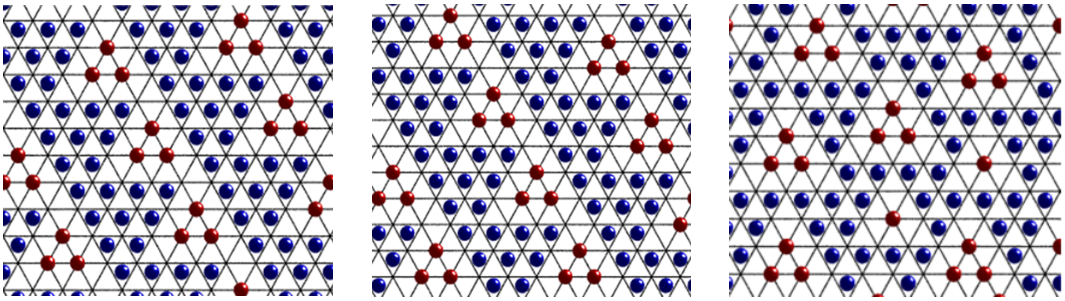

(a) In-plane ordering of Na ions in the stripe phase

(b) In-plane ordering of Na ions in the disordered stripe phase

(c) In-plane example distribution of Na in the disordered phase

Figure 22: $Na_{0.8}CoO_2$ forms superstructures at low temperatures, reducing the overall energy of the system. Beneath 280K the system is in the stripe phase, a). The Na ions arrange into stripes of tri-vacancy clusters that are ordered both parallel and perpendicular to the stripe. At 280K, the ordering perpendicular to the stripes is lost, moving the system into the disordered stripe phase, b). Above 380K, the system enters the disordered phase, c), which is characterised by a lack of long range coherence.

Although in isolation tri-vacancy clusters may be energetically unfavourable, they are possible as part of superstructures. In $Na_{0.8}CoO_2$, the arrangement of tri-vacancy clusters into long chains, Figure 22a, has been found to be favourable by Morris et al. [128]. The forming of stripes of tri-vacancy clusters is deemed to alter the topology of the electronic conduction pathways. A phase transition occurs at 280 K leading to a partial disordering, Figure 22b. Above 380 K a second phase transition occurs, Figure 22c, and the long range ordering breaks down. There is still some local ordering causing the formation of di vacancy and tri-vacancy clusters.

4.3 Ordering and Dynamics

4.3.1 Temperature Dependence

The ordering arrangements of $Na_{0.8}CoO_2$ are strongly linked to the dynamics of the system. NMR measurements, by Weller et al. [129], show that above 280 K the system becomes super-ionic. This coincides nicely with the transition from the ordered stripe phase to the disordered stripe phase seen by Morris et al. [128]. Figure 23a shows the temperature dependence of the NMR signal seen by Weller. The ^{23}Na spin-lattice relaxation rate is approximately flat up to 200 K, at which point it begins to increase slowly. At 280 K the rate is seen to jump by an order of magnitude becoming super-ionic.

Figure 23b shows the peak intensity of two satellite peaks, observed by Morris et al. [128], corresponding to the ordered stripe and disordered stripe phases. At the transition point one peak is observed to appear and the other disappears. A certain amount of hysteresis is visible in the transition, but the temperature of the transition centres on 280 K in line with the NMR results.

A second NMR study by Carlier et al. [130] concludes that the Na ions are not all mobile at room temperature. This would agree with the presence of an intermediate disordered phase. A loss of coherence between tri-vacancy clusters of different stripes is observed, while the coherence of tri-vacancy clusters along stripes is maintained. The dynamic movement observed by NMR would reinforce that in this intermediate phase, the clusters are able to move along the stripes. The static nature of some Na ions can be explained by the rows of ions separating each stripe.

Further evidence for temperature dependent diffusion regimes can be seen in the

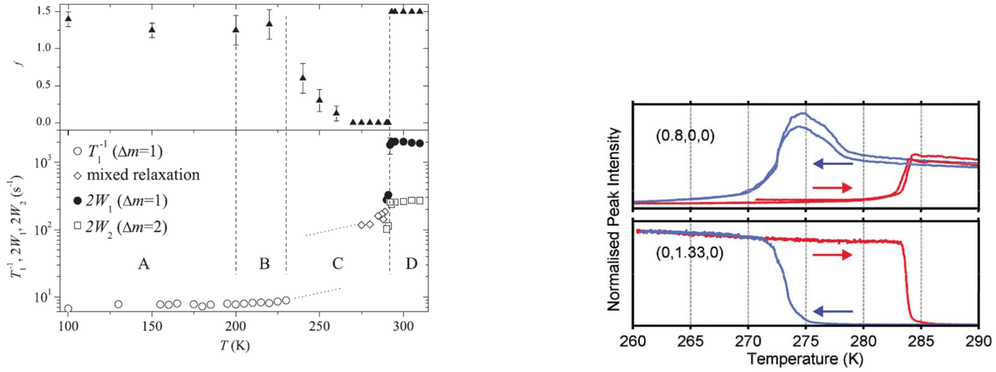

FIG. 3. The upper panel contains the relative intensity f of the satellites with respect to the central line. In the lower panel, ^{23}Na NMR spin-lattice relaxation rates of $Na_{0.8}CoO_2$ between 100 and 310 K are shown. The different regimes (A-D) are explained in the text.

(a) NMR spin-lattice relaxation rates against temperature [129] showing that $Na_{0.8}CoO_2$ becomes super-ionic at 280K.

(b) Intensity of Bragg peaks with increasing temperature associated with the ordered and disordered stripe phases of $Na_{0.8}CoO_2$ [128].

Figure 23: The appearance of super-ionic behaviour shown in the NMR data, a), coincides with b) a phase transition observed in $Na_{0.8}CoO_2$.

experiment by Medarde et al. [131]. They carried out high resolution neutron powder diffraction measurements of a $Na_{0.7}CoO_2$ sample at different temperatures. The lattice parameters of the basic unit cell were refined and the hexagonal symmetry was observed to be broken in low temperature phases. From the refinements they are able to create Fourier maps in each phase describing the scattering density across the whole unit cell volume.

The positioning of scattering density informs us of the nature of the diffusion events occurring. In the lowest temperature phase, Figure 24a, only small amounts of scattering density are observed away from the Na1 and Na2 sites which is interpreted as the system showing no diffusive motions between different sites. When the temperature is increased to 350K they note the development of scattering density along a pathway corresponding to continuous Quasi-1D motion of ions between Na1 and Na2 sites, Figure 24b. The directionality of the hops is determined by the symmetry of the system which makes the accessible pathways shorter.

At 450 K the system symmetry is hexagonal and the diffusion becomes 2D as all Na1 to Na2 hop lengths are equivalent, Figure 24c. The diffusion in all cases is from Na1 to the Na2 sites and vice versa. No intensity pathways are seen elsewhere, although a small intensity is visible in the 1D diffusion phase between the O ions. Although the concentration is different than the $Na_{0.8}CoO_2$ stripe system, the temperature dependence of dynamic processes are determined by the activation barrier between hops so the diffusion rates should be broadly similar. The change in symmetry resulting in shorter path lengths may serve to lower the activation energy, enhancing diffusion rates.

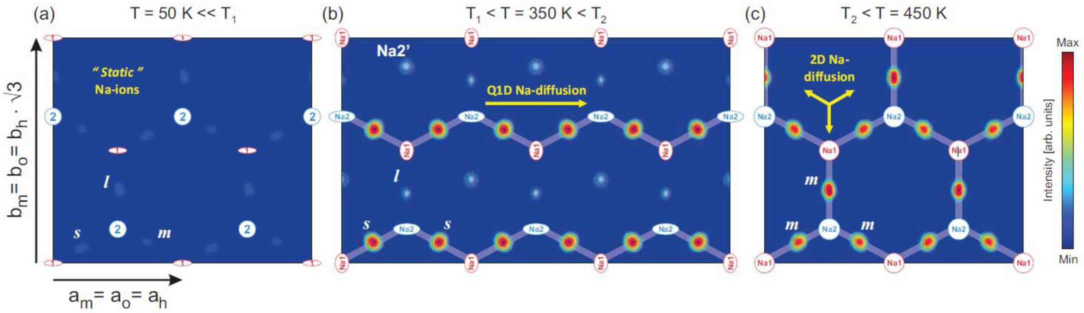

FIG. 4: (Color online) Fourier difference maps of the $z = 0.25$ Na planes at $T = 50$, 320 and 450 K showing the evolution of the residual scattering density in the paths connecting the Na1 and Na2 sites (scale top/bottom: 0.25/0.0875 Fermi). For the three temperature regions there is a clear evolution from (a) Static Na ions, to (b) Quasi-1D ion diffusion along the $\mathbf{a}_o$-axis to finally (c) fully 2D ion diffusion. Thick solid white lines are overlayed together with the Na-ion positions in order to emphasize the diffusion paths. The shape of the Na ions has been adapted to the thermal ellipsoids previously shown in Fig. 3 and the different Na1-Na2 distances (l, m ,s) from Fig. 2(a) are also indicated.

Figure 24: Fourier maps of the scattering density of $Na_{0.7}CoO_2$ in the Na plane, studied by Medarde et al. [131]. Clear changes in the location of scattering density with temperature are attributed to different dynamic regimes.

4.3.2 Concentration Dependence

The ordering of Na as a function of concentration has been studied numerous times by different groups. A variety of techniques have been used to probe the superstructures, including electron diffraction of the $Na_{0.5}CoO_2$ concentration [132], and more generally over the the range $0.15 < x < 0.75$ by Zandbergen et al. [133]. Zandbergen notes that the structural principle for the ordering schemes results in the presence of lines of Na ions, rather than simply maximising Na-Na separations. The superstructures of $x = 0.71$ and $x = 0.84$ have also been studied by both X-ray [134] and electron diffraction [135], identifying peaks associated with $\sqrt{12}a$ and $\sqrt{13}a$ periodic structures. These are interpreted in relation to vacancy clustering and a model is provided of the Na ion positions.

Computational techniques have been used to identify the superstructure of Na_xCoO_2 as they are effective in simulating the ground state energy of different possible structural arrangements. Zhang et al. [136] have shown DFT simulations that agree well with the electron diffraction experiments of Zandbergen et al.[133]. They indicate that the driving forces are screened electrostatic interactions and that the Co ions electronic structure plays no role in determining the Na ordering. Instead, it is the intra-planar Na-Na interactions that have the largest effect.

Calculations have also been carried out by Hinuma et al. [137] which have identified different superstructures above the $x = 0.50$ concentration. Figure 25 shows some of the structures calculated by Ceder for these concentrations. At $x = 0.50$, Hinuma predicts the experimentally observed superstructure consisting of alternating Na1 and Na2 occupied sites. At increased concentrations, different arrangements of di-vacancy clusters are observed with decreasing ratios of Na1/Na2 ions. Hinuma calculates that the first tri-vacancy cluster dominated structures will appear for Na concentrations of

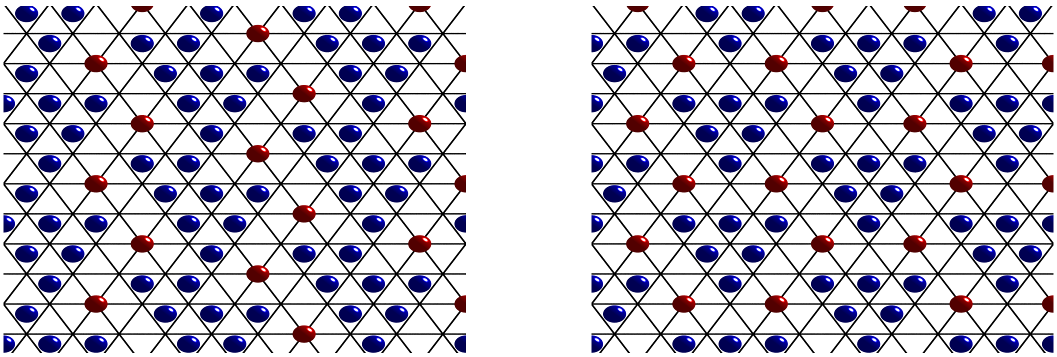

(a) The predicted $Na_{0.71}CoO_2$ phase.

(b) The predicted $Na_{0.67}CoO_2$ phase.

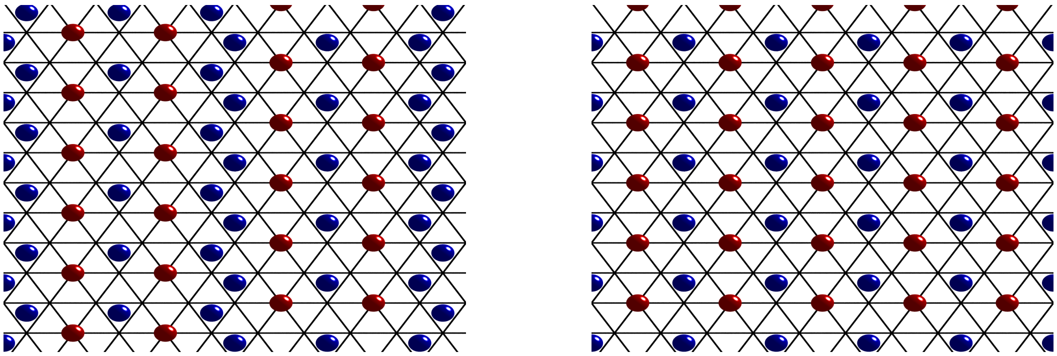

(c) The predicted $Na_{0.56}CoO_2$ phase.

(d) The predicted $Na_{0.50}CoO_2$ phase.

Figure 25: The in-plane ordering of Na ions for several phases of Na_xCoO_2, based on predictions by Hinuma et al. [137]. The concentrations are chosen to coincide with the Na concentration range shown in Figure 26.

0.77 and greater. It is also stated that above $x = 0.81$ the lowest energy arrangements are in the O3-Na_xCoO_2 formations.

The different arrangements of Na ions in Na1 and Na2 sites can be interpreted as hindering or helping long range diffusion. In the $x = 0.50$ system, the structure lends itself to having dynamic corridors of Na ions separated from each other by static Na2 ions. The diffusion of ions, or holes, is favourable in the vertical direction of Figure 25c due to the continuous lower overall Na concentration. The $x = 0.71$ structure, Figure 25a, by contrast has no corridors for diffusion. A possibility is that diffusion of ions would occur between the chains of di-vacancy clusters, however the arrangement of the Na2 ions inhibits this in most directions.

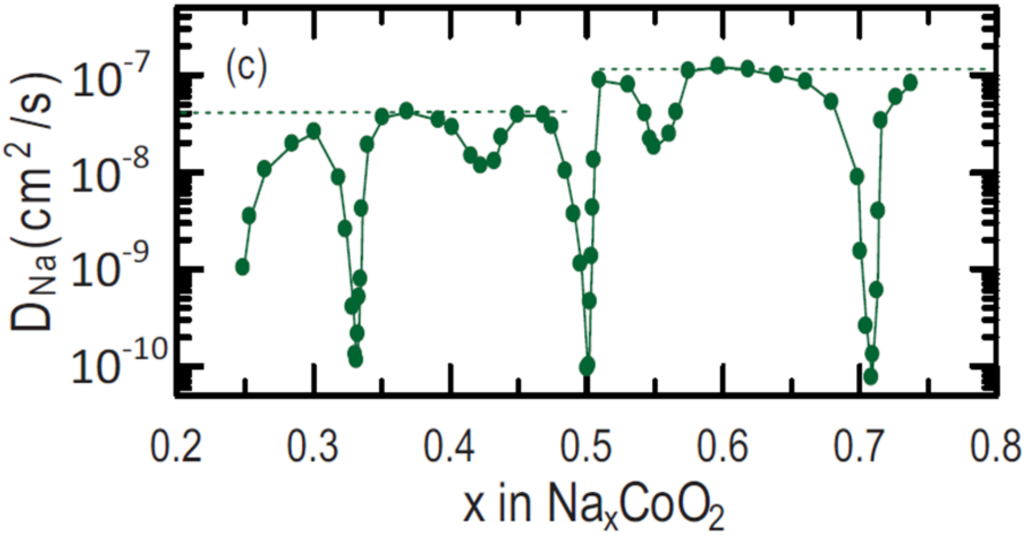

Figure 26: PITT measurement reproduced from Shu and Chou [41]. Each point marks a step in the potential difference applied between the cathode and anode. Ions move in response to the field, generating a current. For small potential steps the current is proportional number of charge carriers that diffuse between the electrodes. The time it takes the system to equalise the potential and the number of ions in motion provides a measure of the diffusion rate.

An electrochemical Potentio-static Intermittent Titration Technique, PITT, experiment of a bulk Na_xCoO_2 sample by Shu and Chou [41] determined the ionic diffusion behaviour as a function of concentration. The Na_xCoO_2 sample was mounted between platinum plates and placed in an electrolyte solution as a cathode. A very small potential difference is created between the cathode and anode resulting in the sample intercalating or de-intercalating ions in the same way a battery would as it charges or discharges. In response to the movement of ions a small current is generated which declines over time as the potential difference is equalised. For a small concentration change, the current can be integrated over time to give the total charge, equivalent to the number of ions which have entered or left the system. The time it takes to equalise the potential difference provides a measure of the diffusion rate.

Figure 26 shows their main result of the diffusion rate against concentration. There is a general decrease, around an order of magnitude, in the diffusion rate with decreasing concentration. Greater dips of several orders of magnitude are seen at specific concentrations corresponding to the superstructures predicted by Hinuma. In particular the superstructures at concentrations of $x = 0.5$ and $x = 0.71$ are seen to have a large effect while the concentration of $x = 0.56$ has a much smaller effect which supports the idea that certain arrangements may impede the diffusion of ions due to a lack of available pathways.

The broadness of certain dips may be linked to the presence of incommensurate phases. Above $x = 0.5$ several structure formations are predicted and experimentally an incommensurate region has been observed by Manoj Pandiyan in his thesis [40] for Na concentrations between $0.54 < x < 0.61$. This manifests as a region in which the Bragg reflections were seen to move continuously as the sample was de-intercalated.

4.4 Diffuse Scattering

Short range local ordering of ions leads to diffuse scattering. The coherence between ions contributes to constructive interference in the scattered wavefunction similar to the coherent elastic scattering that causes the sharp Bragg peaks. However, as there is no long range ordering the intensity is scattered diffusely in reciprocal space, hence the name. Diffuse intensity is observed in specific regions in reciprocal space, according to the dimensionality and orientation of the ordering in real space. From the location of the scattered intensity, and generally with regard to the Bragg peaks, an approximation of the local ordering can be determined.

In the disordered phase of $Na_{0.8}CoO_2$ there is short range coherence resulting from the tri-vacancy and di-vacancy clusters. These give visible diffuse scattering in both X-ray, such as Figure 27, and neutron diffraction patterns. A technique for determining the structure of the local ordering is Reverse Monte Carlo (RMC) which makes it possible to model the necessary arrangements of ions needed to create the diffraction pattern.

In RMC simulations, a system modelled on the basic unit cell is replicated many times and populated with a large number or ions and vacancies, such that it mimics the long range ordering while allowing for short range ordering without self-coherent effects occurring across boundary conditions. The atoms are refined from their starting positions by moving them and re-evaluating the diffraction pattern. If the new calculated diffraction pattern is a better match to the experimental pattern then the change is kept. If it is not, then there is an acceptance probability that the change is not accepted.

This method encourages the system to refine towards better matching structures, however the use of the acceptance probability allows the system to escape local ground states. Over time the acceptance probability is reduced, converging the system to a ground state by making it less likely to escape. This process is repeated over many steps until a suitable match is achieved. Additionally, the whole simulation is typically run from a significant number of different starting positions with the results of each simulation compared.

The Bragg peaks of a superstructure will match with a commensurate hexagonal grid of $\mathbf{a}^*/N$ where N is an integer multiplied by the simple hexagonal lattice param-

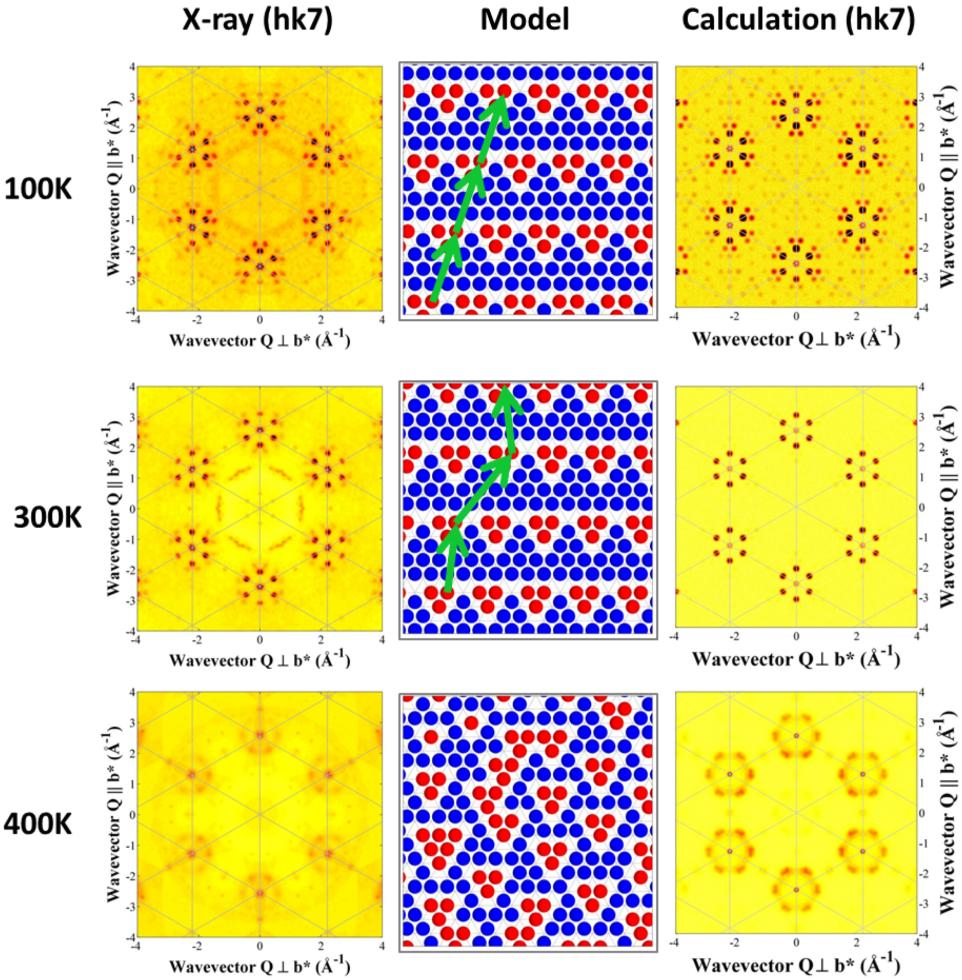

Figure 27: X-ray diffraction data measured using the in-house Xcalibur Diffractometer, at Royal Holloway[138], modelled using Reverse Monte Carlo techniques. Three temperatures are shown corresponding to three phases of $Na_{0.8}CoO_2$. The left hand column displays the X-ray data in the hk7 plane. The central column shows the arrangement of Na ions from RMC refinements that best reproduce the data. The right hand column shows the calculated diffraction pattern.

eter. Using a suitably sized RMC simulation it is possible to recreate the long range ordering seen in diffraction patterns. The size of the cell will need to be large enough to negate finite boundary conditions. RMC has been used to verify the superstructures of Na$_{0.8}$CoO$_2$ [139] and also of Ca substituted Na$_x$CoO$_2$ [140].

In Figure 27, calculations of the different superstructures of Na$_{0.8}$CoO$_2$ which have been primarily calculated by Dan Porter at Royal Holloway[138] are shown. The first column displays X-ray diffraction data in the {hk7} plane at 100K, 300K and 400K corresponding to the stripe phase, disordered stripe phase and disordered phase, respectively. Most notably, with each phase transition, at increasing temperature, the number of Bragg peaks reduces, signifying the loss of long range ordering. The hexagonal lattice corresponds to the simple hexagonal structure inherent in each phase. The Bragg peaks associated with this hexagonal lattice don't disappear. Importantly, at 400K we see the appearance of diffuse rings of intensity in regions between the hexagonal lines where there is no intensity in the lower temperature phases.

The second column shows the results of the RMC simulations to model the respective phases and the third column shows the calculated diffraction patterns that are used for comparison. At 100K a highly ordered phase is observed with coherence between the tri-vacancies in each stripe and between different stripes, as shown by the line of green arrows. As a result the calculated diffraction pattern predicts all of the diffraction peaks seen in the experiment.

In the disordered stripe phase, the ordering of the tri-vacancies between stripes is lost, as shown by the disjointed green arrows. Finally in the with the first columns reading by the RMC simulations show that as the temperature increases the level of ordering decreases. A green arrow in the central column shows how ordering along stripes is preserved while the ordering between stripes is lost. Interestingly, with the loss of coherence between stripes the calculated diffraction pattern loses the additional peaks seen in the stripe phase.

As the crystal enters the disordered phase, the superstructure Bragg peaks disappear and instead broad diffuse rings are observed around the hexagonal Bragg peak locations. In comparison to the disordered stripe phase, the main intensity shifts away from the main hexagonal unit cell lines and into the spaces between. The RMC simulations shows clear clusters of Na1 ions and that these clusters can be in large connected groups. The simulation does not support the regular occurrence of single isolated Na vacancies on the Na2 site.

5 Na_xCoO_2 Computational Modelling

The structural scattering of Na_xCoO_2 provides key insight to allow the setup of simulations of ground state superstructures and dynamics. Reverse Monte Carlo provides further predictions for the correct ground state of $Na_{0.8}CoO_2$. By creating MD simulations based on our understanding of the structure of Na_xCoO_2 and using DFT, via CASTEP, it is possible to observe on a microscopic scale the ionic motions. The theory behind DFT has been explained in Chapter 3, with a particular focus on the CASTEP code.

The stochastic motions can be simulated using MD. Previously, $Na_{0.8}CoO_2$ vibrational motions have been studied by phonon calculations in the square phase system, which showed large rattling modes of certain Na ions [121]. Molecular dynamics calculations are extremely expensive and, therefore, it is necessary to carefully plan the simulations to fully explore the dynamics as efficiently as possible. The disordered stripe and the disordered phases of $Na_{0.8}CoO_2$ are studied extensively with relation to the clustering of ions.

5.1 Introduction

The Na_xCoO_2 system has previously been studied using first principles calculations by Lee et al. [141]. Using the experimental galvanostatic intermittent titration technique, they investigated the diffusion behaviour between Na concentrations of 0 and 2/3 and observed a reversible transition from P2 to O2. The Na diffusion, in the P2 structure, proved to be faster than the Li ion diffusion in the O3 structure. The barriers to diffusion were then calculated via a nudged elastic band method and discovered to be < 200 meV for ions moving between Na1 and Na2 sites.

Mo et al. carried out molecular dynamics and transition-state-search calculations of the Na_xCoO_2 system involving potentials created using DFT code [142]. They studied Na concentrations of $x = 0.56$, 0.69 and 0.75 in the P2 structure. At the x = 0.56 concentration they observed a range of activation energies from 10 meV to 170 meV which were strongly linked to the difference in numbers of neighbours and nearest-neighbours. They conclude that the P2 system outperforms the O3 system due to the low energy barriers associated with the honeycomb sub lattice inherent in the P2 system.

Prior to these investigations, calculations of Na_xCoO_2 have studied the structure and thermal properties of the material. A study by Tada et al. [143], for example, generated interaction potentials from *ab initio* methods which were then used in an MD simulation. The goal of their work was to simulate the atomic vibrations at elevated temperatures. They measured the $Na_{0.5}CoO_2$ system and observed remarkably high mean squared displacements as Na ions hopped.

Transition state searches of the O3-Na_xCoO_2 structure and other transition metal oxides have been compared by Li et al. [144]. In the O3 system, there is only one equivalent Na site, and hops calculated between adjacent sites were found to have activation energies of 0.45, 0.54, 0.46 and 0.67 eV for $NaMO_2$ with M = V, Cr, Co and Ni, respectively. They also calculated the activation energy for Li_xCoO_2 at 0.36 eV suggesting a slight over-estimate given the experimental observation of 0.32 eV [145] which is attributed to the lower c lattice parameter of the almost fully occupied systems. Alternatively, Van der Ven et al. [146] observed that the activation energy is strongly dependent on the local lithium-vacancy configuration. In particular, a divacancy mechanism mediates the diffusion process; if this is present then it would explain the overestimation. Out of the Na-ion systems, Co and V have the lowest activation energies. The low V activation energy is attributed to the large c lattice parameter, perpendicular to the plane. The low activation energies of Na_xCoO_2 and Li_xCoO_2 are suggested to be due to a reduced repulsion from Co ions in comparison to the other transition metals. Another study has carried out first principles calculations of the activation energies of Na_xCoO_2 against $NaNi_{1/3}Co_{1/3}Mn_{1/3}O_2$ and concludes that the Na migration is about 10 times faster in the doped material [147].

Increasingly, first principles calculations are being carried out on prospective battery materials. This is a relatively new development, particularly for Na battery ions. Results have also been published on other crystalline systems such as $Na_{1+x}Zr_2Si_xP_{3-x}O_{12}$ [148], $Na_2M_2TeO_6$ [149], $Na_2Ni_2TeO_6$ [150], Na_3PSe_4 [151], $Na_3Ti_2P_2O_{10}F$ [152] in the past few years. The same techniques are also in use in organic liquid systems [153] demonstrating their flexibility to analyse dynamics in almost all situations.

The research undertaken in this thesis furthers the understanding of Na dynamics in layered transition-metal oxides by applying molecular dynamics techniques to the ordered structures that exist for $Na_{0.8}CoO_2$. These novel calculations are able to expand upon the mechanisms within Na_xCoO_2 that give it good conductivity and make it a promising cathode material.

The optimisation of ionic positions provides a good starting position for MD simulations by limiting the amount of relaxations that occur as the system heads towards equilibrium. Geometry optimisation cells are also necessary to provide the beginning and end points to transition state searches, which are a simple way to calculate the activation energies of hops. In total there were 6 starting set ups; a single stripe phase, a square phase, two sets of enlarged double stripe phase cells with additional vacancies, an isolated vacancy arrangement and a locally ordered arrangement in the disordered phase.

5.2 Simulation Parameters

Prior to running MD calculations it is necessary to optimise the parameters that control the rigour of the simulations. There are several parameters that determine the bonding between ions, including the electronic energy tolerances. To determine the correct values it is necessary to run several series of test single point energy calculations. The value of a parameter is considered to be acceptable when the total energy of the system, and the forces between ions, is converged to within a designated range.

The k-points are also converged by increasing the number of k-points and plotting against the total energy and the forces on each ion as shown in Figure 28. The figure shows the k-point convergence for a stripe phase cell. The total energy is observed to oscillate around a single value with the oscillations decreasing as the number of k-points increases along each reciprocal lattice vector. The force convergence has been plotted as the change in force between the k-point number and the previous k-point number with each circular point marking a different ion. A line has been added at 0.001 eV/Å marking the acceptable convergence criteria. The simulated stripe cell has lattice parameters of 8.55Å, 13.06Å, 10.8Å, 90°, 90° and 109.11°. Convergence happens quickly in all directions given the scale of the lattice parameters. With an energy convergence criteria of 0.0005 eV, the k-points can be set as 322. The force convergence needs a higher number of k-points to be below the blue line, with the values set at 423 points.

It is necessary to displace the finite grid to see the scale of the difference in total energy. Ideally the total energy dependent on the grid will not change if it is moved, but if it does then it would be necessary to reduce the size of the grid. Cells of the square and disordered phases were also created as well as a larger cell made up of two stripe cells. Calculations of the necessary number of k-points found that the distance

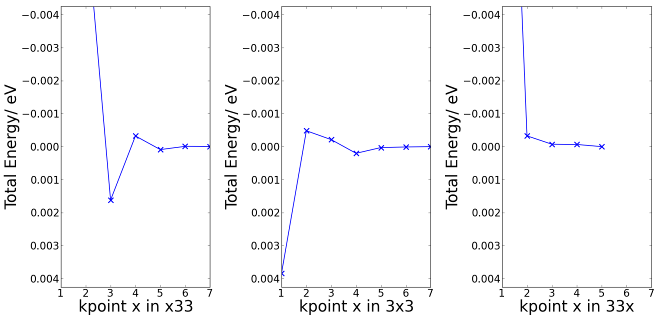

(a) Total energy convergence

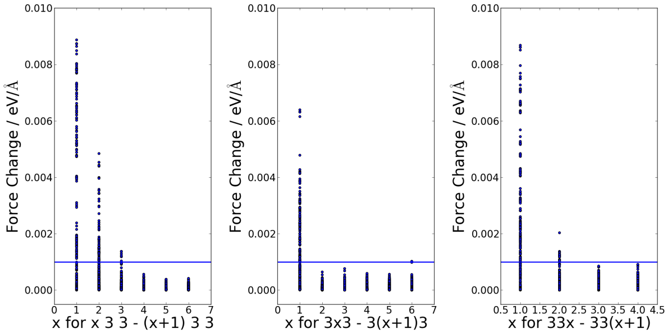

(b) Force convergence

Figure 28: Convergence of the forces and energies dependent on the number of k-points used to model a stripe phase supercell. The notation to describe the number of k-points in a simulation, involves three numbers describing the number of k-points in along each reciprocal lattice vector. A standard system is created with three k-points along each direction, which will have the notation 333. a) Total energy of systems with varying numbers of k-point for each vector in turn, such that if $x = 4$ then $33x = 334$ k-points. b) Change in the force acting on ions. Each graph varies the number of k-points along a different vector in turn. Points shown are the difference in forces on each atom between the x and $x + 1$ k-point, such that if $x = 4$ then the difference in forces between the 334 and 335 k-points sets is calculated. A convergence criterion of 1 meV/Å is shown by the blue line.

between points in reciprocal space was about 0.25 Å^{-1}.

5.3 Stripe Phase

The first cell to be studied was the partially ordered stripe system. The fast dynamics in this region require the use of molecular dynamics simulations to visualise how ions are moving on an ionic level. From structural scattering it is known that the system is still ordered in stripes, however, the coherence between stripes is lost. An MD simulation will enable the natural process by which the stripes lose their coherence with each other to be visualised. To provide the best starting point for MD and transition state search calculations it is necessary to geometry optimise the cell.

Geometry optimisation calculations determine the energetically favourable positions of all ions within a cell. The geometry optimised cells are comparable to the refinements of ion positions from diffraction patterns observed for static systems. Although disordered systems can be optimised, the boundary conditions can lead to a false picture being presented, as it is not possible to simulate fractional occupancies without an extremely large cell containing hundreds or thousands of ions. It is important to look for evidence of self interference across boundaries that may misrepresent the dynamics of the system.

The initial ionic positions of the stripe phase supercell are shown in Figure 29. The two parts show the top and bottom Na layers of the system with the positions of the Co and O ions shown beneath. Ideally the Na1 ions will sit between the Co ions while the Na2 ions are in a gap with no immediate neighbour's perpendicular to the plane. After the geometry optimisation, slight distortions can be seen for the Na ions close to the tri-vacancy clusters. These distortions are in the plane towards regions empty of ions, for example the Na2 ion at the point between tri-vacancy clusters.

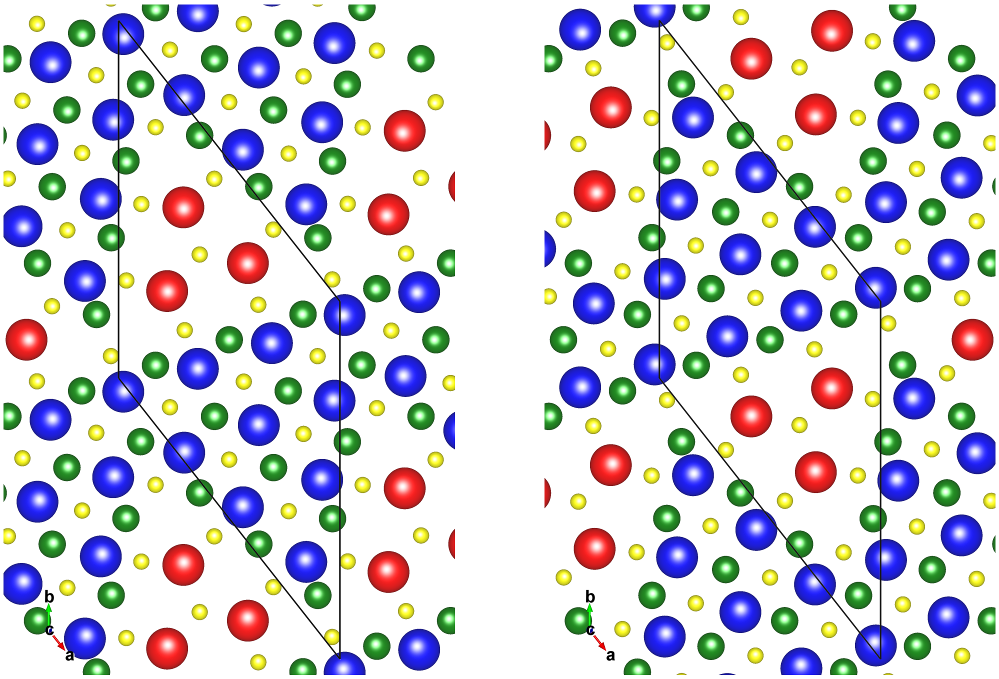

(a) Lower Na layer (b) Upper Na Layer

Figure 29: Geometry Optimised stripe phase supercell of $Na_{0.8}CoO_2$. Initial ionic positions of a) the bottom Na layer and b) the top Na layer. Ions are plotted with Oxygen ions as yellow, Cobalt ions as green and the Na ions as red or blue dependent on whether they are on the Na1 or Na2 site, respectively. The cell boundaries are shown by the black line.

5.3.1 Molecular Dynamics

An MD simulation of a single stripe phase cell, shown in Figure 29, was carried out at 350 K for 12 ps with a time step of 5 fs. The cell has dimensions of 8.55Å, 13.06Å, 10.8Å, 90^o, 90^o and 109.11^o and consisted of 24 Na ions split over 2 layers, and then 60 O ions and 30 Co ions. The temperature was chosen as 350 K as this is within the disordered stripe phase experimental temperature range without being too close to either of the boundaries. The calculation was carried out in the NVT canonical ensemble, therefore the volume of the cell is constricted throughout the simulation.

The fastest vibrations in the $Na_{0.8}CoO_2$ stripe phase system, from phonon calculations [154], have an energy of $\sim$ 80 meV which corresponds to an oscillation time period of $\sim$ 50 fs. It is standard practice to choose a time step approximately 8 to 10 times smaller than the period of the fastest oscillation. Several time steps were tested to determine the optimum ratio of simulated time/ calculation time. As expected lower time steps completed each step faster, but the need to calculate more steps increased the time of the overall calculation. A time step of 5 fs was selected as being the most efficient use of computational resources. The total time of the simulation was constricted by budget, therefore it was decided that a 10 ps simulations with an initial 2 ps equilibrating time were acceptable.

Figure 30 provides a representation of the dynamics of the Na ions in the lower layer of the simulation. The initial ionic positions and a trace map of the Na ion trajectories integrated over the total simulation time are shown in Figure 30a. The Na ions can clearly be divided into two groups: a band of dynamic hopping ions close to and within the tri-vacancy clusters, and a band of largely static ions that away from the clusters that act to separate the stripes.

Figure 30b shows the root-mean-squared (RMS) displacements, within the plane, of Na ions from their original positions. This graph emphasises that major displacements only occur for a few ions. Large displacements are also quantised, meaning that these must be due to hops between different stable ionic sites. The magnitude of the hop distance is comparable to the separation between adjacent Na1 and Na2 sites (1.65 Å). However, distortions in the vicinity of tri-vacancy clusters mean that there is unlikely to be exact correspondence. Figure 30d shows the component of the ionic displacement parallel to the stripe. Apart from thermal vibration, no net movement is seen in this direction.

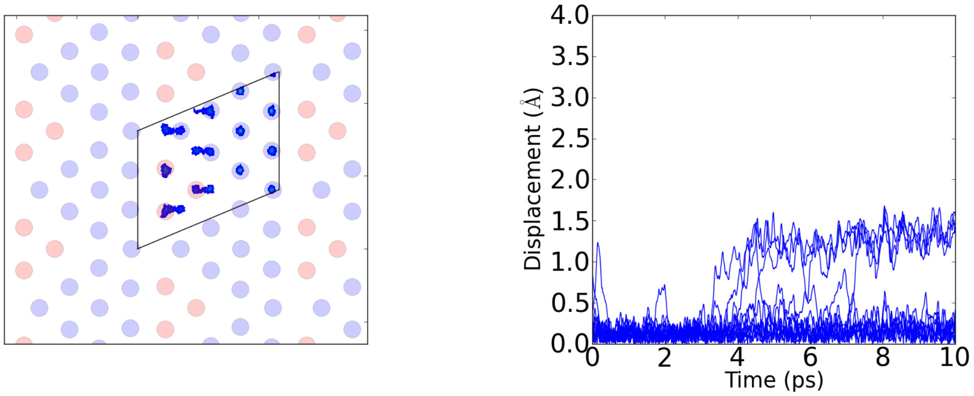

(a) Na Ion trajectories (b) RMS displacement of Na ions

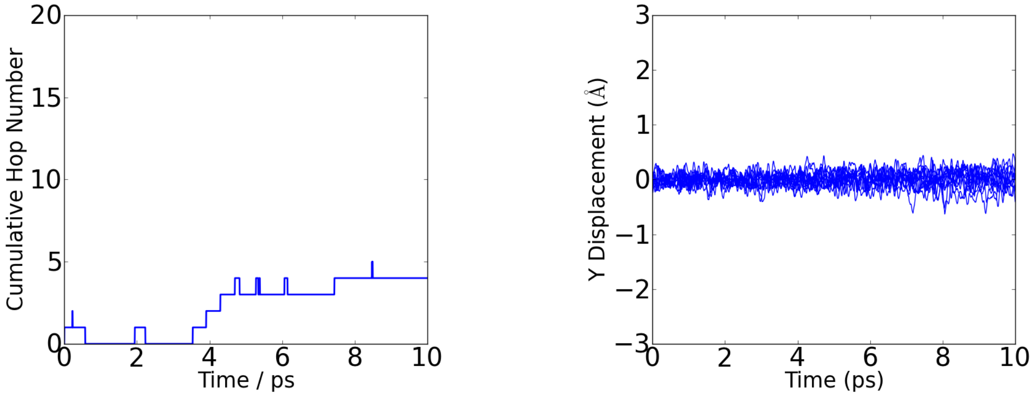

(c) Cumulative Na-ion hops (d) Displacement parallel to the stripe

Figure 30: The lower Na layer of a MD simulation of the stripe phase superstructure cell at T = 350K. a) is a trace of the Na positions integrated over the total time with the initial Na ion positions plotted as large circles. The simulation cell boundaries are shown as black lines. b) shows the root-mean squared displacement of ions from their original position with time. c) shows the cumulative number of transitions between sites for Na ions. d) shows the displacement of ions parallel to the stripe.

The cumulative number of hops experienced by all Na ions over the total simulation time is displayed in Figure 30c. In total four hops are observed in the system, although on inspection five can be seen in Figure 30a. Hops are identified dependent upon their position in relation to the original placements of the O and Co ions. A two dimensional map is created wherein each Na ion is recorded as being closest to the in-plane position of a O ion in the alternate layer of the P2 structure (if its in a Na2 position), or being closest to a Co ion position (if its in a Na1 position). At each step of the simulation, Na ions are re-evaluated to determine whether they are closest to a Co or alternate layer O ion and, therefore, whether they have undergone a hop. To prevent over counting of hops, a time factor is introduced which states the condition that if the ion returns to its original site within 0.5 ps then a hop has not occurred. In the graph this can be seen by increases in cumulative hop that are subtracted a short time later.

Figure 31 shows the top layer of the same stripe cell simulation. The same bands of 'static' and 'dynamic' ions can be observed in this layer. In contrast to the lower layer where all movements were perpendicular to the stripe, in this layer one ion is observed to move along the stripe. In the displacement graphs the ion is coloured green. The ion hops at around 5 ps, however a short time later at 6 ps it moves back to its original position.

5.4 Square Phase

The square phase was selected as an interesting candidate to compare with the stripe phase. The identical concentration and presence of tri-vacancy clusters could provide similar dynamic behaviour. The crucial difference between the two systems is the proximity of tri-vacancy clusters to each other. In the square phase clusters are separated by rows of Na2 ions in all directions. Studying the relative levels of diffusional

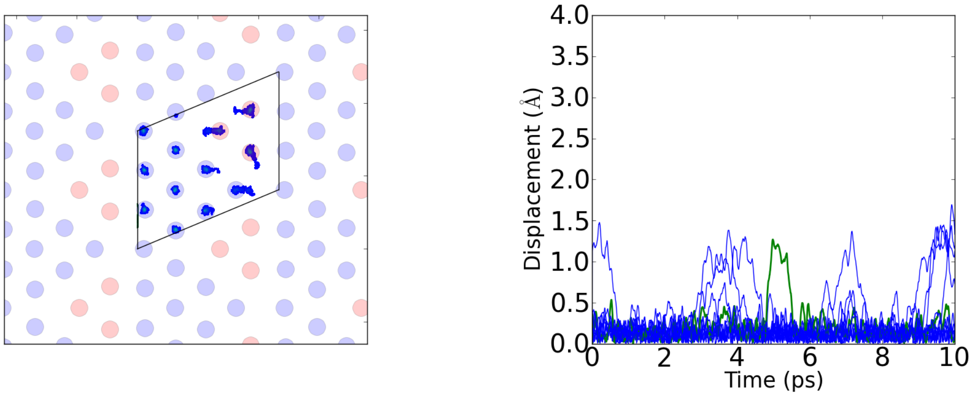

(a) Na ion trajectories

(b) RMS Displacement of ions

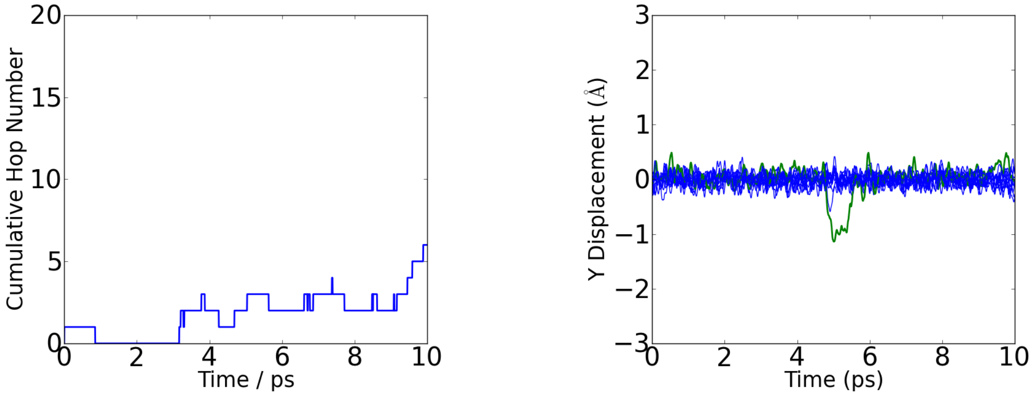

(c) Cumulative Na Hops.

(d) Displacement parallel to the stripe.

Figure 31: The upper Na layer of a Molecular Dynamics simulation of the stripe phase superstructure cell at T = 350K. a) is a trace of the Na positions integrated over the total time with the initial Na ion positions plotted as large circles. The simulation cell boundaries are shown as black lines. b) shows the root-mean squared displacement of ions from their original position with time. c) shows the cumulative number of transitions between sites for Na ions. d) shows the displacement parallel to the stripe.

events in each system will determine the effect of interconnected clusters.

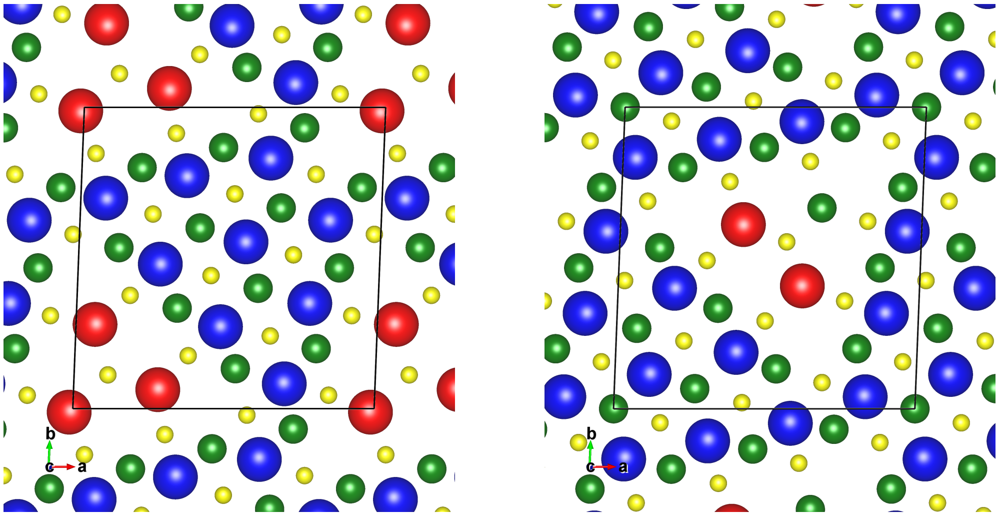

(a) Lower Na layer (b) Upper Na layer

Figure 32: Geometry Optimised square phase supercell of $Na_{0.8}CoO_2$. Initial ionic positions of a) the bottom layer of the ideal square superstructure and b) the top layer with a vacancy on one of the Na1 sites. Ions are plotted with Oxygen ions as yellow, Cobalt ions as green and the Na ions as red or blue dependent on whether they are on the Na1 or Na2 site, respectively. The cell boundaries are shown by the black line.

The ionic positions of the square phase supercell are shown in Figure 32. The bottom layer is the standard arrangement with a tri-vacancy cluster separated from neighbouring clusters by rows of Na2 ions. Slight in plane distortions are also observed in this system with the Na2 ions distorted towards the cluster. The Na1 ions are distorted away from their Na1 neighbours. The top layer of the square phase has had an ion removed from the tri-vacancy cluster in preparation for an MD simulation. Very weak binding between Na layers means that the two levels can be considered pseudo-independent simulations.

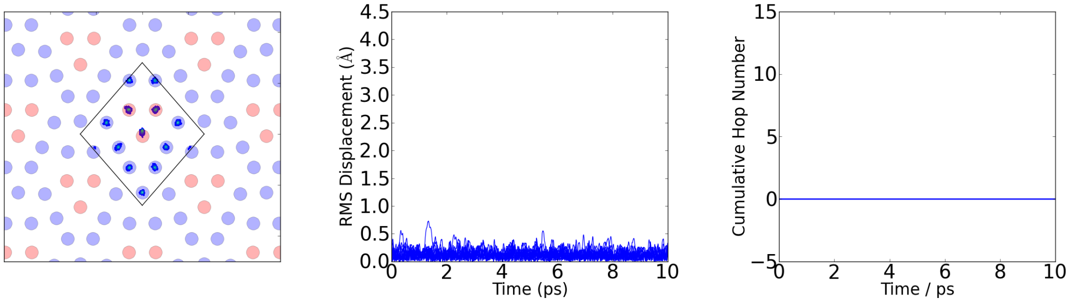

(a) Na ion trajectories (b) RMS displacement (c) Cumulative Na-ion hops

Figure 33: The lower Na layer of a MD simulation of an ideal square phase superstructure cell at T = 350 K. a) The trace of the Na ion positions integrated over the total time, with the initial Na ion positions plotted as large circles. The simulation cell boundaries are shown as black lines. b) The RMS displacement of Na ions from their original position with time. c) The cumulative number of transitions between sites for Na ions.

5.4.1 Molecular Dynamics

The Molecular Dynamics simulation for the square phase cell ran for a total of 10 ps plus 2 ps equilibration time. The cell has lattice parameters of 10.2758 Å, 10.2758 Å, 10.8 Å, 90°, 90°, 87.7958° and contains 60 O ions, 30 Co ions and 23 Na ions due to the additional vacancy in the top layer. A time step of 5 fs was used, consistent with the stripe phase MD calculation. Voneshen et al. [121] calculates that the shortest phonon period is 50 fs for the square phase, and has confirmed that the period is similar in the stripe phase [154]. Even though this structure is only stable up to T $\sim$ 280K, the temperature was set at T = 350 K for direct comparison with the MD simulation of the stripe phase.

Figure 33 is of the lower layer of the MD simulations of the ideal square phase. This layer is fully occupied and consists of one tri-vacancy cluster and a large cluster of Na2 ions which encloses the tri-vacancy cluster. The cell boundaries are translated relative to Figure 32a. The ion trajectories in Figure 33a show very little movement away from the original positions. In fact, looking at Figure 33b, only 3 RMS displacements exceed 0.5 Å, and none of these are for long periods of time. At no point does any ion move closer to a different neighbouring ion. Hence the cumulative hops in Figure 33c are zero throughout.

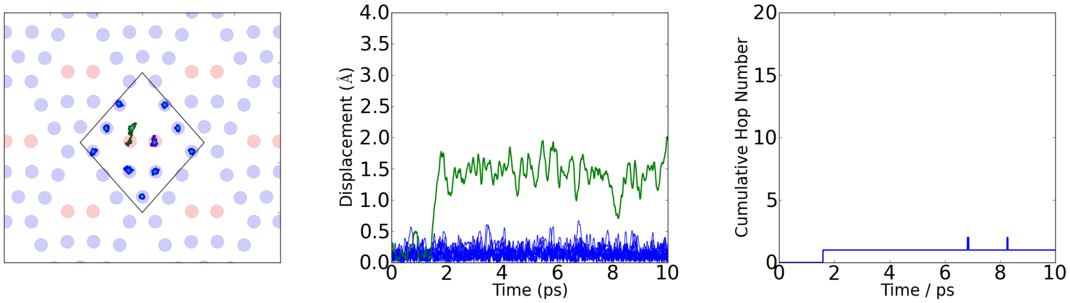

(a) Na ion trajectories (b) RMS displacement (c) Cumulative Na ion hops

Figure 34: The upper Na layer of a Molecular Dynamics simulation of a square phase superstructure cell with one Na1 ion removed at T = 350 K. a) The trace of the Na ion positions integrated over the total time, with the initial Na ion positions plotted as large circles. The simulation cell boundaries are shown as black lines. b) The RMS displacement of Na ions from their original position with time. c) The cumulative number of transitions between sites for Na ions.

The top Na layer of the simulation is shown in Figure 34. In this layer an additional vacancy has been added by removing one Na1 ion of the tri-vacancy cluster. Figure 34a shows the initial positions and the trajectories of the Na ions. One ion, coloured green, makes a hop after 1.5ps from a Na1 site to a Na2 site. After this hop the ion remains in its new site, however with some thermal vibrations as shown in Figure 34b. This contributes the one hop seen in Figure 34c. No other ion is observed to displace far from its original site.

5.5 Extended Stripe Cell

Two large cells were created to model the stripe phase with additional vacancies. This allowed longer range hops and also ensured that there were no coherent effects between tri-vacancy clusters. The lattice parameters of these cells are 17.1 Å, 13.06 Å, 10.8 Å, 90^o, 90^o, 109.1071^o. Figure 35a and 35b show the bottom and top layers of the first cell, respectively. An additional vacancy is placed in each cell to examine the effect of additional disorder on diffusion. In the bottom layer the vacancy was actually placed in one tri-vacancy cluster to allow the transfer of an ion from one cluster to the next in a transition state search or an MD simulation. The vacancy in the top layer was placed in the, typically stationary, Na2 ions near to a cluster.

Figures 35c and 35d are a second set of stripe cells with additional vacancies. In the bottom layer an additional vacancy has been placed in the other possible distinct position of a tri-vacancy cluster. This is in preparation for a MD simulation to determine the dependence of diffusion on where the vacancy begins. In the top layer a vacancy has been placed in amongst the Na2 ions as far away as possible from the tri-vacancy clusters.

5.5.1 Molecular Dynamics

The extended stripe cells contain 226 ions each with 23 Na ions in each layer of each simulation. This leads to a far more expensive calculation at each step and this was why the series of MD simulations were limited to 10 ps of time. The temperature was kept at 350 K as this is a simulation of dynamics in the disordered stripe phase. An additional vacancy was added to non-equivalent positions in each level as described in

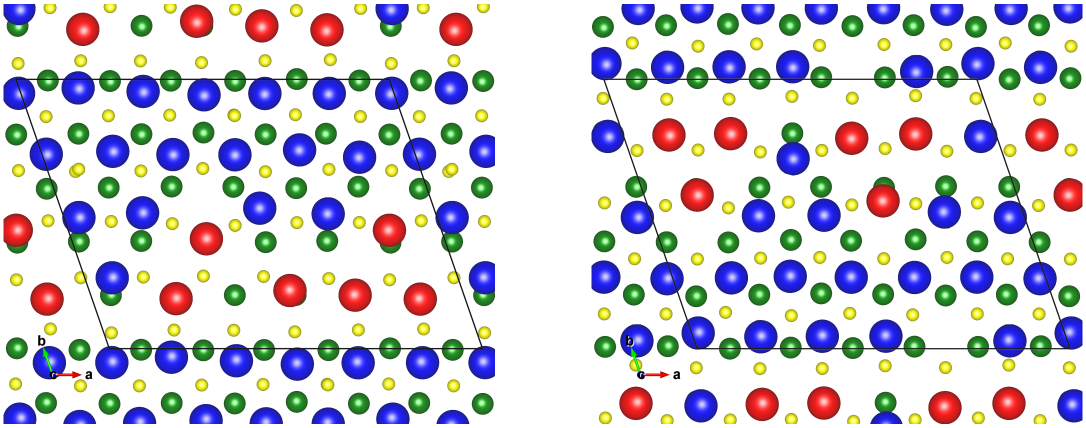

(a) Lower layer of the first cell (b) Upper layer of the first cell

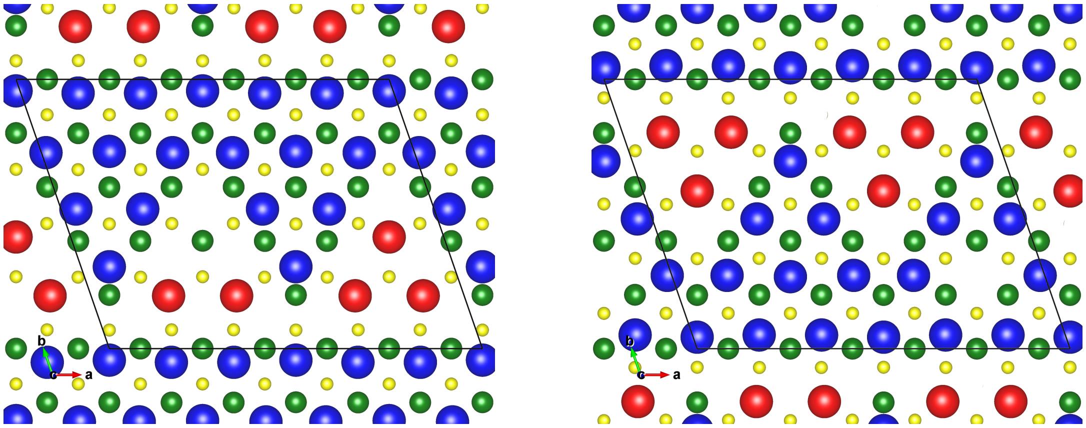

(c) Lower layer of the second cell (d) Upper layer of the second cell

Figure 35: Two stripe superstructures cells, each with additional vacancies. The ionic positions are shown according to colour. The Oxygen ions are yellow, the Cobalt ions are green and the Na ions are red or blue dependent on whether they are on the Na1 or Na2 site, respectively. The cell boundaries are shown by the black line. For the first cell a) one of the Na1 ions is removed and b) a Na2 ion next to the stripe is removed. For the second cell c) a different Na1 ion is removed and d) a Na2 ion away from the stripe is removed.

the previous section.

Figure 36 is a layer containing an additional vacancy within one of the two tri-

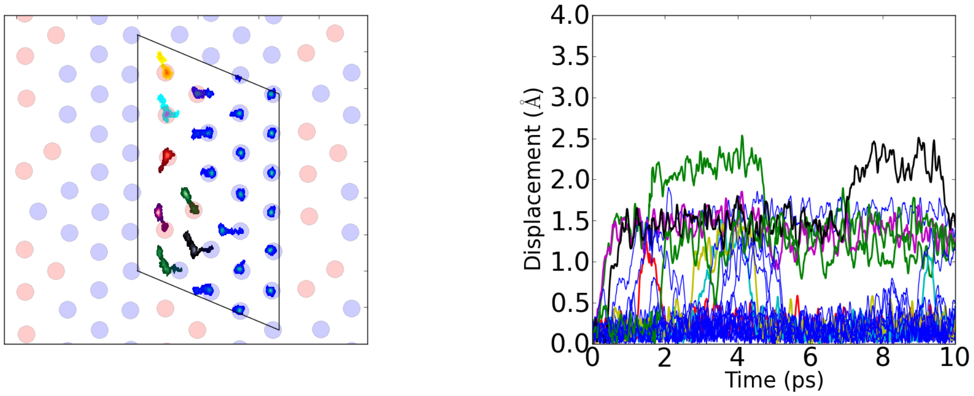

(a) Na ion trajectories

(b) RMS displacement of Na ions

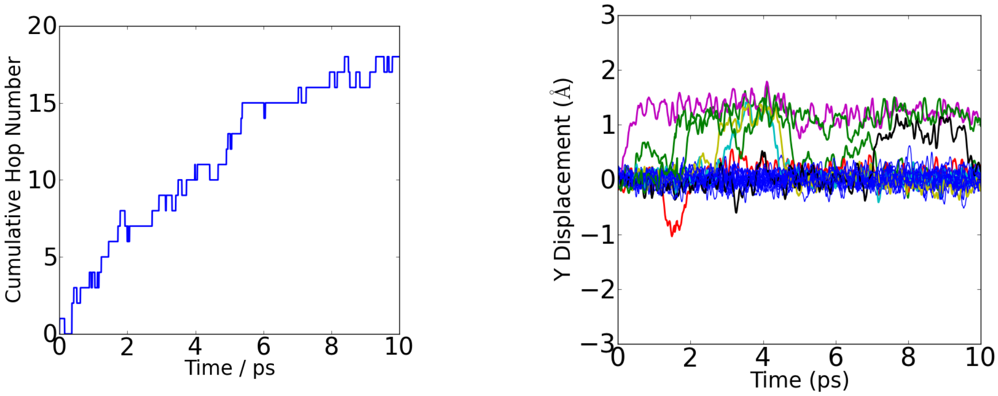

(c) Cumulative Na-ion hops

(d) Displacement parallel to the stripe

Figure 36: The MD simulation for the stripe cell with an additional Na1 vacancy, as shown in Figure 35a, at T = 350 K. a) The trace of the Na ion positions integrated over the total time, with the initial Na ion positions plotted as large circles. The simulation cell boundaries are shown as black lines. b) The RMS displacement of Na ions from their original position with time. c) The cumulative number of transitions between sites for Na ions. d) The component of the displacement of ions parallel to the stripe.

vacancy clusters, as shown in Figure 35a. The trace of ionic trajectories in, Figure 36a, shows a large number of short Na1-Na2 hops, with the motion of each ion colour coded. Initially the closest ions move towards the vacancy and then subsequent waves of movement follow. The movements include Na1 ions and Na2 ions adjacent to the stripe.

The RMS displacements, in Figure 36b, show that most ions move in short hops away from their initial site. In two cases ions have multiple hops, in these cases making transitions from Na2-Na1-Na2. The transitions are not continuous and instead the ions do remain on the Na1 sites for a short amount of time. After a short while on the new Na2 site they do move back to the Na1 site.

Studying Figure 36d, of displacement along the stripe, all ion hops are in one direction except for one short red ion's movement which is quickly reversed. This means a total of 6 ions have taken a coherent series of motions in the same direction along the stripe. Alternatively this could be viewed as a vacancy moving along the stripe in the opposite direction. Throughout the simulation a consistent increase of cumulative hops is observed, Figure 36c, although it does appear that the hop rate is slowly decreasing.

In the initial configuration corresponding to Figure 35b, a vacancy was inserted into the band of Na2 ions next to the stripe. The fact that the vacancy was placed close to the tri-vacancy stripe may be expected to increase the potential for diffusion of ions along the stripe. Figure 37a shows the trace of the ion trajectories with the initial ionic positions. The red and light blue coloured ions are observed to move towards the vacancy along the available Na2-Na1 pathways. Similarly their neighbouring ions, magenta and green, follow them moving parallel along the stripe towards the initial site of the additional vacancy.

The RMS displacements in Figure 37b, show a large number of short hops of several ions starting near the beginning of the simulation. Combining this with the displace-

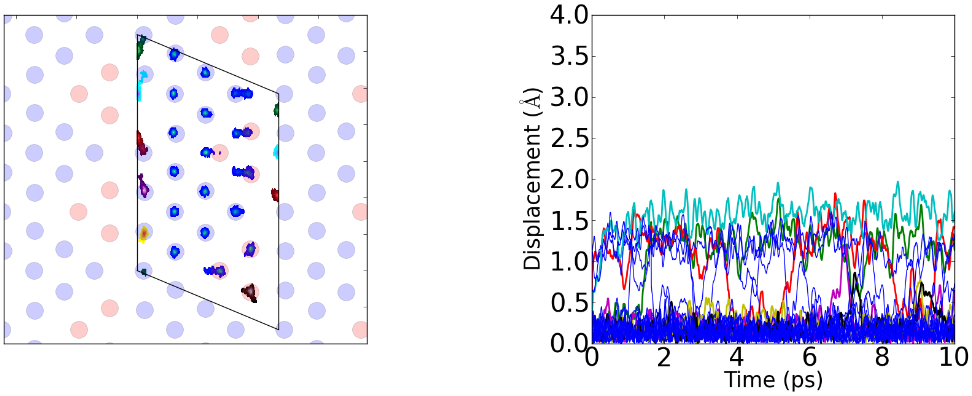

(a) Na ion trajectories

(b) RMS displacement of Na ions

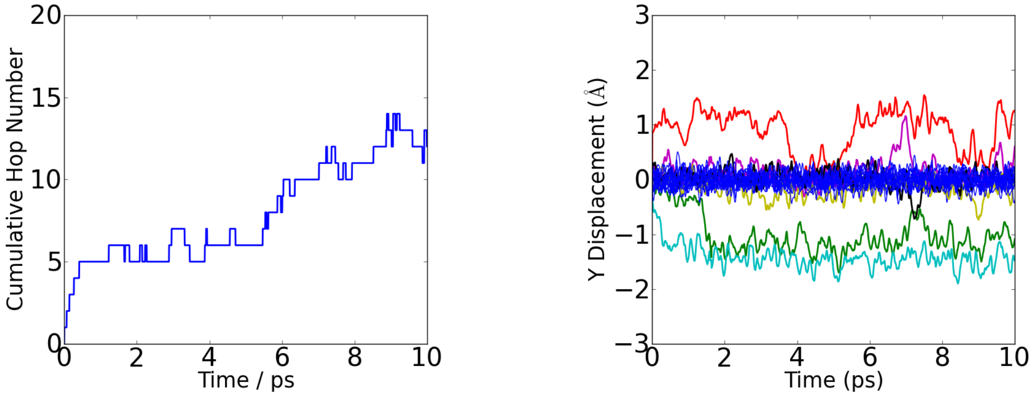

(c) Cumulative Na-ion hops

(d) Displacement parallel to the stripe

Figure 37: The MD simulation for the stripe cell with an additional Na2 vacancy next to the stripe, as shown in Figure 35b, at T = 350 K. a) The trace of the Na ion positions integrated over the total time, with the initial Na ion positions plotted as large circles. The simulation cell boundaries are shown as black lines. b) The RMS displacement of Na ions from their original position with time. c) The cumulative number of transitions between sites for Na ions. d) The component of the displacement of ions parallel to the stripe.

ment along the stripe in Figure 37d, it appears that the majority of the hops are perpendicular to the stripe. A total of five ions move towards the site of the additional vacancy within the first picosecond. Of these only the two coloured red and light blue move parallel to the stripe. After a short time, 1.5 ps, the green ion follows. Its positioning completes a quadri-vacancy structure involving six ions on Na1 sites. A magenta ion does follow at $\sim$ 7 ps but it returns to its original site quickly.

Figure 37c displays the cumulative hops. Initially in response to the additional vacancy, a series of five motions occur within 1 ps. The structure then assumes a relative stability before a second series of hops at around 6 ps. This corresponds to the movements of the pink ion and also a move by the green ion. Ions in the tri-vacancy clusters also move in response.

In the initial configuration corresponding to Figure 35c a different Na1 ion was removed so that a vacancy has been added in one of the tri-vacancy clusters at the vertex of the triangle, perpendicular to the stripe. The initial positions and the Na ion trajectories integrated over the simulation time are shown in Figure 38a and interconnected diffusion pathways are observed for multiple ions.

The RMS displacements in Figure 38b, show that many multiple ions move away from their original sites. Three ions, coloured magenta, red and yellow, move a particularly large distance. The magenta ion moves first and settles in a site around 3 Å from its original position. This corresponds to a hop of a Na1 ion onto a neighbouring Na2 site, then a further hop to a different vacant Na1 site (The Na1-Na1 distance is 2.85 Å). Again, distortions in the vicinity of disorder means that there is unlikely to be exact correspondence.

The displacement parallel to the stripe, Figure 38d, shows clearly that after the magenta ion moves, the yellow ion follows shortly, after 1 ps. At regular intervals of 2 ps, a red and then a light blue coloured ions then follow. The trace of ion trajectories

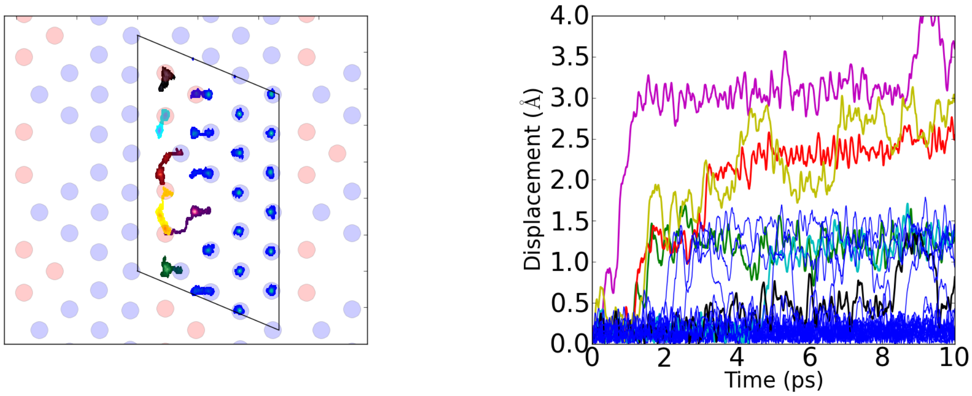

(a) Na ion trajectories

(b) RMS displacement of Na ions

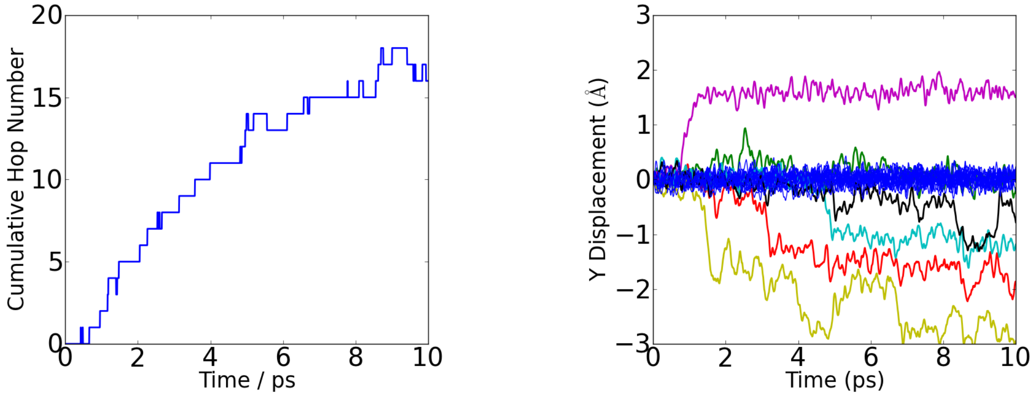

(c) Cumulative Na-ion hops

(d) Displacement parallel to the stripe

Figure 38: The MD simulation for the stripe cell with an additional Na1 vacancy, as shown in Figure 35c, at T = 350K. a) The trace of the Na ion positions integrated over the total time, with the initial Na ion positions plotted as large circles. The simulation cell boundaries are shown as black lines. b) The RMS displacement of Na ions from their original position with time. c) The cumulative number of transitions between sites for Na ions. d) The component of the displacement of ions parallel to the stripe.

shows that the magenta ion hops to the site of the additional vacancy. This moves the vacancy within the stripe and the other Na1 ion in this tri-vacancy cluster, yellow, then moves towards it. Shortly after making a Na1-Na2 hop, the red ion makes a Na2-Na1 hop to the initial site of the yellow ion. There is a series of correlated hops: magenta, yellow, red, light blue and black, which are all directed towards the original vacancy resulting in a large net movement of ions, as each individual ion moves towards a neighbouring vacant region.

Overall this can be interpreted as the added vacancy moving within the stripe and then moving along the stripe with each subsequent ions hop. The graph of cumulative hops, Figure 38c, increases in a consistent way up until 7 ps at which point the rate of increase slows.

Finally, for the initial position with a Na2 vacancy furthest from the tri-vacancy clusters, Figure 35d, the MD simulation is presented in Figure 39. The additional vacancy is inserted on a Na2 site symmetrically between 2 clusters on the stripe. It is separated by a row of Na2 ions from the clusters in all directions. The RMS displacement in Figure 39b shows relatively low levels of diffusion on all ions. Small movements are associated with ions within the stripe vacancy clusters and there are no significant displacements parallel to the stripes, Figure 39d. The level of dynamic behaviour is much less that when vacancies are introduced in the vicinity of stripes, and instead resembles the ideal stripe superstructure.

5.6 Isolated Vacancies in the Disordered Phase

The disordered phase was modelled by creating a super cell of $5x5x1$ basic hexagonal unit cells of $Na_{0.8}CoO_2$ giving a total of 200 ions with 100 O ions, 50 Co ions and 50 Na ions in the fully occupied cell. The total cell had lattice parameters of 14.2855 Å,

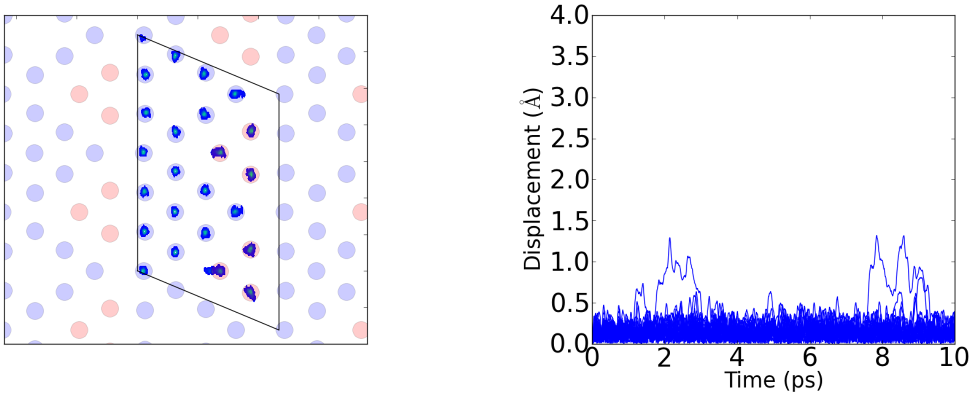

(a) Na ion trajectories (b) RMS displacement of ions

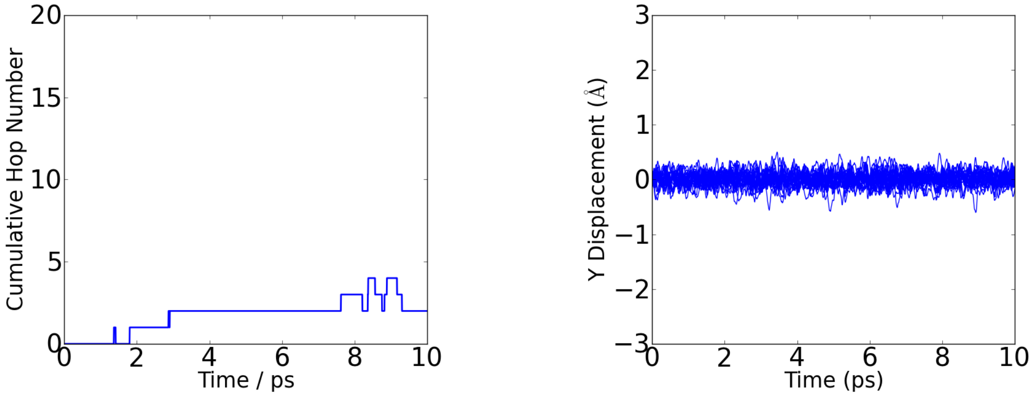

(c) Cumulative Na-ion hops (d) Displacement parallel to the stripe

Figure 39: The MD simulation for the stripe cell with an additional Na2 vacancy away from the stripes, as shown in Figure 35d, at T = 350 K. a) The trace of the Na ion positions integrated over the total time, with the initial Na ion positions plotted as large circles. The simulation cell boundaries are shown as black lines. b) The RMS displacement of Na ions from their original position with time. c) The cumulative number of transitions between sites for Na ions. d) The component of the displacement of ions parallel to the stripe.

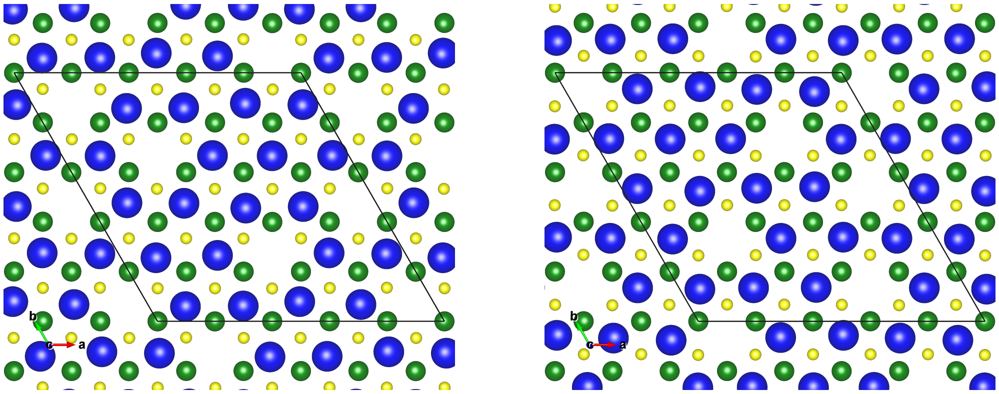

(a) Lower Na layer

(b) Upper Na layer

Figure 40: Disordered phase cell made up of $5x5x1$ basic hexagonal cells with vacancies isolated from each other. Ions are plotted with Oxygen ions as yellow, Cobalt ions as green and the Na ions as red or blue dependent on whether they are on the Na1 or Na2 site, respectively. The cell boundaries are shown by the black line. The initial positions are shown for a) the lower layer and b) the upper layer.

14.2855 Å, 10.8 Å, 90°, 90°, 120°. In each Na layer there are a total of 25 Na2 sites, all of which were fully occupied when the cell was geometry optimised. Firstly five Na2 ions were removed from each layer. The placement of the vacancies created a system of isolated vacancies, all separated by at least one other Na2 ion. The arrangement of both the top and bottom Na layers are shown in Figure 40.

5.6.1 Molecular Dynamics

A MD simulation of the disordered phase at 80% concentration was set up with the vacancies arranged to be isolated from each other. In the starting set up, all Na1 positions are blocked by neighbouring Na2 ions. Any hops observed must therefore be Na2-Na2 hops. The exception to this is if vacancies become neighbours, which will unblock Na1 sites. The MD simulation ran at a simulated temperature of 550 K for

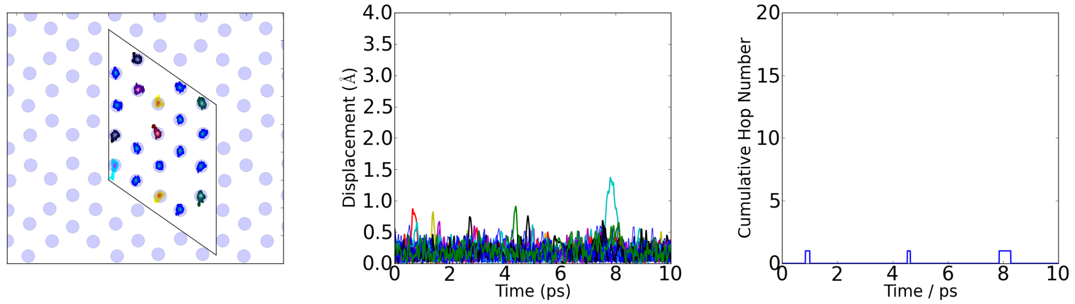

(a) Na ion trajectories (b) RMS displacement (c) Cumulative Na hops

Figure 41: The lower Na layer of a Molecular Dynamics simulation of a disordered system with isolated vacancies, as shown in Figure 40a, at T = 550 K. a) The trace of Na ion positions integrated over the total time, with the initial Na ion positions plotted as large circles. The simulation cell boundaries are shown as black lines. b) The RMS displacement of Na ions from their original position with time. c) The cumulative number of transitions between sites for Na ions.

10 ps after an initial 2 ps equilibration time.

Figure 41a shows the Na ion trajectories of the lower layer, Figure 40a, with the initial Na positions underlayed as blue circles. All ions appear to stay close to their initial locations. Only one ion in Figure 41b, coloured light blue, appears to make any significant motion away from its original site. At a maximum displacement of 1.45 Å, the motion is almost enough to get the ion to a neighbouring Na1 site. However, this site is blocked and the ion returns to its original location. Figure 41c, the cumulative hops graph shows zero due to the lack of any ions hopping.

The simulated behaviour of the top layer of Na ions, Figure 40b, is shown in Figure 42. A single clear Na2-Na2 hop is observed. The ion is coloured yellow and takes a curved path to get between the start and end points of the hop, Figure 42a. The path is curved due to the O ions which repulse the Na ion from the shortest path. Figure

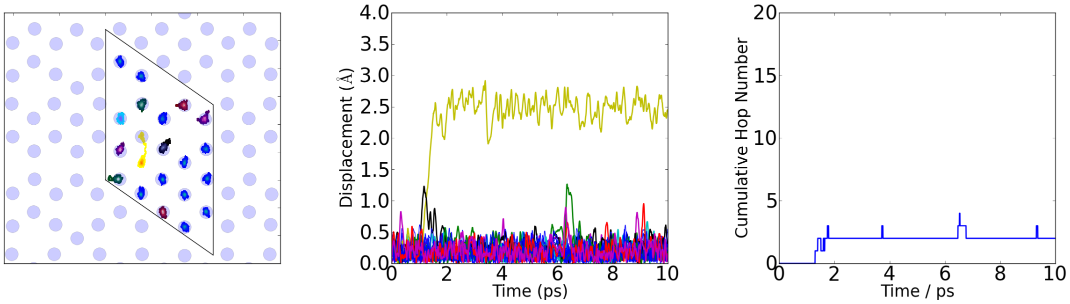

(a) Na ion trajectories (b) RMS displacement (c) Cumulative Na hops

Figure 42: The upper Na layer of a Molecular Dynamics simulation of a disordered system with isolated vacancies. a) is a map of the Na ionic density integrated over the total time with the initial Na ion positions plotted as large circles. The simulation cell boundaries are shown as black lines. b) shows the root-mean squared displacement of ions from their original position with time. c) shows the cumulative number of transitions between sites for Na ions.

42b shows the RMS displacement of the ions from their original positions. The yellow ion is observed to take a rapid continuous motion between sites. This coincides with a temporary displacement of a neighbouring black ion. The Na trajectories, Figure 42a, show that the black ion moves in a direction perpendicular to the hop direction. Presumably this ion moving out of the way, lowers the barrier for the Na2-Na2 ion hop. Figure 42c, the cumulative hop graph, double counts the hop as the yellow ion passed very close to a Na1 site on its curved path before heading to its final site.

5.7 Local Ordering in the Disordered Phase

A second simulation was performed for the disordered phase based on the same 5×5×1 supercell. Five Na ions were again removed from each layer. However, the remaining ions were rearranged with some being promoted from Na2 to Na1 sites to create local ordering. The lower layer consists of a tri-vacancy and a di-vacancy cluster that are separated by Na2 ions, shown in Figure 43a. The upper layer consists of a tri-vacancy cluster with an additional vacancy close by, and another vacancy isolated, shown in Figure 43b.

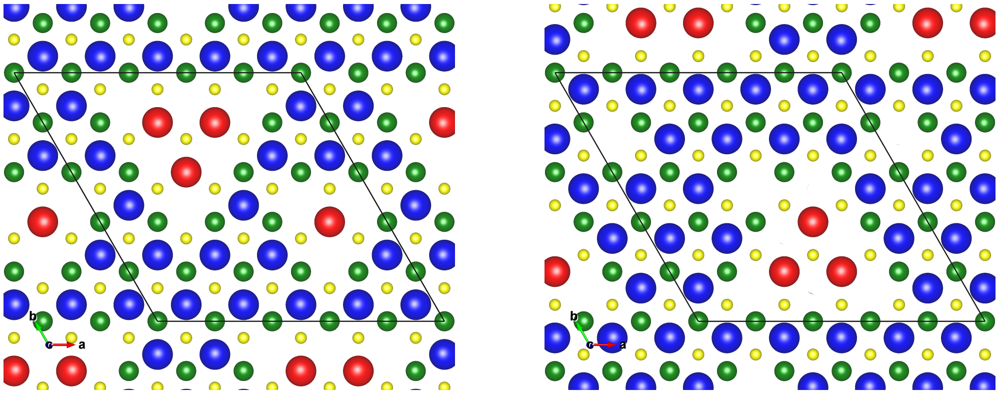

(a) Lower Na Layer (b) Upper Na Layer

Figure 43: Disordered phase cell made up of 5×5×1 basic hexagonal cells with ions arranged to include di-vacancy and tri-vacancy clusters. Ions are plotted with Oxygen ions as yellow, Cobalt ions as green and the Na ions as red or blue dependent on whether they are on the Na1 or Na2 site, respectively. The cell boundaries are shown by the black line. The positions are shown for a) the lower and b) the upper Na layers.

5.7.1 Molecular Dynamics

The second disordered phase MD simulation ran at 550 K for 10 ps with an initial 2 ps equilibration time. The aim of this simulation was to investigate the effect of the presence of multi-vacancy clusters on diffusion. In the lower layer of the simulation, Figure 43a, a tri-vacancy cluster and a di-vacancy cluster have been created. The only initial hops available are those of Na1 ions out of the clusters and onto Na2 sites. Any chained diffusion motions will then require a second ion from somewhere else to move in response. This may be another Na1-Na2 hop or a Na2-Na1 hop.

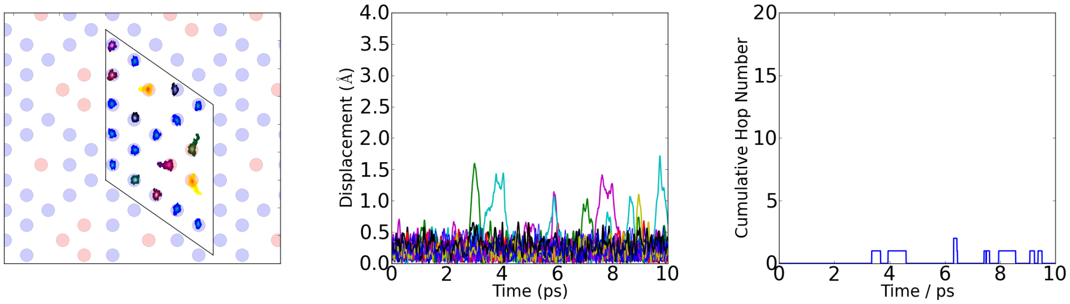

(a) Na ion trajectories (b) RMS displacement (c) Cumulative Na hops

Figure 44: The lower Na layer of a MD simulation of a disordered system with local ordering of vacancies, shown in Figure 43a, at T = 550 K. a) The trace of the Na ion positions integrated over the total time, with the initial Na ion positions plotted as large circles. The simulation cell boundaries are shown as black lines. b) The RMS displacement of Na ions from their original position with time. c) The cumulative number of transitions between sites for Na ions.

In Figure 44a the trace of Na ion positions shows large variations from the clusters towards the surrounding Na2 sites. In particular in the case of the tri-vacancy, the ions are only able to move away. The RMS displacements of the Na ions from their original sites are shown in Figure 44b. The four Na1 ions associated with the clusters are observed to move large distances of around 1.4 Å although none remain in place for longer than 0.5 ps. No Na2 ions are observed to make large displacements at all. This leads to zero hops being recorded in the cumulative hop graph, Figure 44c.

Figure 45 shows the graphs detailing the behaviour of Na in the top layer of the simulation, Figure 43b. Figure 45a shows the ion trajectories with the ions' initial positions underlayed as pale circles. The initial setup involved a tri-vacancy cluster

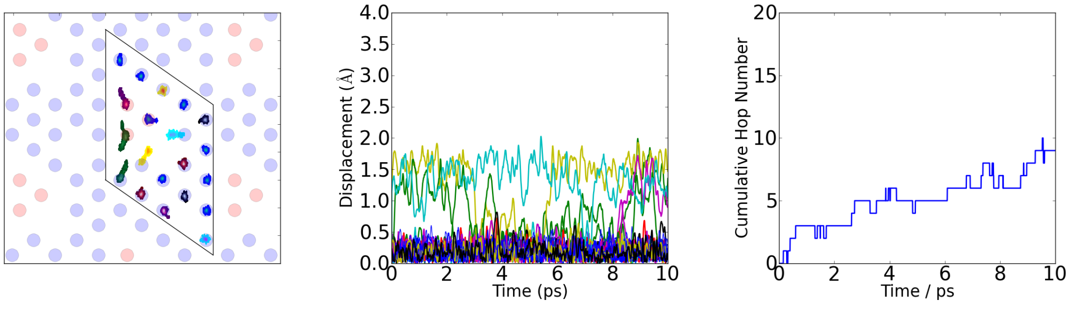

(a) Na ion trajectories (b) RMS displacement (c) Cumulative Na hops

Figure 45: The upper Na layer of a MD simulation of a disordered system with local ordering of vacancies, shown in Figure 43b, at T = 550 K. a) The trace of the Na ion positions integrated over the total time, with the initial Na ion positions plotted as large circles. The simulation cell boundaries are shown as black lines. b) The RMS displacement of Na ions from their original position with time. c) The cumulative number of transitions between sites for Na ions.

surrounded by Na2 ions except for one site which was vacant. Another vacancy was placed further away separated by Na2 ions. The ion trajectories shows large movements of all the ions near to the cluster. Additionally, one ion near to the isolated vacancy is observed to have a large displacement towards the vacancy. The movement of ions in the cluster echoes that of the earlier simulations with all the displacements being away from the centre of the tri-vacancy cluster. The Na2 ions surrounding the vacancy adjacent to the cluster are observed to move towards the vacancy to Na1 sites. Their neighbours are seen to move too, typically towards their initial positions.

Figure 45b shows the RMS displacements of the ions. The yellow and light blue ions neighbouring the adjacent Na2 vacancy are seen to move immediately. Similarly the green ion of the tri-vacancy cluster is observed to move almost immediately. This then moves back to its original position before moving in a different direction as shown by the ionic density map. This is the only example of two ions of the same cluster diffusing in the same direction. At 8 ps the black ion at the top of the cluster moves which judging from the displacement graph is in response to large vibrations of the yellow Na ion at 7 and 8 ps.

The cumulative hop graph, Figure 45c, shows an initial flurry of hops in the first picosecond in response to the nearby vacancy which is then followed by a long period of continual hops. The mid region of the simulation appears to be stabilised by the formation of a quadri-vacancy cluster which involves 6 ions promoted to Na1 sites.

5.8 Na$_x$CoO$_2$ Transition State Search

Although the MD simulations are ideal for determining the type of dynamical processes in these systems, they require very long times simulation times to properly analyse diffusion rates and activation energies. To understand the barriers to diffusion it is necessary to look at averages over all the possible states. The arrangement of neighbouring ions in respect to any hop will affect its activation energy.

To understand why the short hop is so dominant in the MD simulations, a series of three hops including a short-range Na2-Na1 hop, a medium-range Na2-Na2 hop and a long-range cluster to cluster hop were considered. To determine the activation energy between start and end points of a hop, both positions must be optimised so that they are in their local ground states. A transition state search then moves ions between the two states, searching for a saddle point in energy. It is necessary to have true ground energy states when determining the size of the barrier to the hop. All ions are allowed to shift away from the direct path between states to allow the true saddle point to be found.

Transition state searches (TSS) were run using the Complete LST QST protocol of CASTEP, described in Ref. [111]. The algorithm initially identifies the transition saddle point using a Linear Synchronous Transition (LST) search before switching to a Quadratic Synchronous Transition (QST) search using the result of the LST as a guess. This is a highly robust method to discover the saddle points of transitions and is described in more depth in Chapter 3.

5.8.1 Na2-Na1 Short-Range Hop

The short-range hop of a Na ion from a Na2 to a Na1 site was carried out in the ideal stripe phase system. The only ion available to make this hop is the Na2 ion directly between clusters. Figure 46 shows the geometry optimised initial positions of the Na layer containing the hop. The hopping ions initial position is coloured black, the final position is coloured white, and the saddle point of the hop is coloured yellow.

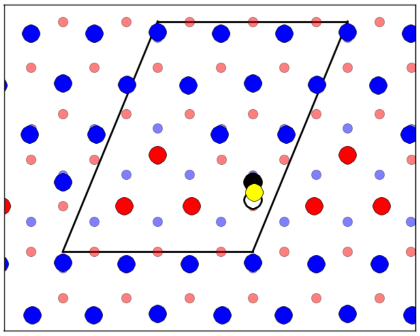

Figure 46: The positions of ions for a short-range Na2-Na1 hop in a stripe phase system. The initial ionic positions are shown according to their Na1, red, and Na2, blue, sites. The initial position of the hopping ion site is shown in black, the final site is shown in white and the transition-state saddle point is shown in yellow.

The ground state energy of the initial stripe system is set to be 0 in energy. When the Na2 ion is promoted to the final state Na1 site, the energy increases by 81.9 meV. The saddle point of the TSS has an energy of 94.2 meV in comparison to the ground state. The discrepancy in site life-times, which is linked to the activation energy barrier of the hop, will lead to the two states having a large difference in average occupancy over time. The reverse hop from Na1 to Na2 site has a barrier of 12.3 meV which is an order of magnitude smaller. This may explain the large amount of immediate reverse hops seen in MD simulations as a lower activation energy signifies a shorter mean residence time for ions and, consequently, a faster hop rate.

5.8.2 Na2-Na2 Medium-Range Hop

A TSS for a Na2-Na2 hop was set up in the disordered phase where these are predicted to occur to some extent. A supercell of 4x4x1 hexagonal cells was created to simulate the diffusional process. The initial state is shown in Figure 47, with all ions in Na2 positions except for isolated vacancies. The transitioning ion is shown in black in its initial position, white in its final position and yellow at the saddle point of the transition. The chosen transition to study involved a vacancy isolated by Na2 ions. Similarly, the final position of the vacancy is surrounded by Na2 ions.

The initial and final states are not symmetric due to a change in the number of next-nearest neighbour Na ions. This leads to a small discrepancy in the geometry optimised ground state energies. The final state is 57 meV lower in energy than the initial state. The saddle point of the transition has an energy of 375 meV from the initial state and 432 meV from the final state. The similarity in the size of the barrier from the two positions will mean that there will only be a small difference in average site occupancy. As there is no quick hop back to the initial state, it may be more likely that other ions can hop into this vacancy.

5.8.3 Na1-Na1 Long-Range Hop

A long-hop simulation was developed to look at the possibility of very long range pathways between adjacent clusters. Using a supercell equivalent to the 2x1x1 stripe cells used in MD simulations, initial and final cells were geometry optimised by removing a single ion from adjacent clusters. The TSS is shown in Figure 48 with the ions coloured according to Na1 and Na2 sites. The transitioning ion is shown in black in its initial position, white in its final position and yellow at the saddle point of the transition.

This long hop involves a long curved path between the initial and final states. Due to the symmetry between the initial and final states, their ground state energies differ by only 1.6 meV. The saddle point is found almost exactly half way between the two sites and has a prohibitive energy ~1300 meV higher than the end points.

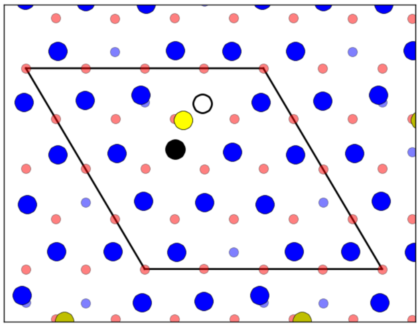

Figure 47: The positions of ions of a medium range Na2-Na2 hop in a 80% concentration disordered phase system with isolated vacancies. The initial ionic positions are shown according to their Na1 and Na2 sites. The initial position of the hopping ion is shown in black, the final site is shown in white, and the saddle point of the TSS is shown in yellow.

5.9 Summary

The ionic diffusion mechanisms of Na_xCoO_2 have been studied by a series of MD simulations. The interactions between ions, controlling the dynamics, have been modelled using the DFT implementation of CASTEP. Constrained by the calculation time and cost, the range of simulations was chosen to provide a broad sampling of the possible ionic arrangements. Subsequent TSS of candidate hops provide an estimate of the activation energy.

Clear distinctions in the level and type of dynamic behaviour were observed between different simulations. These could be linked to the arrangement of ions in the cell, in particular to presence of Na ions on the Na1 site. Their presence leads to local regions of lower ionic density that promote motion of neighbouring Na ions.

The formation of Na1 ions into tri-vacancy clusters for $Na_{0.8}CoO_2$ leads to regions of very mobile ions. The positioning of the clusters relative to each other; as well as

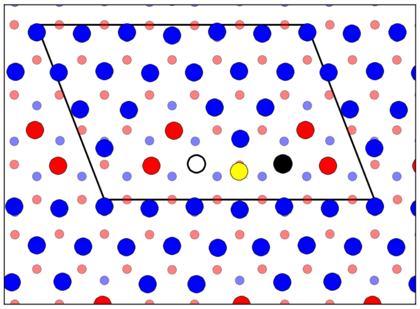

Figure 48: The positions of ions of a long-range Na1-Na1 hop between adjacent clusters. The initial ionic positions are shown according to their Na1 and Na2 sites. The initial position of the hopping ion is shown in black, the final site is shown in white and the transition state is shown in yellow.

changing the level of dynamics observed, also, affects the coherence between subsequent hops. It is necessary to consider the coherence between hops even though this is a difficult process to simulate, particularly over short timescales. An attempt to determine the scale of the coherence between hopping events was made by plotting the graphs of the cumulative number of Na hops between different sites. A rapidly increasing number of hops, in relation to the background, indicates a series of correlated hops. These show up particularly in the extended stripe cell where additional vacancies lead to a significant cascade in the initial picosecond. Cascades of hops are observed to happen at later points in many simulations.

The simulations of the ideal stripe, Figure 30, and square phase, Figure 33, are informative. Both show dynamic events of the ions in the clusters. However, only the stripe system with its connected clusters shows large scale motions and also secondary ions away from the clusters moving. This sequence in which the ions hop while periodically reforming tri-vacancy clusters at different points along the stripe has been identified as the method by which the ions within stripes lose coherence with the ions of neighbouring stripes. Figure 49 demonstrates this by showing the arrangement of ions for the ideal stripe system at the beginning and end of the MD simulation.

The movement of a tri-vacancy cluster along a stripe only requires hops perpendicular to the stripe. This does not lead to any net diffusion of ions as all ions are simply moving back and forth between two sites. To stimulate diffusion along the stripe channels additional vacancies were added. The placement of the new vacancy greatly affected the dynamics of the system. If the vacancy was placed on either of the non-equivalent tri-vacancy cluster Na1 ion sites, Figure 36 or Figure 38, then the diffusion was greatly increased and coherent effects were seen with many hops along the stripes. These processes can, therefore, contribute to bulk diffusion along the stripe.

Placing a vacancy in the Na2 ions close to a vacancy cluster, Figure 37, also made

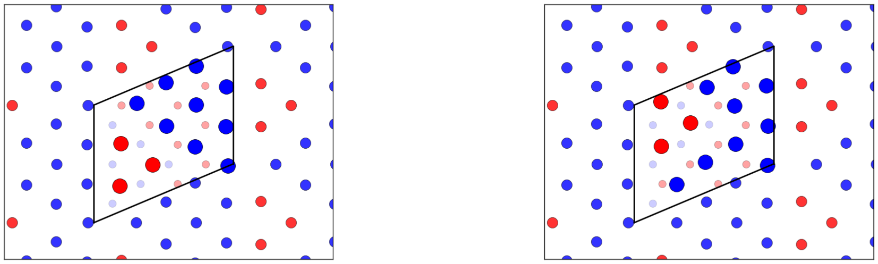

(a) Initial tri-vacancy cluster position (b) Final tri-vacancy cluster position

Figure 49: The positions of a tri-vacancy cluster in the disordered stripe phase near the start and end of an MD simulation, showing the translation of the tri-vacancy cluster along the stripe.

many ions move. Finally, a vacancy was added in a location separated from the tri-vacancy clusters, Figure 39, to investigate whether an additional vacancy away from the stripes would also increase dynamic events. This simulation showed that having a vacancy in this location suppressed the movement of ions. The Na2 ions form barriers to diffusion, leaving one-dimensional channels along the stripes. Hence in the disordered stripe phase there is very little bulk diffusion close to ideal stoichiometry. The introduction of additional vacancies leads to one-dimensional bulk diffusion along the stripes.

The next step was to analyse the motions of ions when there is no superstructure present. Two simulations were carried out; one containing isolated vacancies and one with some local ordering. From diffraction measurements, the presence of glassy mixtures of multi-vacancy clusters has been observed.

Far more events were seen for the locally ordered system, Figure 45, than for the isolated vacancy system, Figure 42. This is attributed to the availability of short range hops which are blocked in the isolated vacancy case. Despite the higher temperature, only one hop is observed in the entire isolated vacancy simulation. This would indicate that the presence of multi-vacancy clusters continues to be important at high temperature for diffusion in the disordered phase.

After identifying the dominant hops in the $Na_{0.8}CoO_2$ system, TSS were setup to verify why the short hop was dominant. These consisted of a short Na2-Na1 hop similar to those observed in most simulations, a medium-range hop observed in the isolated vacancy simulations and a long-range hop proposed as a possibility to create very fast diffusion rates along the stripes.

The activation energy of the short-range Na2-Na1 hop was calculated to be 94.2 meV with its reverse hop having a smaller barrier of 12.3 meV. In comparison the cost of a Na2-Na2 hop is $\sim$ 400 meV, a factor four increase at best. Even as a rough estimate of the activation energies of all hops of these types, the difference is scale will lead to the dominance of the short range hop. The pathway traced by the Na2-Na2 hop passes very close to a Na1 site. This may also inhibit the occurrence of longer hops as ions in a system where the Na1 site is available may always remain at the Na1 site for a short time. The long range hop was calculated to have an activation energy of $\sim$ 1300 meV which almost certainly prohibits the possibility of Na ions diffusing by this process.

6 $Na_{0.8}CoO_2$ QENS on OSIRIS

Quasi-Elastic Neutron Scattering is a powerful probe to study short range dynamics of crystalline systems. The time dependency of incoherent motions coupled with structural knowledge provides a realistic snapshot of the range of dynamics present. The theory behind QENS has been discussed in Chapter 2.

The similarities of Na_xCoO_2 to Li_xCoO_2 make it an incredibly interesting and relevant battery material. As discussed in section 1 and shown in Figure 2, the two systems share a similar layered structure with the mobile Na and Li ions sandwiched between static layers of Co and O ions. The structures differ in that the Hexagonal symmetry of the P2-Na_xCoO_2 opens up a second stable site, allowing new shorter pathways in comparison to the O3-Li_xCoO_2.

The Na_xCoO_2 does have slightly larger (in plane) *a* and *b* lattice parameters at 2.855 Åin comparison to Li_xCoO_2's 2.816 Å, however this is expected to have only a marginal effect in contrast to the additional pathways and positioning of the O ions. Perpendicular to the plane there is a larger difference with an inter-planer Co distance of ~ 5.4 Åfor Na_xCoO_2 and only ~ 4.7 for Li_xCoO_2. As a result the O ions are more spaced out in the Na_xCoO_2 which may lead to lower activation energies for the Na ion, although this may be negated by the Li ions smaller ionic radius.

Subsequent to the initial experiments given in this thesis, a different research group has shown preliminary QENS investigations of Na_xCoO_2 [155]. The paper by Juranyi et al. shows the presence of Lorentzian broadening at elevated temperatures however the data is insufficient to establish a Q or Temperature dependence.

Voneshen et al. have seen large vibrational rattling modes associated with the disordered stripe phase [121]. The direction of the vibration coincides strongly with the direction of a Na1-Na2 hop and therefore may act to enhance the diffusion effect of ions out of tri-vacancy clusters.

The following chapter contains experiments carried out on the time-of-flight indirect geometry instrument OSIRIS and details the analysis that provides an understanding of the diffusion mechanisms of $Na_{0.8}CoO_2$. Although the use of bulk measurements allows an estimate of the diffusion rate, they often underestimate diffusion due to boundary effects between crystallites. QENS experiments determine the diffusion from processes happening within each crystallite, therefore are not hindered by boundary effects making them an excellent probe.

6.1 Experimental Setup

The ordering of $Na_{0.8}CoO_2$ with temperature has been discussed widely in Chapter 4. The dynamic regime begins at 280 K as the sample enters the disordered stripe phase. Above 600 K the crystal structure softens and the crystal structure begins to melt [156]. Samples were mounted in a top loading pulse tube cryofurnace which has an operating window of 4 K to 673 K, covering the useful range of the sample.

In the initial experiment, a 1.96 g single crystal was mounted on an Al plate using Al wire so that the hk0 plane of the sample coincided with the horizontal plane of the detectors. Al was used due to its low incoherent cross section, minimising its contribution to background. It was necessary to carefully clean all mounts to remove all possibilities of hydrogen due to its large incoherent cross section and its mobility which would have created a large secondary QENS signal. The powder experiment used an Al container; in this case a cylinder of 14 mm diameter and 50 mm height.

The maximum amount of sample is chosen according to the absorption and scattering cross sections, which are given in Table 1 for the relevant ions. The absorption cross sections given are for thermal neutrons, however the low energy of the hydrogen moderated neutrons leads to an increased absorption cross section. Li has been included for reference with Na, Al has been included to show why it is a useful sample environment material, and H has been included to show why the any contamination has to minimised.

The diameter of the sample was chosen to maximise the scattered proportion of neutrons. Although having a larger sample would increase the scattering, it would also increase the absorption and as such the scattered portion is below 10%. Additionally, this is significantly below the threshold at which multiple-scattering events significantly effect the measured signal. The height of the cylinder is slightly larger than the beam size as this allows for a small error in the vertical position while still ensuring that the beam interacts with the maximum amount of sample. Al heat shields with a 10 cm diameter were placed around the samples to enable heating to higher temperatures. The collimation on OSIRIS removes the majority of the scattering signal of these shields.

The useful scattering power is determined by the amount of Na ions and their incoherent cross section of 1.62 barns. The Co, Al and O ions create an incoherent static background due to their non-zero incoherent cross-sections of 4.8, 0.0082 and 0.0008 barns respectively [58]. The relative scale of the cross sections makes it clear that the overwhelming majority of the background signal comes from the Co despite the far greater mass of Al in the sample mounts. There are also 5 Co ions for every 4 Na ions therefore at most 21.1% of the total incoherent signal is from the Na. It is necessary to have large counting times to compensate for the large signal to background ratio. To ensure there was no contamination from hydrogen, which has a cross section of 80.26 barns, the sample containers were carefully handled and washed with acetone. Once in place the sample was heated above the boiling point of water, while the atmosphere was pumped out, to remove any water vapour that may have condensed on the system.

An initial scan of the powder sample was carried out for 12 hours at 200K, signifi-

Isotope	b_{coh} (fm)	b_{inc} (fm)	xs_{coh} (barn)	xs_{inc} (barn)	xs_{scat} (barn)	xs_{abs}/ barn
Na	3.63	3.59	1.66	1.62	3.28	0.53
Co	2.49	-6.2	0.779	4.8	5.6	37.18
O	5.803		4.232	0.0008	4.232	0.00019
Li	-1.9		0.454	0.92	1.37	70.9
Al	3.449	0.256	1.495	0.0082	1.503	0.231
H	-3.7390		1.7568	80.26	82.02	0.3326

Table 1: Relevant neutron scattering lengths and cross sections for $Na_{0.8}CoO_2$, as reported in [58]. The columns are, from left to right: bound coherent scattering length, bound incoherent scattering length, bound coherent cross-section, bound incoherent cross-section, total bound scattering cross section and absorption cross-section. The absorption cross-section is given for neutrons at 2200 m/s.

cantly below the temperature onset of diffusive processes, before being compared to a vanadium Background. The scattering pattern was determined to be static within the instrumental resolution. Limited knowledge of the diffusion rate made it necessary to take long measurements over the entire dynamic range.

Twelve hour measurements at 350 K and 450 K showed only small differences when compared directly to the resolution limited function. For later twelve hour measurements at 500 K, 550 K and 600 K the difference became much greater. To provide a large temperature base line for analysis of the diffusion mechanisms, further measurements at 200 K, 350 K and 450 K were carried out for a total of 36 hours. This reduced the statistical uncertainty significantly making differences between the dynamic and static regimes readily apparent. Additional one hour measurements were taken in the disordered stripe and ordered stripe phase. Low diffusion rates made it preferable to use the PG002 reflection of the analyser bank which has a resolution of 25.4 μeV; an almost 4 factor improvement compared to the 99.0 μeV of the PG004 reflection resolution.

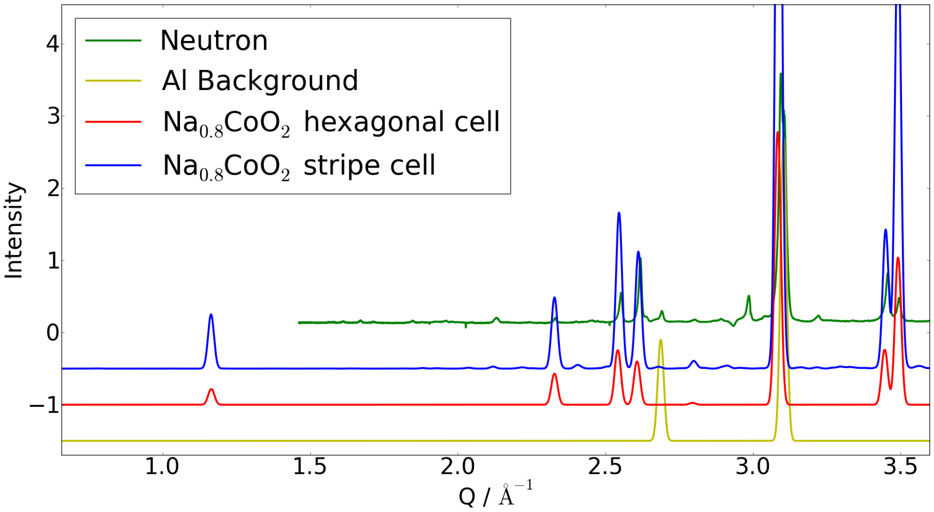

Figure 50: The scattered intensity for a powder sample of $Na_{0.8}CoO_2$ at 200K using the OSIRIS diffractometer. The Neutron powder diffraction profile is shown in green, while the predicted diffraction patterns of the hexagonal phase and stripe phase of $Na_{0.8}CoO_2$ and the aluminium background are shown in red, blue and yellow, respectively.

The Q range drops from 0.37-3.6 Å to 0.18-1.8 Å with the change from the PG004 to the PG002 reflection. Without a long baseline in reciprocal space, it is challenging to fit an accurate dependence to the hop length particularly when that hop length is short. The higher the Q value; the more likely the occurrence of Bragg peaks which lead to a large amount of elastic scattering, obscuring the QENS signal. For the single crystal system the $Na_{0.8}CoO_2$ Bragg peaks can be avoided by careful orientation of the sample, however it is impossible to avoid the Bragg lines from the Al and the powder system.

Figure 50 shows the diffraction pattern of $Na_{0.8}CoO_2$ at 200K measured with the

OSIRIS diffractometer. Additionally, predicted diffraction patterns from the $Na_{0.8}CoO_2$ hexagonal phase and the stripe phase are shown. The predicted diffraction pattern from the aluminium sample environment is also shown. Consistency is observed between the positions of the largest peaks of the stripe and hexagonal phases which line up with the largest peaks observed experimentally. At high Q values, the aluminium causes two large Bragg peaks however given the small unit cell there are no peaks at low values.

There are a number of low intensity peaks that are not explained by the simple hexagonal $Na_{0.8}CoO_2$ cell; most of these can be explained by scattering from the supercell of the ordered stripe phase, given by the blue line. These are much smaller than the peaks associated with the hexagonal cell. A few additional peaks, for example at 3 $Å^{-1}$ may be due to contaminates such as Al_2O_3. Given the density of peaks at high Q, it makes sense to use the PG002 reflection to study a region in higher resolution away from potential sources of interference. The exception to this is the [002] Bragg peak from $Na_{0.8}CoO_2$ at 1.16 $Å^{-1}$. The detectors affected by scattering from this Bragg peak will be discounted and not included in any fitting.

Thermal conductivity is another key consideration of the experiments. Accurate knowledge of the temperature difference between the sample and the temperature control is necessary to produce accurate temperature dependences. At low temperature, beneath 380 K, the thermal equilibration is enhanced by the presence of a small amount of helium exchange gas, however at higher temperatures it is necessary to place the sample under vacuum to avoid softening or melting the seals on the cryofurnace. The low surface area in contact between the single crystal and sample mount meant that there was a significant difference particularly at high temperature. Sample temperature is measured by a nearby copper thermometer however this cannot be in direct contact with the sample as it would also scatter and therefore an additional error is introduced into the system because of this distance. In contrast the powder sample had a large surface in contact and it was possible to attach the thermometer near the top of the mount greatly reducing the problem. At temperatures beneath 450 K the temperature difference was within a few K which then rose to 20 K at 600 K.

6.2 Energy Lineshape

The incident neutrons of each pulse are recorded as counts in a series of time bins associated with each detector. Data reduction used the MANTID software package [157], with **Q** assigned based on the detector position and analyser reflection used. The time of flight necessary for a neutron to arrive at a specific bin informs on the amount of energy that must have been lost or gained in through its interaction with the sample. The zeroth bin is defined as fulfilling elastic scattering and the surrounding time bins are set according to the difference between incident and final energy of the neutrons.

The number of neutron events per energy bin can be plotted on a single graph called the energy lineshape. For a sample with static ions, the profile is the resolution of the instrument defined by a combination of the incoming neutron beam energy range, determined by the moderator, and the viable scattering pathways from the analyser crystal through the collimator's. The data can be re-binned, by grouping detectors or energy bins, reducing numerical noise but losing instrument resolution. A measurement of a vanadium sample is used to calibrate the efficiency of each individual detector.

The 200 K, blue curve, of Figure 51 shows the asymmetric resolution function while the 550 K, red curve, shows the dynamically broadened curve. The small difference is caused by the comparatively large incoherent contribution of the Co atoms and made it necessary to have long count times. Despite this, the change is noticeable between high and low temperature.

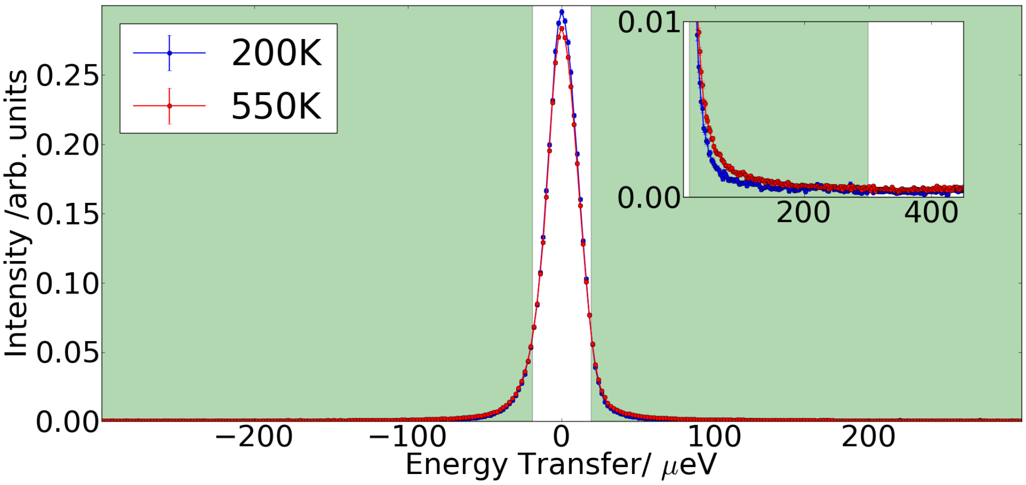

Figure 51: A comparison of the energy lineshape of the static regime at 200 K, blue, and the dynamic regime at 550 K, red. The green shaded region covers the quasi-elastic region. The inset shows a magnified version of the quasi-elastic region emphasising the difference between the low and high temperature regimes and showing the intensity level in the background region.

6.2.1 Intensity Analysis

The first analysis is a study of the integrated intensities of different regions of the energy lineshape. Figure 51 is divided into an elastic, quasi-elastic and background region, dependent on the change in energy from the zeroth energy transfer position. The elastic region, centred on zero energy transfer, contains the bulk of the intensity particularly in static regimes. As temperature increases it is expected that the intensity will drop linearly due to the Debye-Waller effect, caused by ions vibrating around their normal positions. If the system develops ionic hopping motions then the subsequent QENS signal will further reduce the intensity departing from the linear behaviour expected from Debye-Waller. Although this bears some resemblance to the EISF technique, the presence of the Co signal prevented attempting to divide the Na signal into elastic and quasi-elastic components. Instead this simply calculates the change of total intensity in each region as a function of temperature for a fixed Q.

The wings of the energy profile, shown as green in Figure 51, will increase in intensity in the presence of QE scattering. If the sample was static then as temperature rises the intensity will decrease due to Debye-Waller. However, an increase will occur due to a rising background level caused by scattering from the phonon density of states. The background level at each temperature can be subtracted by calculating its scale suitably far out from the elastic peak. The boundary of the quasi-elastic region was defined as starting at 1.5 times the HWHM of the PG002 resolution limited function and extending out to 300 μeV. The background level is then obtained from the intensity between 300 μeV and 450 μeV.

Figure 52 shows the normalised intensity dependence on temperature of the elastic and the quasi-elastic regions for the powder and single crystal experiments. The boundary of the QE region for the single crystal experiment starts at 1.5 times the HWHM of the PG004 resolution and ends at 740 μeV. The background range then runs from 750 μeV to 1000 μeV. All data sets have been calibrated using the 200 K data as a reference point to remove biases in intensity between different detectors caused by the sample geometry.

In the ordered stripe phase, the behaviour of the curves is essentially flat with the single crystal measurements showing a slight change beginning at 250 K. In the powder experiment a smaller change recorded at 300K however the experiments are consistent within the error bars. As the samples enter the disordered stripe phase a consistent linear increase begins that continues into the disordered phase, particularly for Figure 52b. In the quasi-elastic case, Figure 52a, the increase in intensity appears to be tailing

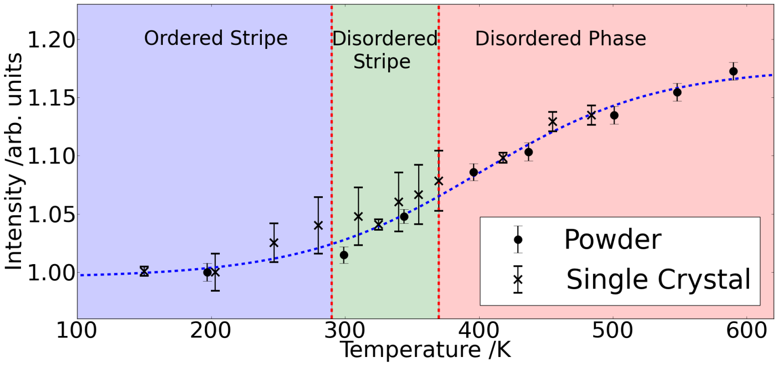

(a) Quasi-elastic intensity, integrated between ±19 μeV < Energy < ±300 μeV. The single crystal measurement uses a larger range and is normalised by the 200 K data

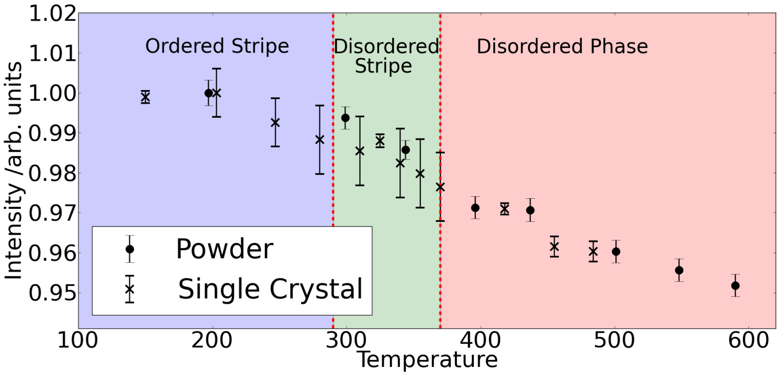

(b) Elastic intensity integrated between -19 μeV < Energy < 19 μeV. The single crystal measurement uses a larger range and is normalised by the 200 K data set.

Figure 52: The integrated intensities of the quasi-elastic and elastic regions as a function of temperature for powder and single crystal measurements. The integration ranges are given for the powder PG004 reflection with the single crystal PG004 having a range $\sim$ 4 times as big and then having been renormalised based off of the 200 K and 500 K data. The Q range for both is from 0.3 Å^{-1} to 1.8 Å^{-1}.

off above 500K giving a complete behaviour that can approximately be modelled by a sigmoid function, dashed blue line. This behaviour, in conjunction with the continual loss of intensity from the elastic peak, is consistent with a quasi-elastic signal exiting the viable range of the instrument.

6.2.2 Fitting the Energy Transfer Lineshape

The energy transfer lineshape of all the temperature and Q values can be explained by determining the underlying functions that describe the level of broadening. In the ideal case, the profile is described by the equations given in Section 2.1.6. If the resolution function is known then it is easy to calculate the profile by first splitting the signal into static and dynamic contributions. The static contribution is described by a delta function and the dynamic contribution is described by a Lorentzian function that narrows into a delta function as the temperature drops and the diffusive motions stop. The two contributions can then be convolved with the resolution function to give the exact profile.

$$Signal(x) = Resolution(x) \otimes \big(Static(x) + Dynamic(x)\big). \tag{52}$$

The contributions are normalised to unity and a mixing factor is applied determining the proportion from each regime, with a further multiplication by an amplitude factor to restore the correct intensity. An additional background constant is also added as this helps the fitting of data far away from the elastic peak preventing anomalously wide Lorentzian widths.

Figure 53 shows the energy lineshape of a mid-range Q, 1.37 $Å^{-1}$, and high temperature, 560 K, as an example of the fitting routines. It is necessary to create a fitting routine that can accurately and reliably fit multiple data sets at all temperatures and Q. Figure 53a shows an attempt to fit the data by scaling the resolution-limited func-

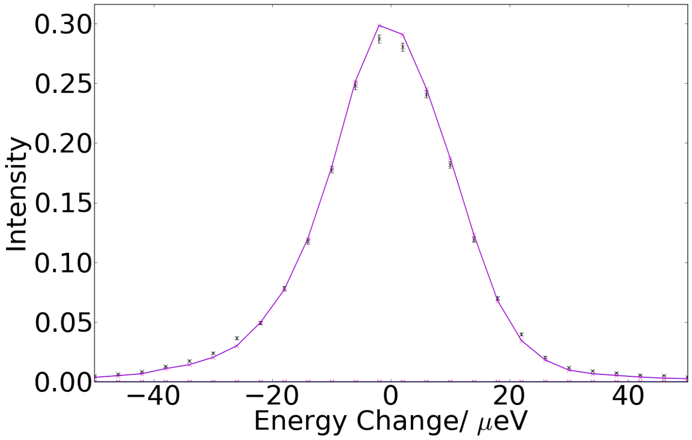

(a) Fitting using only the resolution function with a fitted intensity.

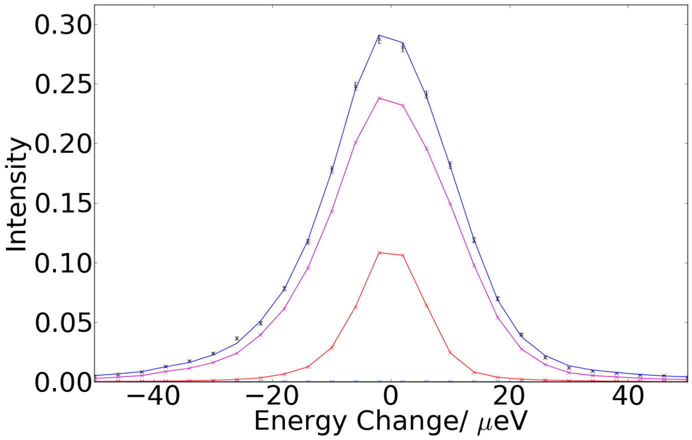

(b) Fitting with a resolution and convolved Lorentzian-resolution function with a fitted width and intensity.

Figure 53: An example energy lineshape at 560 K and 1.37 Å^{-1}. a) simply fits the resolution function to the high temperature data. b) introduces a fixed 21.1% dynamic component with a variable width and intensity. Both graphs have a small background level visible as a blue line with a levels of ~ 0.0002 Arbitrary units.

tion to the high temperature data. The fit is systematically too high near the elastic peak and too low in the Quasi-Elastic wings.

Figure 53b introduces a dynamic component, 21% of the total intensity, decided by the amount of Na in the system, that allows the fitting of the Na ion hops. The dynamic component is formed of a Lorentzian, whose freely varying width allows for fitting of the wings, which is then convolved with the resolution-limited function. The remaining 79% is given by the resolution limited static function.The total intensity of the static and dynamic components are then fitted using a freely varying amplitude factor. The final figure shows much better agreement over the whole of the lineshape. The fixing of the fraction of dynamic and static contributions was necessary to ensure reliable intensities particularly at low Q where the broadening is smaller. This assumes that all Na's are mobile in the disordered phase as long range correlations have broken down.

The behaviour of the background and the amplitude of the fitted lineshape are shown in Figure 54. The background has been fitted as a sloping line due to a higher intensity on the positive side of the ETP, however the gradient is so small that this is almost flat. The intensity parameter is the amplitude factor necessary to scale the unity normalised static and dynamic components to the data. The intensity is dominated by the Q points where Bragg lines occur, most significantly the [002] and also at the highest Q. Other problems occur at low Q, which is likely to be caused by low counting statistics and interference from the straight through beam. These low points are also seen as being anomalous in the fits of the Lorentzian HWHM at all temperatures and therefore have been excluded from later analysis.

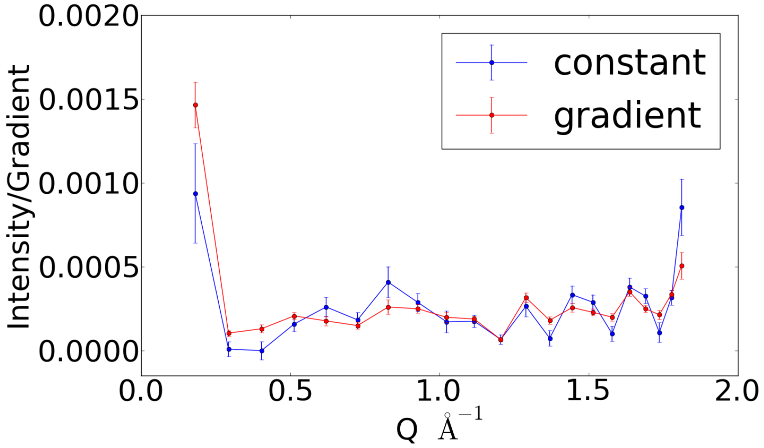

(a) Background parameters fitted at each Q position.

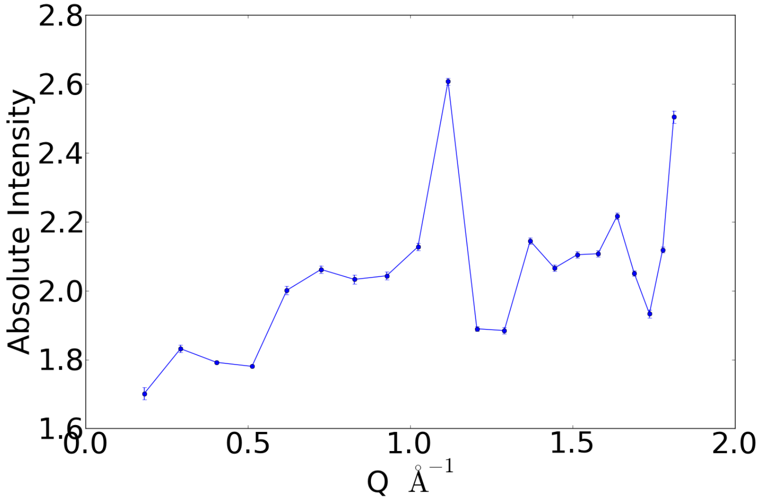

(b) Intensity parameter fitted at each Q position.

Figure 54: The fitted parameters for all Q positions of the 550 K data set. The background is fitted by a sloping line with the gradient and level shown in a). The Intensity parameter fits the amplitude of the Lorentzian broadened profile to the actual data.

6.2.3 Q Dependence

Section 2.3.1 discusses the theory behind the Chudley-Elliot model used to fit the Q dependence of the HWHM. The model fits the average residence time before a hop, which is inversely proportional to the observed Lorentzian HWHM. The model takes into account the possible hops inherent in 2D hexagonal planar diffusion.

The initial single crystal experiment suggested the presence of QE broadening in $Na_{0.8}CoO_2$ however the resolution of the PG004 analyser reflection and the low sample mass makes it difficult to determine reliable Q dependencies. The second experiment using the powder sample focussed on the higher resolution PG002 analyser reflection. The crystals of a powder are randomly orientated in all directions in 3 dimensional space and the vectors of the diffusion mechanisms are lost. The hop mechanisms in a powder resemble an isotropic liquid with hops happening in all directions with a hop length decided by the local environment, although in the crystalline powder case the length is heavily constrained. The Q dependence can be expressed by Eq. (29), restated here:

$$\Gamma(\mathbf{Q}) = \frac{\hbar}{z\tau} \sum_{j}^{z} (1 - \exp(-\mathrm{i}\mathbf{Q}.\mathbf{l}_j), \tag{53}$$

where the Lorentzian width, Γ, depends on the average residence time, τ, and each hop, $\mathbf{l}_j$ with z being the coordination number, determined by the number of available hop pathways [46]. At each temperature, a time parameter is fitted along with a hop length which can either be assumed or fitted. The possible hops, $\mathbf{l}_j$, correspond to forward and backward motions between red and blue sites. The orientation of the crystallites with respect to the detectors determines the behaviour of the exponential term. A powder average can be represented by numerically averaging the summation for all orientations of crystallites within the irreducible wedge, assuming an even distribution of crystallite orientations in all directions.

For short Q ranges it is extremely difficult to discern between different length hops as the Q position of the maximum Lorentzian width is related to the reciprocal of the hop length. Although the behaviour of each curve diverges at high Q, for the majority of the experimental Q range there is almost no difference in the predicted line shape. The analysis of the computational simulations however clearly indicates a strong preference for the short range Na1 to Na2 site hops. Although evidence for the longer range hops was observed in some simulations, they were significantly less frequent and had a larger activation energy inhibiting their contribution. The diffuse scattering observed at high temperatures also strongly indicates the existence of local ordering which exists in the form of tri and di-vacancies clusters. The combination of these two factors provides the basis for the assumption that the diffusion is caused by the short range diffusion. An attempt was made to model the dependence using a combination of the two hops however in all cases the time parameters of the hops were fitted so that one hop contributed nothing while the other actually fitted the Lorentzian width.

The Q dependence of the Lorentzian widths, at all temperatures, are modelled with a fixed hop length of 1.65 Å and a varying average residence time, τ. The fitted temperature graphs are shown in Figure 55. At all temperatures the Lorentzian widths fitted from the energy line shapes are displayed at their Q position. The Q dependence is then fitted to these Lorentzian widths and it is clear that it is small or zero at low Q and then rises through the mid Q range. At high Q there is a suggestion that it begins to plateau however the scale of the error does not confirm this.

The scale of the fitted dependence increases with temperature, as shown in the final graph of Figure 55 and this corresponds to a decreasing residence time. In the disordered stripe phase the level of broadening is low compared to the scale of the error bars but it does visibly increase with Q especially for the 350K data. As the sample

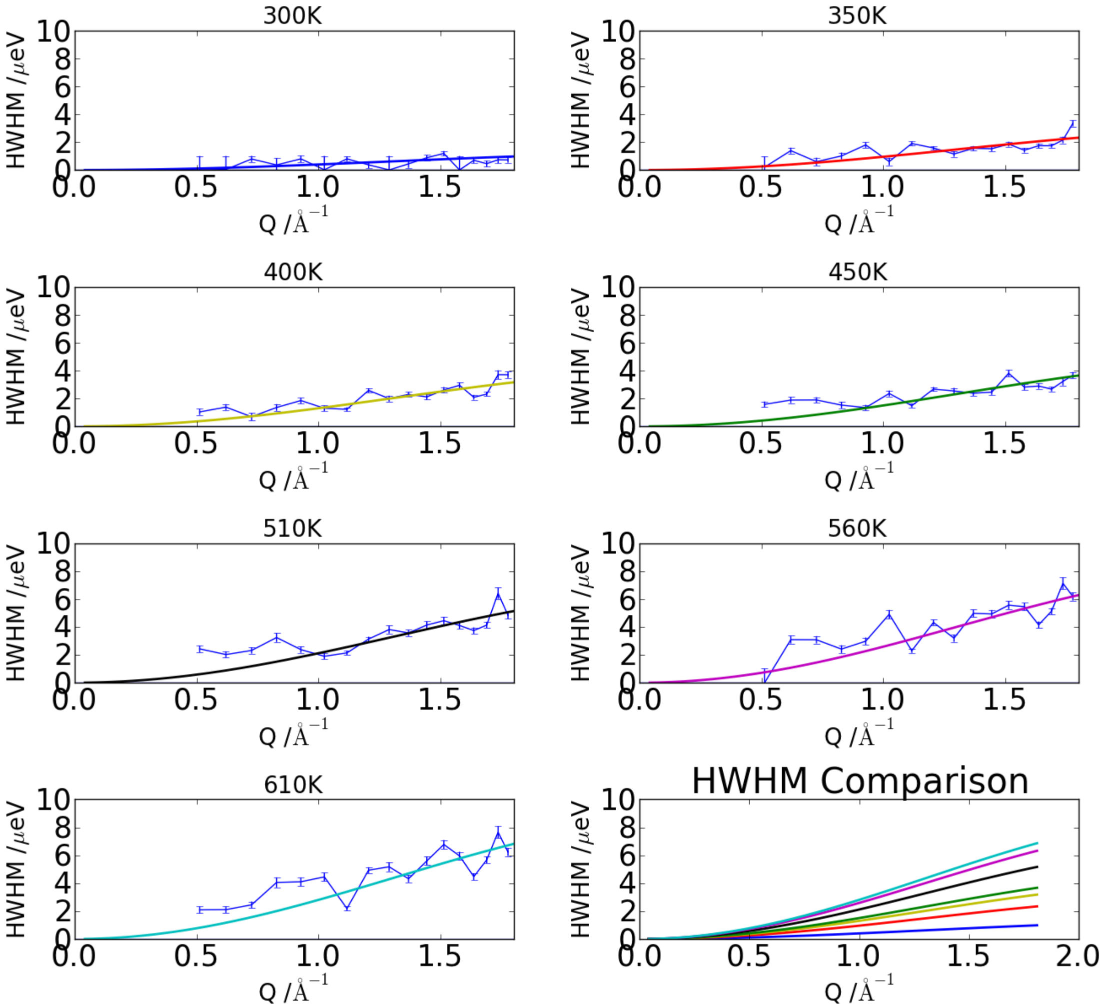

Figure 55: The fitted Lorentzian half width half maximums for each temperature measured using the PG002 analyser reflection. The final plot compares the fitted lines with each line colour coded to match the individual temperature plots. The lines are fitted, using variable time and fixed hop length parameters, according to the Chudley-Elliot Model for powders.

transitions into the disordered phase, the broadening increases. A large jump is seen at 510K which is similar to the temperature at which diffuse scattering is seen to diminish. The final two temperature graphs are again very similar suggesting there is only a small increase in diffusion rate. Alternatively at the highest temperature, the diffusion may be becoming too fast for the instrument and therefore merging with a background.

6.3 Diffusion rate

The change in the average residence time, τ, with temperature is determined from the final graph of Figure 55. The progression of τ is important in revealing how quickly the rate of diffusion is occurring. If the ions are spending less time on average in each site then they must be diffusing quicker though the sample material. The rate at which τ changes with temperature is linked to a parameter known as the activation energy, E_a, which defines the energy barrier between stable sites. If E_a is known then $\tau(T)$ can be calculated using the following formula:

$$\tau(T) = \tau_0 \text{exp}(\frac{E_a}{k_b T}), \tag{54}$$

where τ_0 is a constant to which τ(T) converges as temperature increases. This equation is used to fit the rate of increase in both the disordered stripe and disordered phase, shown in Figure 56. The series of 5 points in the disordered phase allow a real fit to be carried out however as there are only 2 point in the disordered stripe phase this is not possible. Instead the errors in E_a and τ_0 must be estimated based off of the scale of the errors in τ(300 K) and τ(350 K).

In the disordered phase values are calculated for E_a as 84(5) meV and τ_0 as 13(2) ps. The red line of Figure 56 provides a good fit to the τ values and appears to be plateauing which is predicted by the equation. In the disordered stripe phase E_a is calculated as 170(20) meV and τ_0 as 0.7(1) ps. Consequently the E_a which is almost doubled leads to

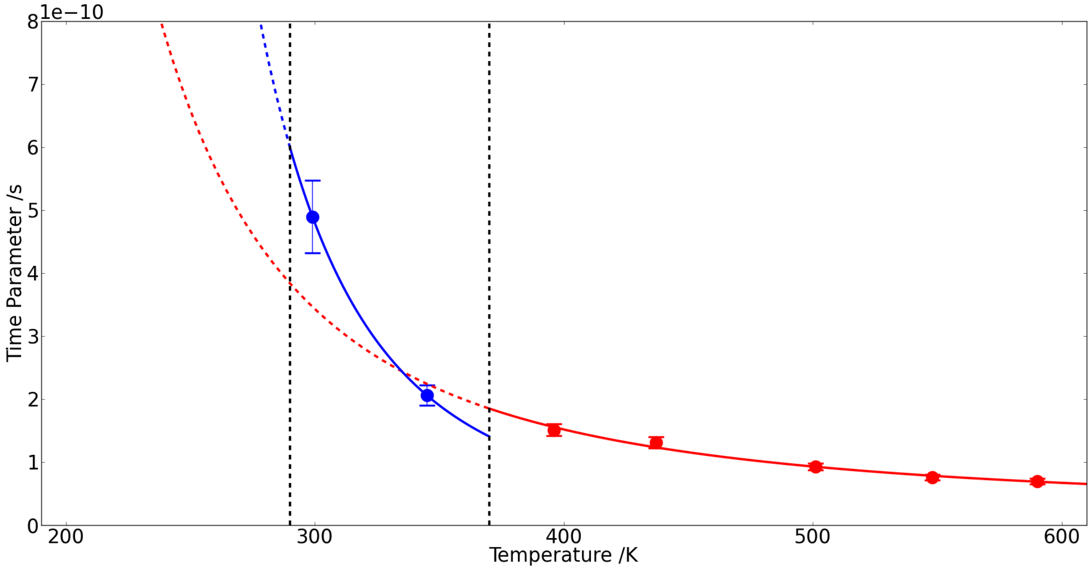

Figure 56: The values of τ fitted in the curves of Figure 55. The temperatures are divided into the disordered stripe phase, blue, and the disordered phase, red, with each region fitted by its own curve according to Eq. (54).

a much lower predicted plateau that is an order of magnitude faster. This is shown by the much steeper blue line which predicts the rapid slowdown of hopping as the sample approaches the ordered stripe phase.

The diffusion, at each temperature, is calculated based off of the hop length, l, and the dimensionality of the available hops in the system, known as the coordination number d, given by the equation:

$$D_0 = \frac{l^2}{2d\tau_0}. \tag{55}$$

For a hexagonal planar system with diffusion consisting of short range hops the coordination number is 3 which is multiplied by a factor of 2 for forward and backward motions. $D(T)$ can then be calculated using a formula similar to Eq. (54). This means as the temperature increases the exponential goes to 1 and the the diffusion rate plateaus at D_0. The diffusion constant is $3.4(4) \times 10^{-6}\,\mathrm{cm^2\,s^{-1}}$ and $6.1 \times 10^{-5}\,\mathrm{cm^2\,s^{-1}}$ in the disordered stripe and stripe phase respectively.

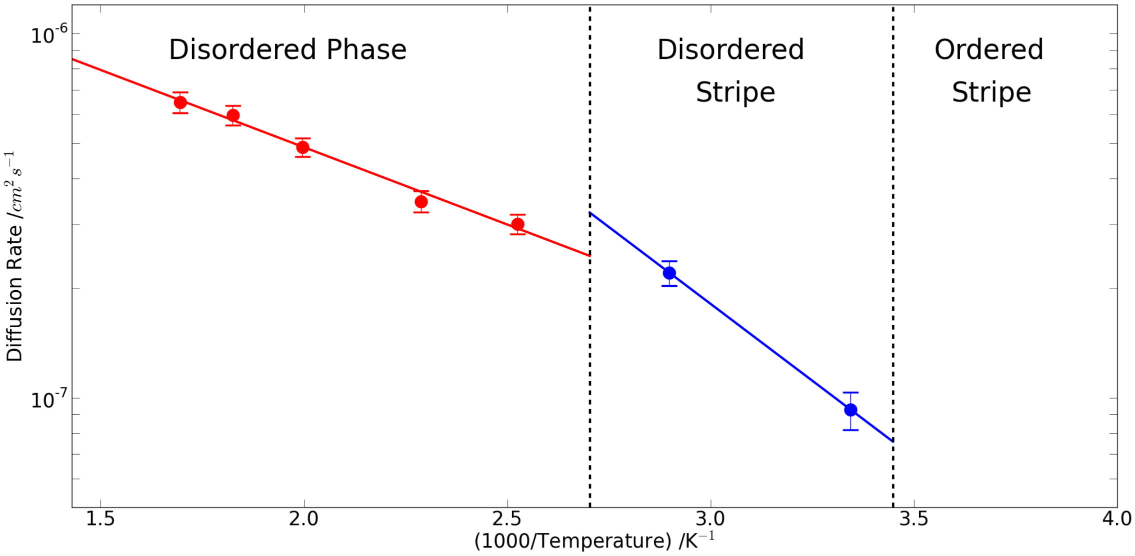

Figure 57: An Arrhenius diffusion plot of $Na_{0.8}CoO_2$ based off of the Chudley-Elliot fitted Q dependence of the Lorentzian widths at each Temperature. The blue line is fitted in the disordered stripe phase and the red line is fitted in the disordered phase.

An Arrhenius diffusion plot is used to display the diffusion rate as a function of Temperature. The log of the diffusion rate is compared against an inverse temperature. This produces a straight line for the diffusion rate where the activation energy does not change. Figure 57 shows the linear relation of the diffusion rate in the disordered stripe, blue, and the disordered phase, red. A clear change in gradient can be seen between the two phases.

6.4 Discussion

QENS measurements of $Na_{0.8}CoO_2$ have been carried out at a range of temperatures, covering the three main phases, to investigate their respective levels of diffusion. The onset of diffusion as the sample enters into the disordered stripe phase has been confirmed by simple intensity analysis of the energy transfer profiles. The intensity of the quasi-elastic region is observed to increase with the onset of the disordered stripe phase. A later plateau is observed at high temperatures in the disordered phase. The diffusion rate at 300 K has a value of $6.5(8) \times 10^{-8}\,\mathrm{cm}^2\,\mathrm{s}^{-1}$ which is in close agreement with the rates obtained using PITT measurements at concentrations of Na > 0.5, $D^{\mathrm{PITT}}_{\mathrm{Na}} = 1.2(5) \times 10^{-7}\,\mathrm{cm}^2\,\mathrm{s}^{-1}$ [41]. For comparison, in Li > 0.5 in Li_xCoO_2 the diffusion rates are much lower at $D^{\mathrm{PITT}}_{\mathrm{Li}} = 6.4 \times 10^{-12}\,\mathrm{cm}^2\,\mathrm{s}^{-1}$ [158]. This is more equivalent to the diffusion coefficients extracted by the Na PITT experiment when the system is in a constricting super structure.

More complex fitting of the QE behaviour, using the Chudley-Elliot formulation, has shown similar behaviour with the development of large Lorentzian widths coinciding with the phase transition to the disordered stripe phase. At higher temperatures the fitted diffusion rate appears to level off. This behaviour of the diffusion rate in the disordered phase is easily modelled by a straight line in the Arrhenius diffusion plot, Figure 57. The Arrhenius dependence indicates that the dominant mechanism of diffusion is unchanged throughout this phase. If a second mechanism became dominant then it is expected that it would depend on a different activation energy resulting in a deviation from the linear fit. A deviation is observed between the disordered stripe and disordered phase suggesting the change in ordering results in a larger activation energy.

The level of ordering in the sample and the diffusion behaviour in each phase is linked, with the reduction in the number of additional superstructure peaks as the sample enters the disordered stripe phase being interpreted as the loss of coherence between tri-vacancies of different stripes [128], as Na ions are allowed to move perpendicular to the stripes. The movement of ions around the tri-vacancies, resulting in their translation along the stripes, has been observed in the MD simulations of Chapter 5. The Na ions for the disordered stripe phase can roughly be divided into either a mobile or static group dependent on their proximity to the tri-vacancy clusters. This lowers the proportion of dynamic incoherent scattering ions. Given the energy costs of forming a tri-vacancy structures [36], the increase in activation energy observed in comparison to the disordered phase could be attributed to the effort necessary to disrupt the stripe phase.

As the sample enters the disordered phase the stripe ordering completely breaks down. Diffuse scattering has been observed up to temperatures of $\sim$500 K indicating the continued presence of clustering. The disruption of the ordering indicates that all Na ions can now be considered involved in the diffusion mechanism. The presence of clusters allows the diffusion to continue to operate by the short Na1-Na2 hop mechanism. If the clusters were to completely break down then hops would only occur via Na2-Na2 hops which have a larger activation energy.

QENS has been considered for many years as a probe for understanding the diffusion mechanisms in battery materials, particularly for Li-ions [159]. It is only in recent years, at similar times to the experiments described in this thesis, that the first successful experiments have been carried out although these concern Li ions [160, 161]. The experiment described in this Chapter goes beyond the cited work by analysing the Q dependence at multiple temperatures to provide an activation energy that is directly comparable to bulk and computational methods.

7 $Li_{0.29}La_{0.56}TiO_3$ Structure and Dynamics

Since the discovery of fast ionic conductivity in $Li_{0.34}La_{0.51}TiO_{2.94}$ by Inamuga et al. [162], interest into the compound and related structures has led to a vast amount of research. The system is based on a simple perovskite unit cell with a shared site for the La and Li ion, surrounded by TiO_6 octahedra. The formula for the occupancies of Li and La in the system is given as $Li_{3x}La_{\frac{2}{3}-x}\Box_{\frac{1}{3}-2x}TiO_3$, where $\Box$ indicates the number of vacancies. This formula preserves the number of outer shell electrons in the system, as 3 Li^+ ions balance a single La^{3+} ion. The high conductivity, initially explained by the large amount of equivalent sites, was quickly replaced by explanations involving the tilting of TiO_6 octahedra [163].

The fast diffusion is also linked to the large free volumes that the Li ions have to migrate through, caused by the comparatively large ionic radius of the La. The La ions have an ionic radius of 1.032 Å while the radius of the Li ions is smaller at 0.76 Å [164]. Studies doping the La site with Sr, which has a larger ionic radius, found that the ionic conductivity increased [165]. Similarly when the La site was exchanged for a different lanthanide ion with a smaller ionic radius, the Li ion conductivity was observed to decrease [166]. The Li-oxygen coordination number has also been investigated, and comparisons of different $Li_{3x}La_{\frac{2}{3}-x}\Box_{\frac{1}{3}-2x}TiO_3$ structures show that the fastest diffusion occurs when the Li ions are situated at the centre of the A site, sharing the site occupancy with the La ions[20]. In this positions the Li ions are 12 fold coordinated, whereas away in off center positions they only are 4 fold coordinated.

Ordering of the La ions was also investigated for its effect on the diffusion rate. It has been proposed that ordering the La into alternating layers promotes the diffusion within the layers while inhibiting the diffusion perpendicular to the layers. The relationship of La ordering with Li diffusion is not linear [167, 168]. Instead high Li diffusion rates are a compromise between the proximity of vacancies, enhancing diffusion, and an increasing activation energy due to constriction of the layer, inhibiting diffusion.

The idea of alternating La rich and La poor layers is supported by X-ray and neutron powder diffraction which is commonly refined as a tetragonal cell with the symmetry P4/mmm [169, 170, 171]. The tetragonal cell contains two full perovskite cells with some distortion created by an imbalance in the occupancies of the La/Li site. An early study by Fourquet et al. [172] linked the tetragonal distortion along the **c** axis to the concentration of Li. Above $x = 0.08$, they observed that the tetragonal distortion of the **c** lattice parameter diminishes so that the ratio of $\mathbf{c}/2\mathbf{a}$ is close to 1, allowing the formation of domains with a 90° orientation that preserve the anionic network.

In addition to the tetragonal cell, the literature also describes various cubic and orthorhombic cells. The simplest system is cubic, containing only one perovskite cell and therefore a completely random distribution of Li, La and vacancies. The system was observed by Harada et al. [21] to occur for particular values of x and has also been observed for samples that are quenched from high temperatures [167]. Quenching achieves the simple cubic system as above 800°C the La ions are mobile and above 1200°C they are completely disordered for all values of x [173].

A larger orthorhombic system was proposed by Inaguma et al. for $Li_{0.16}La_{0.61}TiO_{3.01}$ which contained a $2\times2\times2$ arrangement of perovskite cells [174]. They carried out a refinement on neutron diffraction data which showed additional peaks, some of which were later confirmed to be very weak, but present, in their X-ray diffraction data. They associated the structure with distortion and tilting of the TiO_6 octahedra, which restricted their choice of space group to Cmmm or Cm2m. The first of these has higher symmetry and therefore was adopted for their study. They conclude that the expansion of the cell along the three vectors is caused by tilting along the **b** axis, alternatively arranged La along the **c** axis and Li in two equivalent off-centre positions.

They further suggest that the ionic conduction occurs two dimensionally due to the structural features.

The diffusion behaviour has been investigated using conductivity spectroscopy as the frequency dependence of the technique allows the separation of the signal into diffusion rates in the bulk, grain boundary and at the electrode surface [175]. Deviations from a strict Arrhenius diffusion relation are observed over the temperature range of $150\,\mathrm{K} - 600\,\mathrm{K}$ which are attributed to different pathways becoming active with increasing temperature. Observations are made that the tilting of the TiO_6 is enhanced in the **ab** plane in comparison to the **c** direction, allowing Li diffusion at lower temperatures. Further study by the same group measured activation energies of 0.33, 0.33 and 0.34 eV for x values of 0.08, 0.1 and 0.12, respectively, in a low temperature regime up to 400K. It was expected that the energy corresponds to Li motions from cage to cage. At higher temperatures the activation energies lowered to 0.19, 0.21, and 0.13 eV, which is explained by a second frequency diffusion process becoming active [176].

To obtain an improved idea of the processes by which Li ions move around in the sample and the extent to which the tilting of the O ions affects the process, it is necessary to carry out computational simulations of the system. Mori et al. [177] have modelled neutron powder diffraction data using Reverse Monte Carlo. They identify three different types of Oxygen bottlenecks through which Li ions must pass to migrate between perovskite cages. Using the bond valence sum approach the most numerous type of bottleneck is determined to also be the most beneficial to diffusion.

Recently Molecular Dynamics simulations have provided a more in depth description of Li diffusion. As well as predicting an optimal x value of 0.067, Chen and Du [178] observed that when Li ions diffuse through the bottlenecks, the bottlenecks expand by 8-10%. The flexibility of the O ions to move from their nominal sites is clearly important for the diffusion which may explain why certain pathways are thermally activated. A different MD study by Jay et al. [179] investigated the link between ordering of La into layers and the conductivity. The optimal level of ordering involved a difference in La concentration of 20% between the two layers. The migration of Li was observed to occur as both isolated events and as concerted chains of motion of several ions.

7.1 X-ray Diffraction

Despite the extensive literature, no single crystal X-ray or neutron diffraction experiments exist. The only diffraction experiment to use a single crystal was analysed as a powder, emphasising the orthorhombic distortion [180]. A true single crystal diffraction study provides additional information by separating the powder lines into distinctive Bragg peaks in 3 dimensional reciprocal space. Their relative intensities can be measured to provide additional information about the level of symmetry in the system.

Efforts were made to grow $Li_{0.29}La_{0.56}TiO_3$ in a single crystal form using a floating zone furnace. The difficulty of the process meant that it was not possible to grow single crystals with dimensions larger than ~ 0.4 mm. Sample crystals were pre-screened to check their quality, which involved looking for distinctive strong peaks and the absence of additional peaks due to secondary crystallites. Three inequivalent crystal structures were identified from the diffraction patterns; an orthorhombic system and a cubic system made up of 2×2×2 simple cubic perovskite unit cells and a large tetragonal cell with a Ruddlesden-Popper (RP) structure.

Diffraction data sets were measured at room temperature over a large volume in reciprocal space, exceeding the minimum volume needed to observe the complete symmetric pattern. CrysalisPro software was used to identify the peaks throughout reciprocal space and index them according to their position and intensity. This information is transferred to JANA2006 which refines the ionic positions to match the diffraction

Cell Size	Peak Refinement					Ion Positions		
	a / Å	**b** / Å	**c** / Å	Symmetry	R_{int}	La Conc.	R(all)	ωR(all)
1×1×1	3.8784	-	-	P-43m	0.046	66.0	3.13	3.92
1×1×2	3.8754	-	7.7635	P4/mmm	0.039	66.3	4.47	5.00
2×2×2	7.7557	-	-	Pm-3m	0.064	57.6	12.75	8.07
2×2×2	7.7531	7.7517	7.7511	Cmmm	0.041	66.3	8.94	6.86
1×1×4	3.845	-	14.786	C2/m	0.243	-	-	-
1×1×7	3.8601	-	26.40	C2/m	0.359	-	-	-

Table 2: Refinement of LLT diffraction peaks according to different multiples of the simple perovskite cell using CrysalisPro. The ionic positions and La concentrations of the top four structures have also been refined using JANA2006.

pattern. A range of symmetries were tested for each system to ensure that the best fit was found. The symmetry constrains the flexibility of the ionic coordinates that could be refined in JANA2006. Less constraint is placed upon the atomic displacement parameters, ADP, which were allowed to vary anharmonically and the La site occupation which was also allowed to vary.

7.1.1 Orthorhombic Cell Refinement

The hk0 plane of the orthorhombic system is shown in Figure 58. There are clear peaks associated with the reciprocal lattice spacings of the simple perovskite unit cell, shown by the grid. In addition there are peaks visible at the half and quarter positions along the grid lines. This suggests the presence of a larger superstructure involving multiple perovskite cells.

Different supercells are described as multiples of the simple perovskite cell as listed

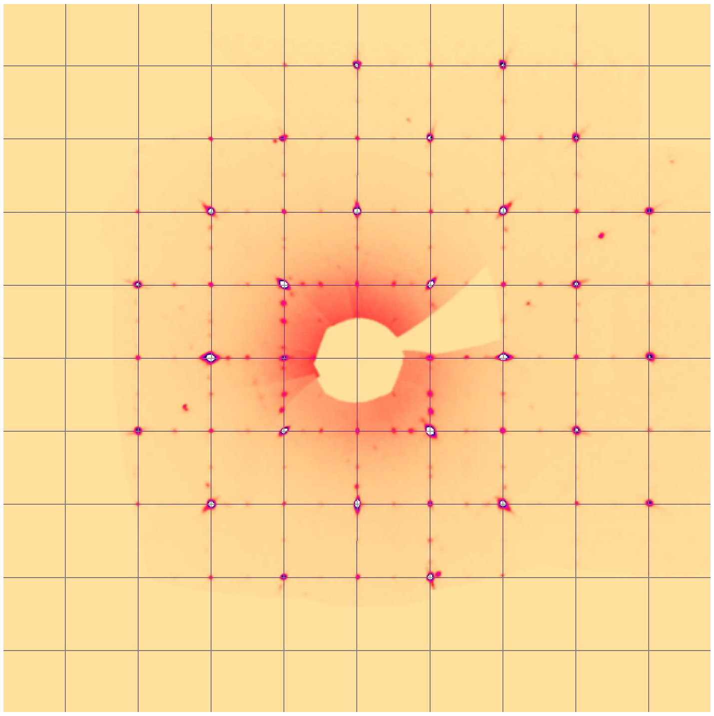

Figure 58: A diffraction pattern in the hk0 plane of the orthorombic cell of LLT.

in the first column of Table 2. Refinements of the lattice parameters and the optimal symmetry are shown along with R_{int} values that provide a measure of the fit. The first four rows have very good levels of R_{int} which is most likely caused by the strong peaks associated with the simple perovskite. The high values for the 1×1×4 cell is most likely caused by weak scattering at large Q values. The 1×1×7 cell was tested for a later comparison with the large tetragonal cell. For the systems with low R_{int} values, attempts were then made to refine the ionic positions.

Using JANA2006, the ions within the cells are refined to provide the best fit to the indexed peaks. The symmetry of the system defines the ways in which ions can move dependent on their Wyckoff position. In addition to this each ion will have its atomic displacement parameters refined to determine how the ions move around their nominal sites. The concentration of the La ion is also refined, which is possible due to its large X-ray scattering cross section. Across three of the structures, a La concentration of approximately 66.2% is refined indicating a low Li content. Orthorhombic cells of $Li_{3x}La_{\frac{2}{3}-x}TiO_3$ have been observed previously for low values of x [174]. It is not possible to refine the Li concentration directly due to its low atomic number which gives a very small scattering cross section. A token 29% occupancy has been fixed on the La sites for all refinements; however this will be almost invisible next to its larger neighbour. This value was used as it is the expected concentration given the synthesis parameters.

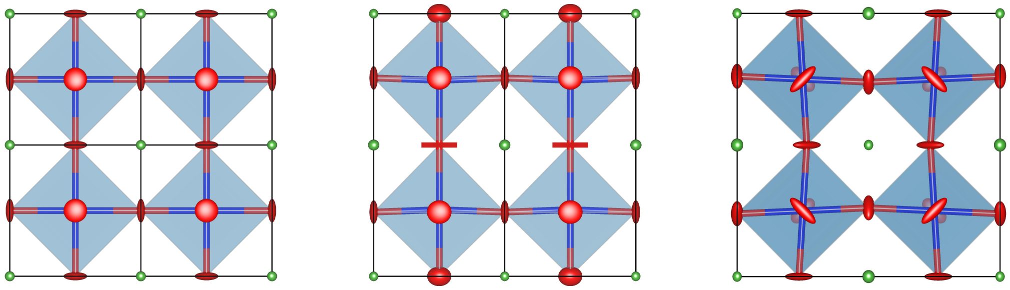

(a) Visualisation of the ADPs of the 1×1×1 refinement.

(b) Visualisation of the ADPs of the 1×1×2 refinement.

(c) Visualisation of the ADPs of the 2×2×2 refinement.

Figure 59: The shape of the ADP parameters are shown centred on their refined positions. The Ti and O are within octahedra with the the O coloured red. The La is coloured green. The smaller 1×1×1 and 1×1×2 are replicated to have the same total volume as the 2×2×2 system. Each unit cell is outlined by a black lines.

JANA2006 only refines the ionic positions according to the peaks that have been indexed for that unit cell, ignoring all other peaks. The 1×1×1 system has low R values showing that the system is approximated quite well by the average structure of the perovskite cell. Although the refinements of the 1×1×2 and 2×2×2 systems have higher R values, they capture a more in depth view of what is happening within the system. Figure 59 shows the refined ionic positions and their ADPs for the 1×1×1, 1×1×2 and 2×2×2 system in their **ac** planes. In the 1×1×1 system the O ions ADPs are flat plates in the plane of the La/Li ions, Figure 59a, while in the 2×2×2 system the O ions has elongated ellipsoid ADPs which are angled towards lower occupancy La sites, Figure 59c. The La ions in each system are shown by the green spheres. The low occupation La sites have larger ADPs comparably with the higher occupation sites.

The ADPs of the 1×1×2 system, Figure 59b, show clear differences based on their proximity to the different La occupation sites. The system shows high occupation at the top and bottom and low occupation in the central La site. Although the general shape is a flat plate for all O ions, similar to the 1×1×1 system, the flatness of the plate is related to its position. A thick plate is observed between high occupation sites while a negligibly thin plate is observed between the low occupation sites, which is why it is represented as a square plate. The O ions between the layers are equivalent in size to those of the 1×1×1.

The flat plate like structure of the ADPs in the 1×1×1 and 1×1×2 systems may come about as a way of trying to model the directionality that is observed in the 2×2×2 system. The directionality is linked to the distortions of the perovskite cells and the La concentrations. The O ions are drawn towards the high occupation La site in the centre of Figure 59c. Comparing the different figures, it is clear that the ADPs of ions in the 2×2×2 system must be averaged out into plates to attempt to describe all the different directions at once, as is necessary in the 1×1×1 system. The R values of the 2×2×2 system may be worse as there is a greater number of parameters, but it may give a better glimpse of the actual make-up of the system.

Comparisons of the cubic and the orthorhombic refinements of the 2×2×2 system

(a) Refinement of a $Li_{0.29}La_yTiO_3$ cell using Pm-3m symmetry.

(b) Refinement of a $Li_{0.29}La_yTiO_3$ cell using Cmmm symmetry.

Figure 60: Refined Ion positions and La concentration for the orthogonal LLT system. The La ions are multi-coloured to make clear their symmetrical partnering while the O, red, and Ti, blue, ions are encapsulated in octahedra.

show distortions of the TiO_6 octahedra, Figure 60. The orthorhombic case has larger distortions of over 0.1 Å. In both systems, the Ti is distorted from its central position. The cubic systems La occupation varies strongly between sites, with the central site almost fully occupied while a low occupation is observed on the corner site and the high symmetry face and edge sites have 66% occupancy. The orthorhombic refinement shows the La mixes into layers of high occupancy, dark green and yellow, and low occupancy, light green and pink, sites with occupancies of 78% and 55% respectively. Due to the symmetry constraints and consequently the Wyckoff positions of the cubic system it is not possible to have alternating layers of La which may explain why the R values are higher.

7.1.2 Cubic Cell Refinement

The second system has a similar diffraction pattern to the first however the peaks at the halfway position are diffuse in appearance suggesting a higher level of disorder. The diffraction pattern of the $\{hk0\}$ plane is shown in Figure 61 with clear strong peaks shown for the simple perovskite cell. The peaks were identified and indexed according to the unit cells listed in Table 3.

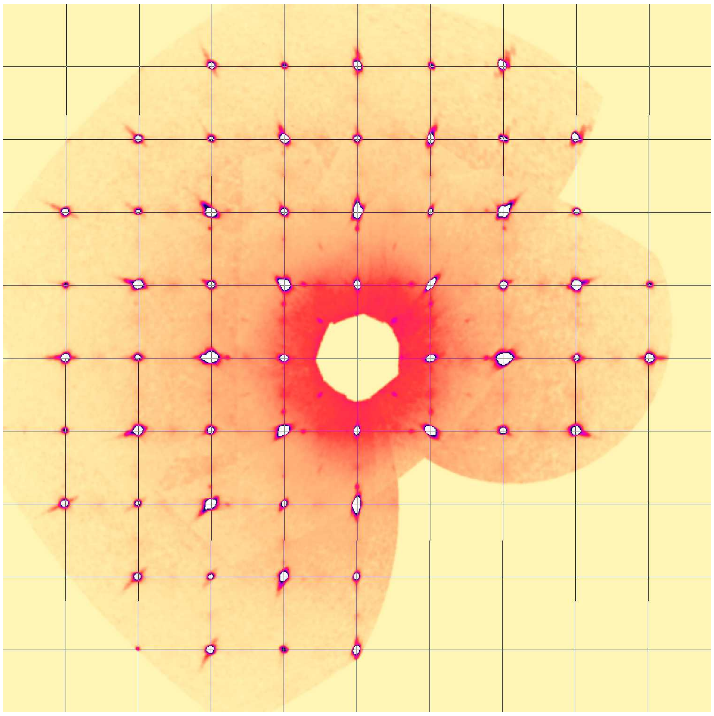

Figure 61: A diffraction pattern in the *hk*0 plane of the cubic cell of LLT.

The refinements of the 1×1×1, the 1×1×2 and 2×2×2 cells give similar values of R_{int} while the 1×1×4 cell gives a value an order of magnitude higher. The value for **c** and 2**a** is consistently at ~7.767 Å regardless of the symmetry. Only the 1×1×4 refinement shows significant deviations which may in part be the cause of its large $\mathrm{R}_{\mathrm{int}}$ value. The first four systems were transferred into JANA2006 to refine the ionic structure. The concentration of the 2×2×2 cells are close to the expected value and are also the only ones that are within the allowed range of $0.5<\mathrm{La}_x<0.666$ which is determined by the amount of electrons.

In comparison to the last structure, the occupation of La is evenly spread across

Cell Size	Peak Refinement					Ion Positions		
	a / Å	**b** / Å	**c** / Å	Symmetry	R_{int}	La Conc.	R(all)	ωR(all)
1×1×1	3.8836	-	-	Pm-3m	0.041	75.7	2.85	3.64
1×1×2	3.8844	-	7.765	P4/mcc	0.036	43.7	5.58	7.09
2×2×2	7.7676	-	-	Fm-3m	0.049	54.4	8.95	9.98
2×2×2	7.7653	7.768	7.7677	Cmmm	0.034	56.5	10.27	9.90
1×1×4	3.900	-	14.552	P4/mmm	0.428	-	-	-

Table 3: Refinement of LLT diffraction peaks according to different multiples of the simple perovskite cell using CrysalisPro. The ionic positions and La concentrations of the top four structures have also been refined using JANA2006.

(a) Refinement of a $Li_{0.29}La_yTiO_3$ cell using Pm-3m symmetry.

(b) Refinement of a $Li_{0.29}La_yTiO_3$ cell using Cmmm symmetry.

Figure 62: Refined Ion positions and La concentration for the cubic LLT system. The La ions are multi-coloured to make clear their symmetrical partnering while the O, red, and Ti, blue, ions are encapsulated in octahedra.

all sites with no variations greater than 1%. Deviations from the predicted structure are also low with the maximum O distortion in both cases being 0.007 Å away from its nominal site. There is almost no difference between the Fm-3m and the Cmmm systems except a slight drop in concentration between the two of 2.2%. In comparison to the refined 1×1×1 system there is a difference of 20% however the positioning of ions is almost exactly the same. The difference between the 2×2×2 and 1×1×1 systems occurs because they contain different lists of indexed peaks due to the size of the reciprocal lattice. The refinements differ in their representations of the atomic displacement parameters, particularly the O ions which are flat circular plates for the 1×1×1 system and spheres for the 2×2×2 systems. The scale of the ADPs for the La and Ti ions also increase from the 1×1×1 to the 2×2×2 system. By not indexing smaller peaks, the 1×1×1 system fits a much simpler cell ignoring the disorder within the system.

The lack of refined distortions in the 2×2×2 systems could be explained by the presence of a single tetragonal crystal with a 1×1×2 tetragonal cell with interlocked 90^{o} domain boundaries. Evidence for such a system has been observed by electron diffraction [181]. By having at least 3 domains of a 1×1×2 tetragonal structure the diffraction pattern would resemble a 2×2×2 cubic system. The ADP parameters will then adjust to mimic the distortions of the tetrahedra in the different domains. In contrast the 1×1×1 refinement would not be able to mimic a two layer system as it cannot predict peaks at halfway positions.

7.1.3 Ruddlesden-Popper Cell Refinement

The diffraction patterns from a large tetragonal cell are shown in Figure 63. The $\{hk0\}$ plane has regularly spaced peaks that correspond to the lattice spacing of the simple perovskite unit cell, see Figure 63a, while in the $\{0kl\}$ planes there are many extra peaks which occur parallel to $\mathbf{c}^*$, however with a spacing ~ 7 times smaller, see Figure 63b. This suggests a larger supercell consisting of 1×1×7 simple perovskite cells.

Attempts were made to refine the diffraction pattern using the smaller 1×1×1 and

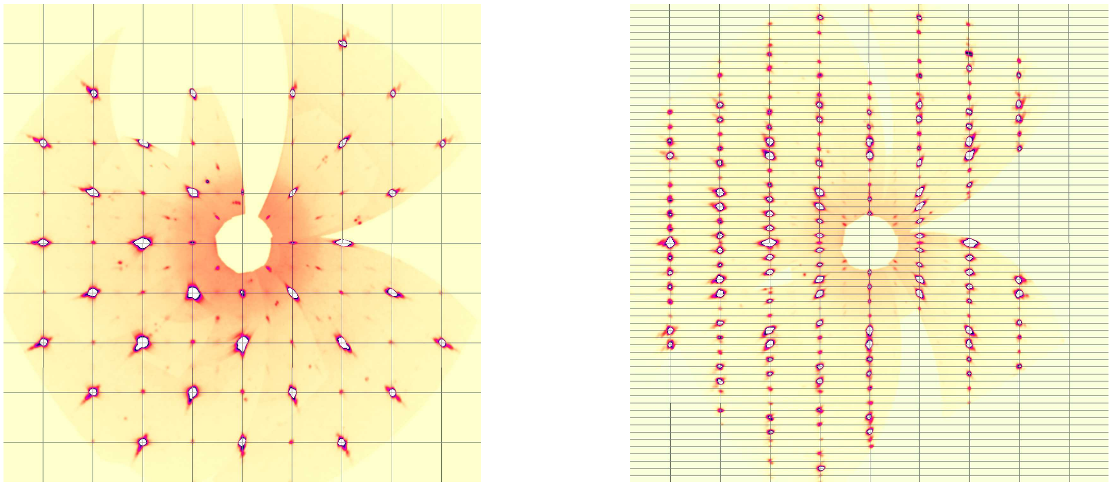

(a) A diffraction pattern in the $hk0$ plane of the tetragonal cell of LLT.

(b) A diffraction pattern in the $0kl$ plane of the tetragonal cell of LLT.

Figure 63: Diffraction patterns in the two inequivalent planes of the RP cell of LLT.

1×1×2 unit cells however only the 1×1×7 cell produced a reasonable R_{int} value, Table 4. The proximity of the peaks to each other, in contrast to the system resolution and mosaic spread, may be responsible for the slightly higher R_{int} value as some peaks are almost overlapping. That the 1×1×1 provides a particularly poor fit shows the strength of these 1×1×7 peaks which are comparable in some cases to the 1×1×1 peaks. A slight increase in the **a** lattice parameters of the tetragonal cell is observed in comparison to the orthorhombic cell. The **c** lattice parameter is refined to be equivalent to $6.8x\mathbf{a}$ lattice parameter. Refinements of the ionic positions carried out using a 1×1×7 arrangement of simple perovskite cells produced poor fits, as is shown by the large R factors in 4.

An alternative ionic structure was proposed and refined by a collaborator [138]. The refinement was based on the Ruddlesden-Popper structure which was first proposed for the related $Sr_3Ti_2O_7$ [182]. The systems contains alternating sets of perovskite cells. A general formula is given for RP phases, written as $A_{n-1}A'_2B_nX_{3n+1}$ where A,A', and B

Cell Size	Peak Refinement					Ion Positions		
	a / Å	**b** / Å	**c** / Å	Symmetry	R_{int}	La Conc.	R(all)	ωR(all)
1×1×1	3.856	-	3.904	P4/mmm	0.380	48.3	24.44	29.63
1×1×2	3.874	-	7.702	Pccm	0.207	51.5	19.00	25.03
1×1×7	3.838	-	26.343	P4/mmm	0.072	38.4	81.22	84.54
RP	3.862	-	26.343	I4/mmm	0.052	64.7	4.21	5.49

Table 4: Refinement of LLT diffraction peaks according to different multiples of the simple perovskite cell using CrysalisPro. The ionic positions and La concentrations of the top four structures have also been refined using JANA2006.

are cations, X is an anion and n is the number of octahedra in each set. Values for n range from 1-3 for stoichiometric samples [183].

The refined RP cell is shown in Figure 64 while parameters are given in Table 4. Greatly improved R factors are achieved using the RP cell. The refined chemical formula is $Li_{1.4}La_2Ti_3O_{10}$ which, for comparison, reduces to a chemical formula of $Li_{0.47}La_{0.67}TiO_{3.3}$ [138]. In contrast to the earlier examined cells, this novel RP cell separates out the Li and La onto distinct sites. The placement of the Li ions within the planes separating the different sets of perovskites cells opens up interesting possibilities for two-dimensional diffusion.

7.2 Calculations

To supplement the diffraction measurements, the arrangements of La and Li ions in the 2×2×2 systems were investigated by calculating the geometry optimised ground states of different starting arrangements of ions using CASTEP. The smaller 1×1×2 system was not studied as it would not be possible to reflect the Li and La concentrations

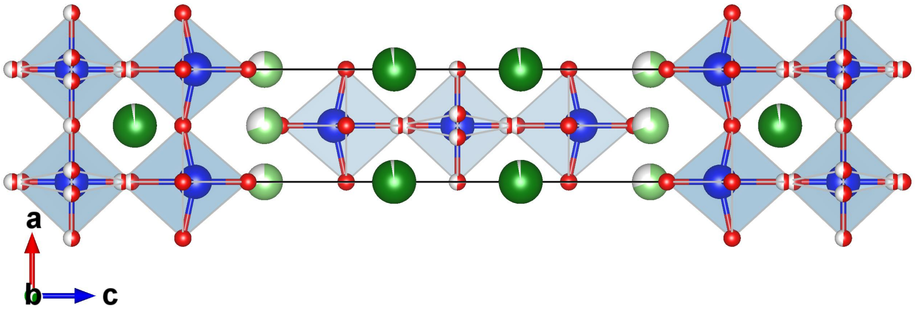

Figure 64: Refined ion positions and La and Li concentrations for the RP LLT system [138]. The La ions are coloured dark green, the Li ions are pale green, while the O, red, and Ti, blue, are encapsulated in octahedra.

using only one unit cell. Other groups have studied larger generic layered systems [179], and it was felt that there was no point replicating their work.

7.2.1 Cubic Cell Ion Ordering

A fully occupied $LaTiO_3$ cubic system containing a 2×2×2 arrangement of basic perovskite cells was geometry optimised to create a template calculation with no site specific biases. The system contained a total of 40 ions, including 8 La, 8 Ti and 24 O ions. A PBE exchange correlation functional was used in combination with the LBFGS method. A high plane wave basis cut-off of 800 eV was used to ensure the rigour of the electron interactions and similarly high convergence tolerances were given for changes in energy, force and position.

With eight La sites in the system it was decided to have 2 Li ions, 5 La ions and one vacancy to achieve close to the nominal concentrations of $Li_{0.29}$ and $La_{0.56}$. A total of 24 arrangements were trialled; the arrangements were constructed based on two layers with a +6 charge in each layer. In the first layer there were 3 La ions and one vacancy while in the second layer there were 2 Li ions and 2 La ions. The trial cells were then individually geometry optimised and analysed to see how the energy of the system depended on the initial and final ionic positions of the system.

A clear relationship is seen of lower ground state energies associated with large distortions of the perovskite cells, Figure 65. The shape of the octahedra, in each geometry optimised system, was analysed according to the scale of the bond lengths and the angle of the bond with respect to the cubic system. For an ideal octahedron, each O ion will line up with one axis of the cubic cell. Canting occurs as the directions of the Ti-O bonds no longer line up with the lattice parameters of the cell.

Figure 65a shows the Ti-O bond lengths versus the ground state energy of each optimised system. In all systems there is some form of distortion from the ideal system resulting in the lengthening and shortening of different bonds. The lowest energies are observed for systems with the widest range of Ti-O bond lengths indicating a large distortion of the octahedra for those systems. Low energy differences, of a few 10's of meV, make it likely that all of these highly distorted systems can co-exist in the real crystal structure which would explain the disorder observed in diffraction patterns. Systems with low distortions have very large energy increases, of > 500 meV, shown in Figure 65a which effectively rules them out as possible ground states.

The association of large distortions with low energy arrangements is further emphasised by Figure 65b which show the canting angle of the O ions away from their ideal position. In the ideal case each Ti-O bond will be parallel to a lattice parameter of the cubic cell. Whereas the Ti-O bond lengths inform about the size of the octahedra, and distortions must be inferred from differences in bond lengths; the canting angle measures any twisting or shifting of the Ti ion away from its central position. The result is the same with large canting angles observed for the lowest energy systems,

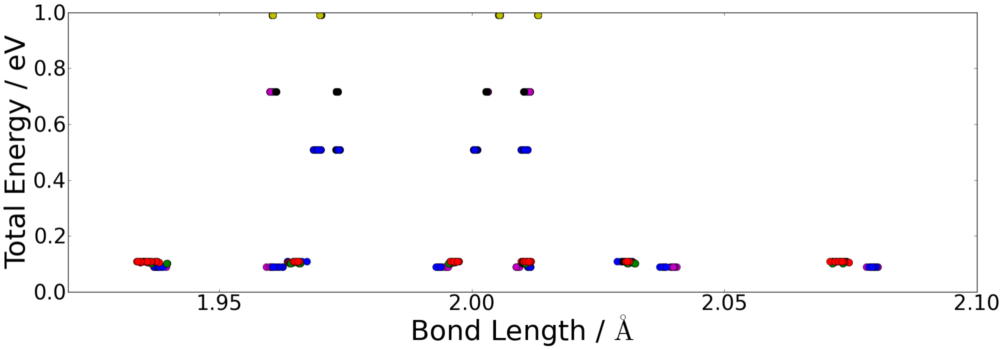

(a) The scale of the Ti-O bond lengths in comparison to the total ground state energy for each geometry optimised LLT cubic system.

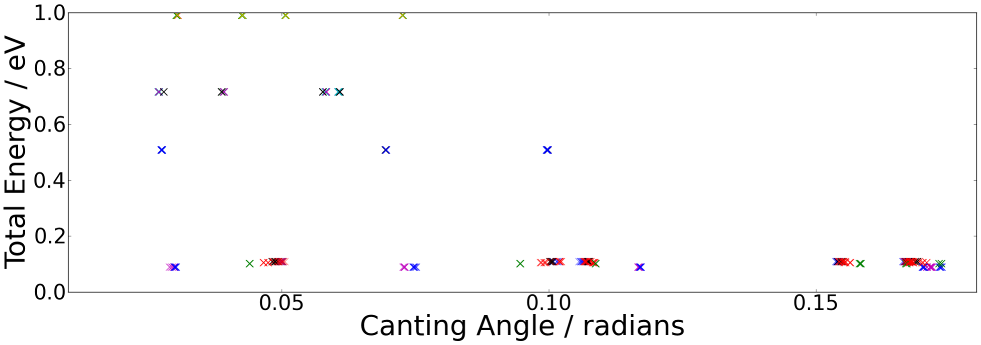

(b) Canting of the O ion away from the ideal octahedra positions displayed in comparison to the total ground state energy for each geometry optimised LLT cubic system.

Figure 65: The profiles of the Ti-O octahedra are analysed in terms of their relative distortions from the ideal octahedron. In each system there are 8 Ti ions surrounded by 6 O each leading to multiple data points for each global system energy. Data points are coloured according to their system.

while small angles are observed for high energy systems.

A visual comparison of the highest and lowest energy geometry optimised systems

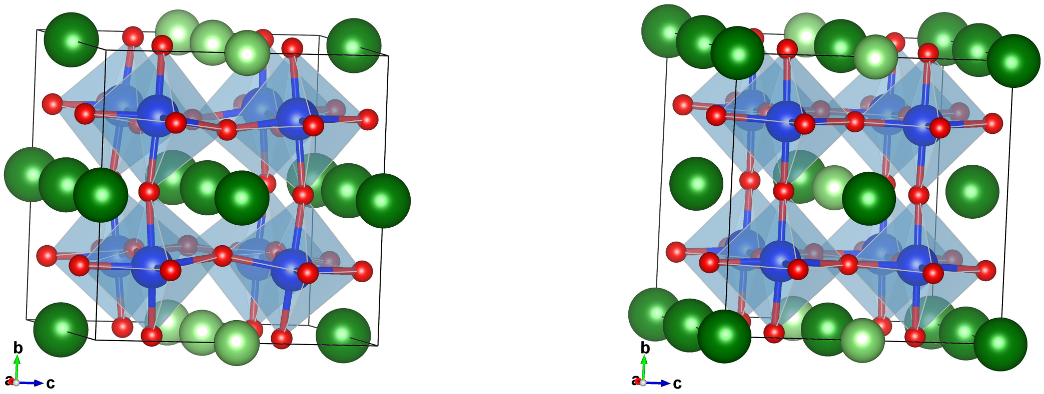

(a) The lowest energy arrangement studied of La and Li ions in the 2×2×2 cell.

(b) The highest energy arrangement studied of La and Li ions in the 2×2×2 cell.

Figure 66: A visual comparison of the lowest and highest energy geometry optimised systems. The La ions are coloured dark green, the smaller Li ions are light green, and octahedra are drawn around the Ti, blue, and O ions, red.

is shown in Figure 66. The octahedra clearly show a large amount of twisting in the low energy case, while in the high energy case they are almost in their ideal positions. The main difference between the high and low energy geometry optimised systems is that in the low energy system the Li ions are neighbours and there is a fully occupied La layer. The direction of the twisting of the octahedra appears to be towards the fully occupied La layer in the centre, where there is a Li ion nearby, and away from the fully occupied layer on the edges, where the neighbours are La ions. The neighbouring Li ions cause this distortion to continue in the next octahedra forming a channel through the structure. In the high energy system channels don't form as the next ion after a Li or a vacancy in any direction is always a La.

7.3 QENS

The fast rate of Li ion diffusion in $Li_{0.29}La_{0.56}TiO_3$ makes it an interesting candidate to study using QENS. By studying the temperature dependence of the average residence time between hoping motions, the diffusion rate in the bulk material is obtained. The rate can be compared to other methods, such as conductivity spectroscopy [176], to establish the connection between bulk electrochemical measurements and diffusion on the atomic scale. The measurement will also look for the presence and scale of any change in diffusion behaviour away from a strict Arrhenius increase. Changes from 2D to 3D diffusion have been reported between 200 K and 400 K [20].

7.3.1 Experimental Setup

As there is some ambiguity about the temperature of a change in the diffusion behaviour, it was decided to use as low a temperature as possible to measure the resolution-limited function, to ensure there is no visible Lorentzian broadening. From this base temperature of 10 K, measurements were made every 100 K up to 700 K. Prior to any measurements the sample was heated to 400 K while the atmosphere was pumped out as a precaution to remove any residual moisture in the cell.

A pulse tube top loading cryostat was used for the experiment to allow a large temperature range from 10 K to 780 K, which covers a large portion of the dynamic range of the sample without needing to switch to a furnace. The advantage is that the background from the sample environment remains the same for all measurements. The 15 g powder sample was contained in a cylinder made of Niobium instead of Aluminium as it has a higher melting point. It does have a slightly increased coherent scattering cross section although the incoherent cross section is reduced, as shown in Table 5.

To improve the signal to noise ratio of the powder sample, an enriched isotope of Ti

Isotope	b_{coh} (fm)	b_{inc} (fm)	xs_{coh} (barn)	xs_{inc} (barn)	xs_{scat} (barn)	xs_{abs}/ barn
Li	-1.9		0.454	0.92	1.37	70.9
La	8.24		8.53	1.13	9.66	8.97
Ti	-3.438		1.485	2.87	4.35	6.09
O	5.803		4.232	0.0008	4.232	0.00019
Nb	7.054	-0.139	6.253	0.0024	6.255	1.15
Al	3.449	0.256	1.495	0.0082	1.503	0.231
H	-3.7390		1.7568	80.26	82.02	0.3326

Table 5: Relevant neutron scattering lengths and cross sections for LLT, as reported in [58]. The columns are, from left to right: bound coherent scattering length, bound incoherent scattering length, bound coherent cross-section, bound incoherent cross-section, total bound scattering cross section and absorption cross-section. The absorption cross-section is given for neutrons at 2200 m/s.

was used to lessen its incoherent scattering contribution. By changing to a 95% enriched ^{48}Ti the incoherent scattering cross section dropped from 2.87 to 0.144 barns. Unfortunately La has a significant incoherent cross section and was too expensive to enrich. With a La cross section of 1.13 barns and a Li cross section of 0.92 barns, the proportion of incoherent scattering from Li, from a sample composition of $Li_{0.29}La_{0.56}TiO_3$, is 25.6% which is slightly larger than in the $Na_{0.8}CoO_2$ experiment.

Using OSIRIS' diffractometer, the total scattering from the powder sample was measured, Figure 67. It covered most of the Q range significant to the spectroscopy detectors, but not the lowest Q values. The Bragg powder lines interfere with the background and consequently the QENS signal and therefore these regions are usually avoided. The diffraction data is shown in black with the fitted pattern shown by open red circles. It is clear that above 2.2 Å there is a large concentration of peaks. Spectroscopy measurements therefore used the PG(002) analyser as this has a Q range from 0.18 to 1.8 Å.

The fitting was carried out using the crystal structures of the background materials Al and Nb, as well as the RP-phase LLT and the 1×1×2 LLT structures by Dan Porter [138]. It was determined that the scattered proportions from each sample were 10.7%, 2.3%, 9.8%, and 77.2% for the Al, Nb, RP-phase and 1×1×2-phase structures, respectively. The lack of a [110] peak in the 2×2×2 system, which is predicted at 1.15Å, indicates that the correct structure of the majority of the powder is the tetragonal 1×1×2 cell and not the 2×2×2 cell which accounts for no additional peaks in the measurement.

Additionally, scattering from the container and the Aluminium heat shields is limited to high Q so will not be a factor if the PG(002) analyser is used. The distance of the heat shields from the centre of the sample leads to a splitting of the peaks due to differing path lengths of neutrons interacting with the front and back walls. This may

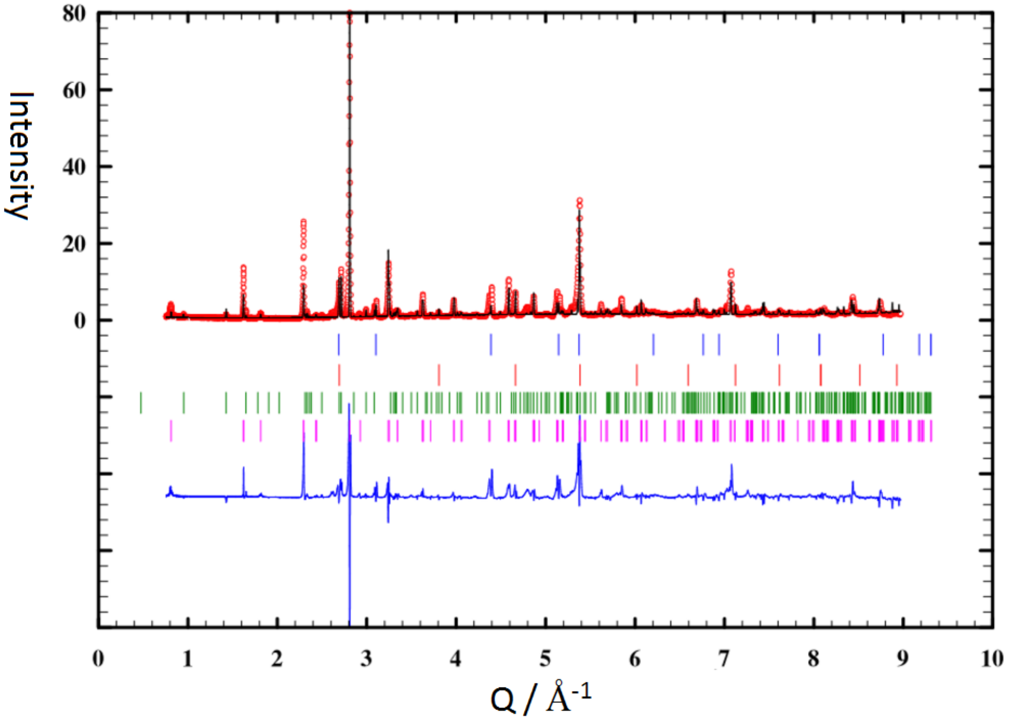

Figure 67: Neutron powder diffraction pattern of the 15 g $Li_{0.29}La_{0.56}TiO_3$ sample measured using the OSIRIS diffractometer bank. The powder data (black) is fitted (red) using the crystal structures of Al (blue), Nb (red), the LLT RP-phase (green) and the LLT 1×1×2 phase (magenta) [138]. The difference between the powder and fitted patterns is shown by the final blue line.

lead to the, sometimes large, differences observed between the experimental and fitted patterns. Another cause could be the presence of small impurities, such as La_2O_3, that occur during the growth process.

7.3.2 Intensity Analysis

The reduction of the data is carried out in the same way as the $Na_{0.8}CoO_2$ experiment using the MANTID software package. The energy transfer profiles of all the temperature data sets are calculated from the time of events occurring at each detector. The data is reduced according to time and Q bins. For gross measurements of the shape of the profiles large Q bins were used which effectively grouped 21 detectors together. For later data analysis this is reduced to groups of two detectors to allow a Q dependence to be resolved. The width of the time bins is fixed so that it is equivalent to 4μeV. The data is normalised by a vanadium scan to account for detector efficiency.

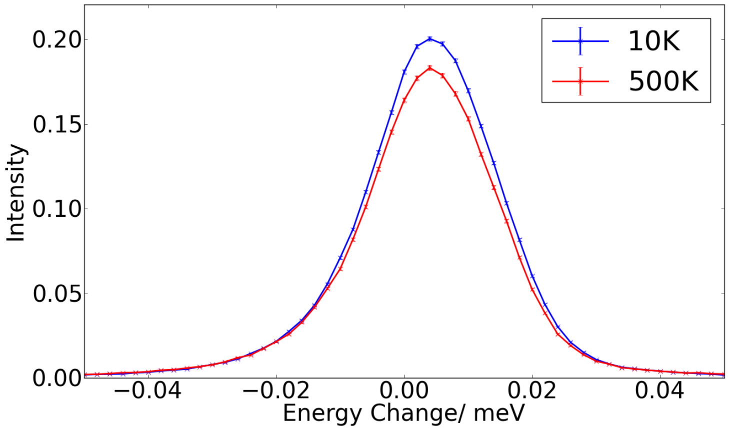

Figure 68: Comparison of the energy lineshape of the 10 K resolution limited function and a 500 K high temperature data set. The data is averaged in both cases over a range of Q centred on 1.27 $\AA^{-1}$.

A comparison of the energy transfer profiles of the base temperature, resolution limited, 10 K data and a high temperature, dynamic, 500 K data set is shown in Figure 68. A clear drop in intensity is observed between the two measurements in the elastic peak. The change in peak shape between the low and high temperature measurements leads to the relative increase in intensity in the wings of the profile. Further analysis of the data at all temperatures is carried out by isolating elastic, quasi-elastic and background regions and measuring their relative intensities.

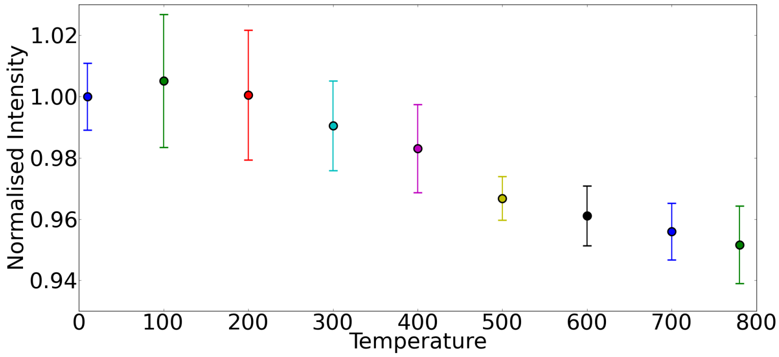

Figure 69: The intensity of the elastic region of the energy lineshape for each temperature data set measured with the LLT powder sample.

The intensity of the elastic region at each temperature is shown in Figure 69. At low temperatures, beneath 300 K very little changes which indicate that the diffusion at these temperatures is either too slow with respect to the resolution of the analyser or is not thermally activated yet. From 300 K a steady decrease in the intensity is observed with a total drop of 5% recorded between highest and lowest temperatures.

The relative counting times at each temperature can be inferred from the scale of the error bars of Figure 69. Only 6 hours of experimental time were invested in the measurements at 100 K and 200 K as the changes in profile were predicted to be limited in comparison to the 10 K data set. At 10 K and initially at high temperatures, measurements were undertaken for 12 hours as the whole experiment depended upon a good approximation of the resolution limited function and the highest diffusion rates were expected at higher temperatures. Extra measurements were carried out at 500 K to improve the errors in this data set. At 300 K and 400 K the measurements ran for 6 hours as it was considered less important to measure here. At 780 K, a reduced data set of 6 hours was also recorded due to a lack of experiment time.

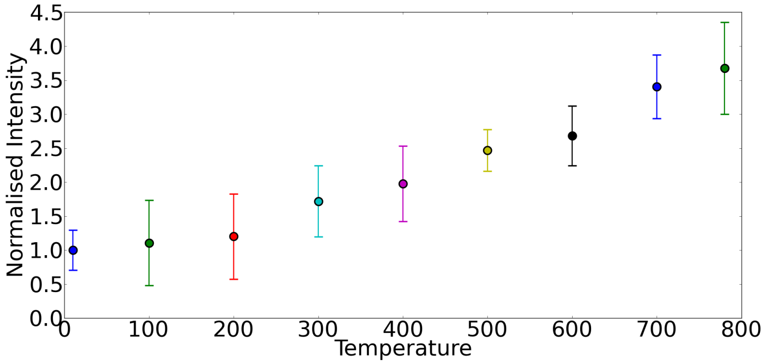

Figure 70: The intensity of the background region of the energy lineshape for each temperature data set measured with the LLT powder sample.

The background level increases by a factor of 4 between 10 K and 780 K, although the absolute level is pretty small in comparison to the intensity in the QE wings and at the peak. At 780 K where the ratio of the maximum elastic intensity over the background intensity is smallest, the maximum elastic intensity is still 1000x larger. Nevertheless the background level has been subtracted from the QENS region so that it does not bias the temperature progression.

With the background subtracted almost no intensity changes in the quasi-elastic region are observed until 300 K, Figure 71. At this temperature a large step increase is observed which then continues up until 600 K. A slight increase in the intensity is observed for the 700 K and 680 K measurements however the change is well within the errorbars. This could suggests a limit to the diffusion rate or the experimental

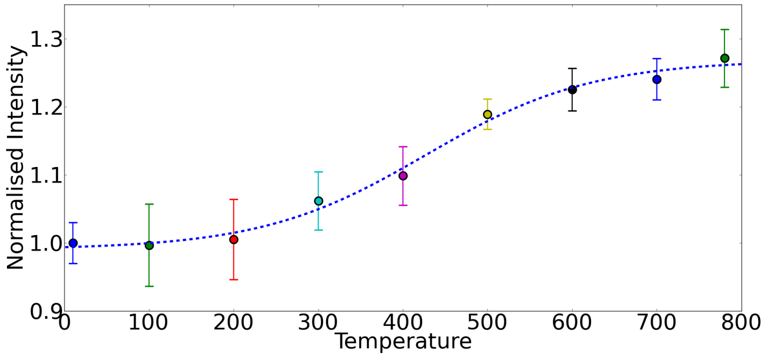

Figure 71: The quasi-elastic intensity of the energy lineshape for each temperature data set measured with the LLT powder sample. It has been fitted with a sigmoid function to help visualise the progression with temperature.

equipment and its ability to measure QENS. Returning to the background measurement, it appears that a small step increase in intensity is observed at 700 K which could indicate that the quasi elastic intensity has flattened into the background.

7.3.3 Q Dependence

As with the $Na_{0.8}CoO_2$ sample, the low level of broadening requires certain parameters to be fixed. In this case the hop length has been fixed at 3.875 Åwhich corresponds to the distance between the different Li/La sites. The ratio of static to dynamic incoherent scattering has also been fixed at 25.6%, determined by the respective ratio of Li to La in the system.

Unfortunately phonon scattering occurring close to the Q positions of the Bragg lines has added an unwanted background, as shown in Figure 72. The additional intensity at non zero energy transfer makes it difficult to measure the resolution as there is no longer a regular shape that can simply be scaled to fit any higher temperature

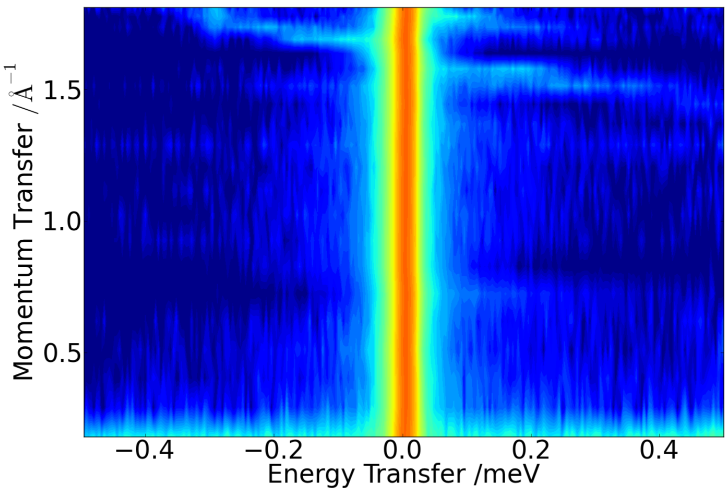

Figure 72: A colour map of the neutron scattering flux in terms of detector and energy transfer for the 10K dataset. At high Q there are phonons observed which create an additional background signal. Blue indicates a low intensity while red indicates a high intensity. The detectors are evenly spaced from 11^{o} to 148^{o} which corresponds to a Q range of 0.18-1.8$\AA^{-1}$.

non-dynamic system. This hinders the fitting of quasi-elastic broadening at higher temperatures as the convolution can no longer be carried out without separately modelling and subtracting the phonon scattering. For this reason, the detectors above 1.4 Å have been ignored. The first three detectors have also been ignored as there is considerable scattering from the straight through beam.

The fit of each energy lineshape consisted of three parts; a background level, a static resolution function modelled on the 10 K data set and a dynamic Quasi-Elastic function consisting of a Lorentzian convolved with the resolution function. The width of the Lorentzian and the background level were allowed to vary at each detector grouping. The detectors were paired and the data rebinned into 4 μeV sections over a total range of ± 0.5 meV.

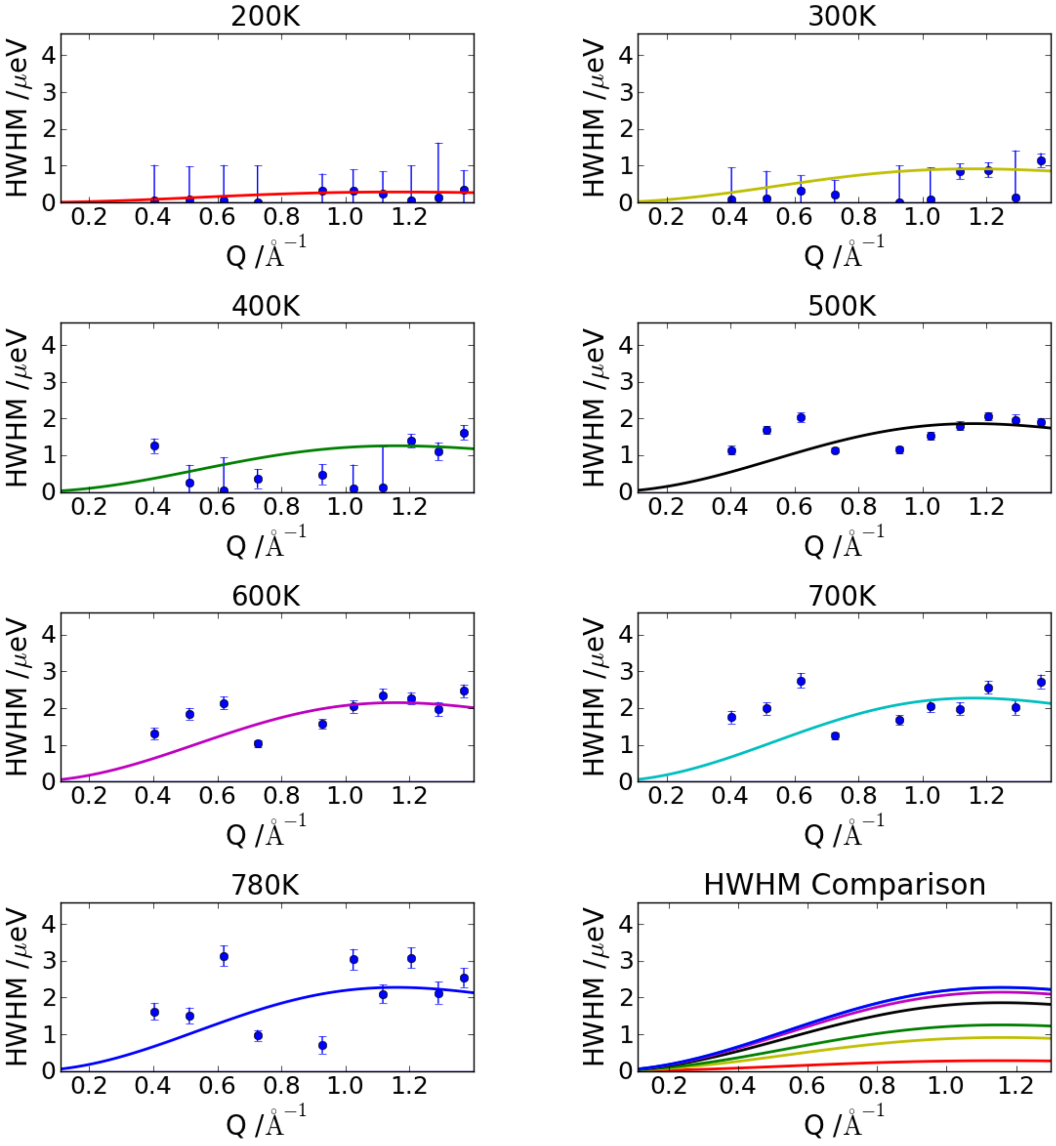

Figure 73: The Lorentzian fitting of the quasi-elastic broadening at each Q value is shown for each temperature data set. The fitted widths are shown by blue markers with the Q position then modelled by a line according to the Chudley-Elliot model. The fitted lines are compared in the final graph with the colour of the line matching the respective temperature.

The fitted Lorentzian widths of each detector grouping are shown in separate graphs for all temperatures in Figure 73. At 200 K the system appears to be almost static. In comparison to the 10 K measurement, the level of broadening of any Q position is no greater than one standard deviation of the Lorentzian widths fit. At 300 K increases in some of the Lorentzian widths are observed, with the errors small enough to separate them from the 0 value. At higher temperatures, the scale of the Lorentzian fit increases further although it is in some ways erratic. From 500 K, there is greater stability in the fitting making it easier to visually see a progression with Q.

An apparent early increase in width is observed for the first three data points shown. If the Lorentzian width were to peak twice over this short Q range, it would correspond to a hop of ~ 9 Å which is clearly unfeasible given the perovskite structure. Despite this there is a clear consistent increase in the level of quasi-elastic broadening with temperature, as shown by the HWHM comparison. The progression of the broadening with Q is modelled using the Chudley-Elliot model. This allows the fitting of a time parameter at each temperature, indicating the average residence time of Li ions in one site between hops.

7.3.4 Diffusion Rate

The average residence times are plotted as a function of temperature in Figure 74. A clear exponential decay is observed with measured mean residence times of the order of hundreds of picoseconds. The exception is at low temperature as the mean residence time at 200 K is an order of magnitude higher. The time parameters are converted to the Arrhenius diffusion rate to allow easier comparison with other methods.

Calculating the Arrhenius diffusion requires converting from the mean residence time to a diffusion rate by making use of the hop distance which was fixed at 3.875 Å.

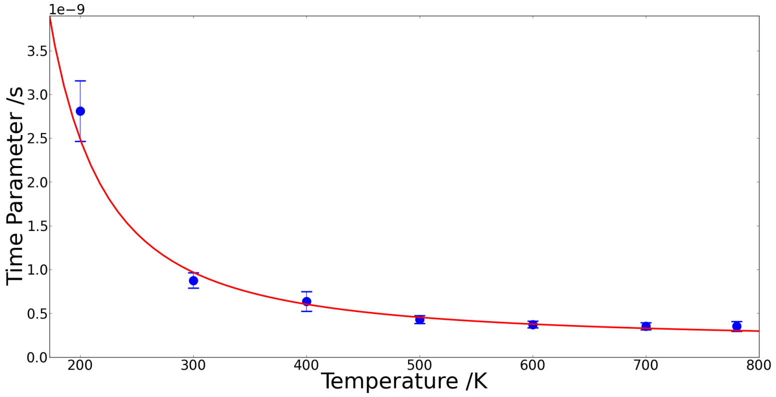

Figure 74: The average site residence times of Li ions between hops for temperatures from 300 K.

Considering the layered structure inferred from the diffraction pattern, the diffusion is expected to be two dimensional. A logarithm of the diffusion rates versus one over temperature is plotted, Figure 75, and a straight line is fitted to establish an activation energy and a diffusion constant. The diffusion constant and the activation energy can be used to calculate the diffusion rate at any temperature.

Over the range from 200 K to 780 K a straight line, red, has been fitted with a diffusion constant of $1.7(2) \times 10^{-6}\,\mathrm{cm}^2\,\mathrm{s}^{-1}$ and an activation energy of $49(3)\,\mathrm{meV}$. This gives a Li diffusion rate at room temperature of $2.6(4) \times 10^{-7}\,\mathrm{cm}^2\,\mathrm{s}^{-1}$. Although no clear diversion from the Arrhenius diffusion is visible in this graph it may be that the resolution of the instrument is not great enough to determine the change given the size of the error bars. At high temperatures it does appear that the experimental data points plateau.

It has been suggested by Bohnke et al. [163] that non-Arrhenius measurements of LLT can be explained by modelling using a Vogel-Tamman-Fulcher type relationship. They state that VTF behaviour accounts for a thermally assisted mechanism of con-

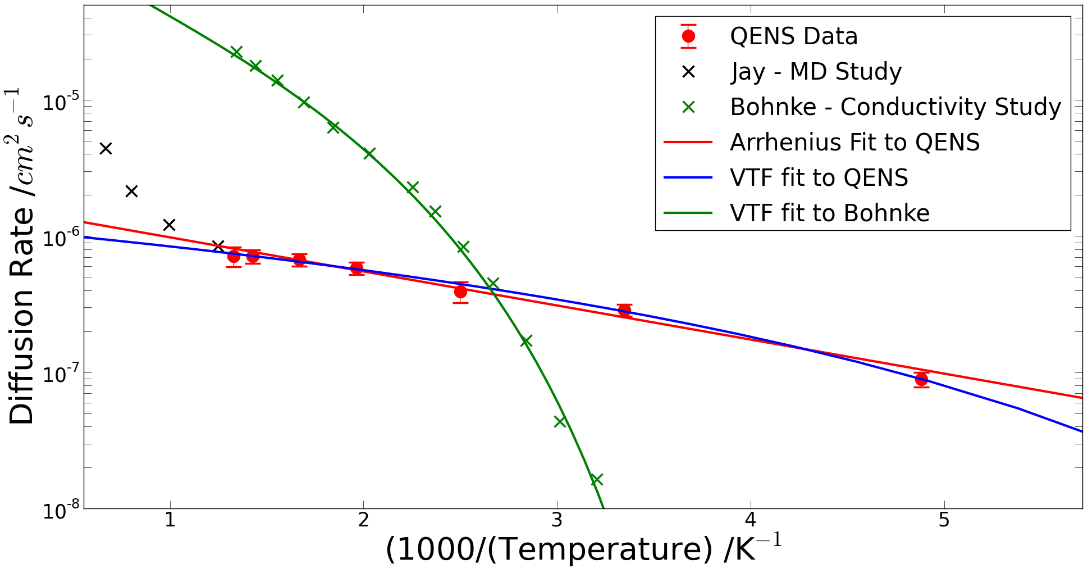

Figure 75: The Arrhenius diffusion rate calculated for LLT from 200K to 780K. The red line fits an Arrhenius dependence while the blue line is a fit using a Vogel-Tamman-Fulcher type relationship. The experimental conductivity measurements of Bohnke et al. [163] has also been added as green crosses with a line marking a temperature dependence according to the VTF formula. Diffusion rates from MD simulations by Jay et al. [179] at four different temperatures are shown as black crosses.

duction dependent upon the opening and closing of bottlenecks between the O of the octahedra. The calculation of the diffusion rate is changed by inserting a temperature offset, T_0 so that Eq. (8) becomes:

$$D(T) = D_0 exp\Big(\frac{-E_a'}{k_b(T - T_0)}\Big), \qquad (56)$$

where T_0 marks the temperature at which the VTF behaviour becomes apparent and E_a' is a pseudo-activation energy. Their experimental conductivity measurements, of a $Li_{0.21}La_{0.60}TiO_3$ sample, have been converted to diffusion coefficients and added to

Figure 75. The VTF line uses an activation energy of 75 meV and a temperature offset of 210 K. This is consistent with other experiments which show changes in diffusion behaviour between 200 K and 400 K [20].

To relate the ensemble transport mechanisms, given by the ionic conductivity, with the motions of individual ions, given by diffusion rates, it is necessary to use the Nernst-Einstein equation, discussed in Section 1.2.4:

$$\frac{\sigma}{D} = \frac{nq^2}{k_b T} f_{\mathrm{NE}}, \tag{57}$$

where n is the number density of ionic charge carriers, q is their charge and f_{NE} is the Nernst-Einstein factor which deviates from unity when ionic motion is correlated [52]. The difference in Li and La concentration in these experiments makes a rigorous comparison difficult. For the purpose of converting the measurement of Bohnke et al. [163] to a diffusion rate, a factor of $f_{\mathrm{NE}} = 1$ was used. Implicitly, this assumes that the motions in the Bohnke system are highly correlated. This would therefore be expected to underestimate the diffusion coefficient as there will be some level of uncorrelated motion which is not detected in conductivity experiments.

Only at values around 400 K is a reasonable level of agreement observed between the QENS diffusion rates and the converted rates of Bohnke. At higher temperatures an order of magnitude difference is observed while at lower temperatures the two measurements diverge rapidly. In silver iodide, Morgan and Madden [52] observe for stoichiometric systems that f_{NE} decreases exponentially from high temperature values where it is close to 1. The Nernst-Einstein factor heads to zero in structures where short closed chains of hops occur. The discrepancy occurs because although diffusion events occur, there is no long range ionic movement.

In the $Li_{0.29}La_{0.56}TiO_3$ the availability of channels with temperature may effectively shift the diffusion of ions from a closed to an open chain system. Evidence of non-

Arrhenius behaviour associated with the opening of new channels at elevated temperatures has been reported previously [175]. This is not inconsistent with the behaviour that the VTF formalism attempts to model.

7.4 Discussion

The structure and diffusion mechanisms of $Li_{0.29}La_{0.56}TiO_3$ have been investigated through diffraction, simulation and QENS measurements. The structures of several diffraction patterns have been investigated and compared to the literature.

A novel tetragonal structure has been examined and corresponds to a RP perovskite-like unit cell. The RP system refines to have an interesting structure with clear planes for two-dimensional diffusion of Li. The concentrations of Li and La are higher than expected, compared to the optimal growth concentration of $Li_{0.29}La_{0.56}TiO_3$. However, the separation into distinct Li and La sites means that there are more vacancies available for Li diffusion.

The other structures observed from X-ray scattering have coincided with 2×2×2 arrangement of pervoskite cells. Previous literature has observed the phenomenon of domains interlocked at 90° in the previously reported 1×1×2 system. The single crystal diffraction pattern would not be able to easily distinguish between these scenarios. Refinements of the ionic positions and also simulations of the structure have favoured a layered structure of La ions. The lowest energy simulations have completely filled La layers and then layers with Li and vacancies and one La ion. Several arrangements of the lower layer have similar energies suggesting that they can coexist together. Long range diffusive motions are also more likely if there is only a small energy difference between the different perovskite cells as then all hops are similarly likely.

The powder sample was specially synthesised for the QENS measurement using a

95% isotopically pure form of ^{48}Ti, increasing the relative contribution of incoherent scattering from Li. A layered 1×1×2 system was identified as being the dominant structure although contamination from RP crystallites was also observed.

Using a fixed hop length, determined by the distance between Li/La sites, a diffusion constant of $1.7(2) \times 10^{-6}\,\mathrm{cm^2\,s^{-1}}$ and an activation energy of $49(3)\,\mathrm{meV}$ were calculated. In comparison to literature the activation energy is around a third lower than reported previously [162, 179]. Lower activation energies have been calculated by Bohnke et al. [163] and Ivanov-Schitz et al. [22] when they used a Vogel-Tamman-Fulcher type relationship which accounts for a thermally activated diffusion mechanism. This VTF relationship is disputed by Rivera et al. [184] who state the diffusion coefficients predicted do not correctly model their low temperature measurements.

At room temperatures, using a Nernst-Einstein factor of 1, the conductivity derived from the QENS diffusion rate is $3.0(3) \times 10^{-3}\,\mathrm{S\,cm^{-1}}$ which is an equivalent order of magnitude to rates observed experimentally using electrochemical methods [162, 185, 177]. Further agreement is seen when comparing to computational studies. A MD study by Katsumata et al. [186] of $Li_{0.2}La_{0.6}TiO_3$ using a partially ionic model to describe interactions, predicted a diffusion rate of $\sim 10^{-7}\,\mathrm{cm^2\,s^{-1}}$ at 500K. Later studies by the same group calculated that Li diffusion gets as high as $1.11 \times 10^{-6}\,\mathrm{cm^2\,s^{-1}}$ at temperatures up to 1000K [187].

Conductivities have been presented by Jay et al. for high temperatures between 600K and 1000K [179], presented in Figure 75. They calculated values between $10^{-1}\,\mathrm{S\,cm^{-1}}$ and $10^{-3}\,\mathrm{S\,cm^{-1}}$ dependent on the structure and La layering. They observe an increase in conductivity between randomly layered and alternating rich-poor layered structures which is an order of magnitude larger when combined with special potentials. This further adds to the consensus that layering is important in enhancing the diffusion rate and conductivities.

The difference in the activation energy between the QENS measurement and other bulk measurements could be caused by the limited temperature baseline of this experiment. Although measurements were made over a wide range of temperatures, beneath 300K the low levels of QE broadening meant that the fitted Lorentzian widths had error bars that were overlapping the zero line. An effective estimate of the activation energy requires a large temperature baseline and although the fit is very good at high temperature, that only comprises a small range. The reported onset of a second diffusion rate may also confuse matters. A change in diffusion behaviour, caused by the thermal activation of new channels, would alter the observed QE broadening away from the Arrhenius fit.

In comparison to the $Na_{0.8}CoO_2$ experiment the diffusion rate is slightly faster despite a longer average residence time. For comparison the experimentally determined residence time at 500K for $Li_{0.29}La_{0.56}TiO_3$ is 430(50) ps while for $Na_{0.8}CoO_2$ it is 93(6) ps. The faster diffusion rate comes from the longer hop length in the $Li_{0.29}La_{0.56}TiO_3$ which is controlled by the perovskite structure. The channelling of ions between different pervoskite cells enhances the diffusion rate making this structure an interesting fast ionic conductor.

8 Conclusions and Future Outlook

The experiments in this thesis aimed to understand diffusion within certain crystalline materials, to advance the development of battery technology by identifying favourable processes for the next generation of materials. The cathode material Na_xCoO_2 and solid-state electrolyte $Li_{3x}La_{2/3-x}TiO_3$ are ideal candidate materials for study.

The similarity of Na_xCoO_2 to the market dominating Li_xCoO_2 coupled to its interesting range of concentration and temperature dependent superstructures provided an opportunity to examine the relation of ionic diffusion with the short and long range ordering of Na ions.

QENS measurements allowed the diffusion rate of Na ion in $Na_{0.8}CoO_2$ to be experimentally determined over a temperature range encompassing all three phases of the composition. The diffusion behaviour is interpreted based upon the fitted activation energies and mean residence time for hopping processes. NMR experiments [129] have shown that the Na ions are super-ionic above 280 K, which corresponds to the sodium reordering phase change from the low temperature ordered stripe phase to the medium temperature disordered stripe phase [128]. No significant changes to the energy lineshape were observed within the temperature range of the ordered stripe phase, suggesting that there is no super-ionic motion of Na ions, in agreement with the NMR measurements. Above the transition into the disordered phase the energy lineshape changes in a manner consistent with the presence of quasi-elastic energy broadening, indicative of translational ionic hop motions.

Reverse Monte Carlo simulations of X-ray scattering patterns of $Na_{0.8}CoO_2$ in the low temperature phase have resolved repeating stripes of tri-vacancy clusters. Coherence between tri-vacancies in different stripes is lost in the disordered stripe phase. We have shown in MD simulations that tri-vacancy clusters are able to translate along stripes via a series of Na1 to Na2 site hops, even when there is an ideal superstructure. These results are consistent with the Fourier difference maps from powder neutron diffraction data, which suggest hops in one dimension [131]. The MD show that for the precise stoichiometry x=0.8 a significant proportion of hop motions do not contribute towards long range diffusion. PITT measurements, by Shu and Chou [41], over a range of Na concentrations have shown that at the precise concentrations corresponding to particular superstructures there are large reductions in the diffusion rates. Fully ordered structures are detrimental to the bulk diffusion rate, promoting ionic motions in closed loops. Non-stoichiometric $\mathrm{Na_{0.8}CoO_2}$ systems have been studied using MD simulations by introducing additional vacancies. If the vacancies are in the vicinity of the stripes, this leads to a large increase in diffusive motions parallel to the stripe. The diffusion rate at T = 300 K determined via QENS has a value of $6.5(8) \times 10^{-8}\,\mathrm{cm^2\,s^{-1}}$, which is reasonably consistent with the bulk diffusion rate for $x > 0.5$ determined using PITT measurements of $D_{\mathrm{Na}}^{\mathrm{PITT}} = 1.2(5) \times 10^{-7}\,\mathrm{cm^2\,s^{-1}}$ [41].

The role of clusters to enhance the diffusion rate has also been studied by MD simulations in the disordered phase. Two separate simulations were created with clusters in one and isolated vacancies in the other. The simulations ran for the same time, and only in the system with clusters were significant numbers of hopping events seen. In the isolated vacancy system only the longer distance Na2-Na2 hop is available. TSS of candidate hops have shown that the activation energy for isolated vacancies is a 4-fold increase in comparison to the shorter Na2-Na1 hop. At least in the temperature range of the QENS experiment, the longer range Na2-Na2 mechanism does not play a significant role, and instead the diffusion occurs by the shorter hops. Our MD simulations show how short-range ordering of multi-vacancy clusters facilitate the hopping of ions between Na1 and Na2 sites. The presence of interconnected pathways could lead to bulk diffusion via this mechanism. Additional evidence for glassy mixtures of multi-vacancy clusters comes from Monte Carlo simulations of X-ray scattering patterns in the disordered phase. Diffuse scattering is observed between Bragg reflections, which is modelled by clustered arrangements of Na1 and Na2 ions with no long range ordering. Even at high temperature, when the diffuse scattering weakens, no change in behaviour is observed in the Arrhenius dependence of the QENS.

In the $Li_{3x}La_{2/3-x}TiO_3$ system, superstructures have been measured using single crystal X-ray diffraction. Three systems were identified, two of which had strong similarities to those mentioned in the wider literature [20]. The new structure consisted of a tetragonal cell with a Ruddlesden-Popper structure. Refinements of the diffraction patterns in all cases determined partial occupancies of La and Li on their shared site. The X-ray refinements showed TiO_6 octahedra which were distorted away from La ions. A consequence of the distortions is the widening of bottlenecks between octahedra, which have been determined to improve the Li diffusion by lowering the activation energy [175, 176]. The Ruddlesden-Popper structure opens up the possibility for new diffusion pathways which should be investigated further using experimental and computational techniques.

The commercial role of $Li_{3x}La_{2/3-x}TiO_3$ as a solid electrolyte requires a fast diffusion rate of Li. QENS measurements were carried out to compliment the existing electrochemical and computational studies in the literature. The QENS data were consistent with the hopping distance predicted in MD simulations. An Arrhenius fit to the diffusion rates determined by QENS provided a good approximation to the observed rates over the temperature range from 200 K - 780 K. A slight curvature to the temperature dependence was observed, Figure 75, which prompted a second fitting using a Vogel-Tamman-Fulcher type relationship. The fit tries to model the relaxation of bottlenecks with temperature, which enhances Li diffusion. If certain bottlenecks are thermally activated then this might result in a change from closed to open chains of hops. Bulk conductivity and atomic scale diffusion measurements are only equivalent when ionic motion is strongly correlated leading to long open hop chains. In short closed chains, hops in a direction restoring the initial state result in net diffusion ~ 0. A Nernst-Einstein factor is a convenient way to relate the degree of the correlation between hops, where a factor $\neq 1$ indicates that the mass and charge transport rates are inequivalent. At 300 K the QENS diffusion rate is larger than the corresponding conductivity measurement when a factor of 1 is used. The limiting of the diffusion to a two dimensional plane between La rich layers could limit the length of hop chains.

The measured residence time of $1.0(2) \times 10^{-9}\,\mathrm{s}$, at 300K, is on the very edge of the QENS instrument's capability. Processes are only visible if their frequency is of an equivalent magnitude to the thermal distribution of neutron velocities. New instruments with improved resolutions will allow the measurement of QE signals particularly at the onset of the diffusional processes where the broadening will always be low. Ideally this will be combined with large Q ranges improving the baseline of any dependence. An existing instrument that has only recently achieved its full potential is the direct geometry cold neutron spectrometer LET at ISIS [188]. A large position sensitive detector bank is combined with a multi-chopper system, crucially allowing the simultaneous measurement of scattering from multiple distinct incident energy pulses. This allows the simultaneous study of diffusional processes with different residence timescales. An alternative design is the upcoming indirect geometry instrument CAMEA, at SINQ, that similarly attempts to separate out different energy pulses but in this case does it by a series of analyser banks [189]. When combining QENS and bulk measurements, slight differences in synthesis methods can easily cause variations in the quality of samples resulting in unreliable comparisons. In situ methods combining conventional bulk with neutron scattering techniques allow the same sample to be measured under the same test conditions. This would allow accurate determination of correlation factors.

The QENS experiments and simulations of this thesis examine the diffusion mechanisms in prototypical battery materials from a variety of perspectives. The materials were chosen for their promising characteristics and the interest shown in them by the wider community. The QENS techniques can be applied widely to Li and Na-ion systems since both diffusing species have significant incoherent scattering cross sections. Careful selection of isotopes to avoid spin or isotope incoherence in the other ions is necessary to ensure favourable signal-to-noise ratios, but with advances in instrumentation more challenging systems with smaller samples or slower diffusion can be studied. Continual improvements in computational resources and modelling theory also increase the complexity of the systems that can be studied. Next steps for this research involve the substitution of the La site of $Li_{3x}La_{2/3-x}TiO_3$ with different lanthanides. New QENS experiments should look for connections between diffusion rate and composition, and ideally be able to relate this to the increase in hop length and size of bottlenecks. In the $Na_{0.8}CoO_2$ system, the availability of short hops was clearly favourable for diffusive motions due to the reduced activation barrier. Limitations at low temperature occurred due to the formation of superstructures. Research should be directed towards materials with the P2 structure but not the Na^+ ordering. A disordered P2 Na-TMO is created by choosing a combination of transition metal ions with very similar ionic radii but substantially different redox potentials versus Na. For example, P2-$Na_{0.6}Cr_{0.6}Ti_{0.4}O_2$ which was found to be completely disordered at any Na concentration and displayed excellent cycle performance [190]. Using isotopically pure ^{52}Cr and ^{48}Ti this compound would be an excellent candidate for a QENS experiment.

Further in the future, research needs to be directed towards completely novel systems. High throughput computational screening has allowed, amongst others, the rapid analysis of potential Li-ion cathode[191] and anode materials[192]. The most promising of the predicted systems can be selected for neutron studies to identify interesting and useful dynamic behaviour. In addition to Li and Na, other alkali metals such as K, Mg and Al are being investigated, with the advantage of better sustainable chemistries[193]. The techniques used in this thesis are ideal to investigate how the dynamics in structures change for different dynamic ions.

The techniques used are also applicable to research beyond conventional battery materials. One promising avenue for improving the characteristics of battery materials is the use of nanomaterials. For example, research on Li-ion batteries has used nanocomposites and nanometre-thick coatings to optimise ionic and electronic conduction pathways, and block undesired irreversible side reactions[194]. QENS studies of the optimised systems may lead to the greater understanding of the ionic pathways, and inform on how to further improve the nano-structured materials. Another promising avenue is flow-battery technologies which are characterised by the spatial separation of the electrolyte and the electrode; where the redox reaction usually occurs on the electrode surface and, therefore, does not rely on intercalation mechanisms which can lead to damage of the internal structure[195]. Although QENS has been applied in this thesis to study the diffusion of ions in intercalation materials; it can potentially be applied to a wide range of research, and is not restricted to solid structures. Understanding the diffusion of ions through the aqueous solution of the flow-battery and at the surface of the electrode could result in the improved stability. Furthermore, coupling studies of the ion dynamics with computational studies may help flow-battery technologies to achieve their potential.

References

[1] Tarascon, J. M. and Armand, M. *Issues and challenges facing rechargeable lithium batteries*. Nature, 414(6861):359–367, 2001.

[2] Nitta, N., Wu, F., Lee, J. T., and Yushin, G. *Li-ion battery materials: present and future*. Materials Today, 18(5):252–264, 2015.

[3] S. Hameer, J. L. V. N. *A Review of Large-Scale Electrical Energy Storage*. Int. J. Energy Res., 39:1179–1195, 2015.

[4] Kirubakaran, A., Jain, S., and Nema, R. K. *A review on fuel cell technologies and power electronic interface*. Renewable and Sustainable Energy Reviews, 13(9):2430–2440, 2009. doi:http://dx.doi.org/10.1016/j.rser.2009.04.004.

[5] Cook, B. *An Introduction to Fuel Cells and Hydrogen Technology*, pages 14–21. Heliocentris, Vancouver, Canada, third edition, 2001.

[6] Goldsmith, J., Wong-Foy, A., Cafarella, M. J., and Siegel, D. J. *Theoretical Limits of Hydrogen Storage in MetalOrganic Frameworks: Opportunities and Trade-Offs*. Chemistry of Materials, 25(16):3373–3382, 2013. doi:10.1021/cm401978e. Doi: 10.1021/cm401978e.

[7] Yaksic, A. and Tilton, J. E. *Using the cumulative availability curve to assess the threat of mineral depletion: The case of lithium*. Resources Policy, 34(4):185–194, 2009.

[8] Ebensperger, A., Maxwell, P., and Moscoso, C. *The lithium industry: Its recent evolution and future prospects*. Resources Policy, 30(3):218–231, 2005.

[9] Grosjean, C., Miranda, P. H., Perrin, M., and Poggi, P. *Assessment of world lithium resources and consequences of their geographic distribution on the expected development of the electric vehicle industry.* Renewable and Sustainable Energy Reviews, 16(3):1735–1744, 2012.

[10] Kushnir, D. and Sandn, B. A. *The time dimension and lithium resource constraints for electric vehicles.* Resources Policy, 37(1):93–103, 2012.

[11] Liu, C., Neale, Z. G., and Cao, G. *Understanding electrochemical potentials of cathode materials in rechargeable batteries.* Materials Today, 19(2):109, 2016.

[12] Goodenough, J. B. and Park, K.-S. *The Li-Ion Rechargeable Battery: A Perspective.* Journal of the American Chemical Society, 135(4):1167–1176, 2013.

[13] Delmas, C., Fouassier, C., and Hagenmuller, P. *Structural classification and properties of the layered oxides.* Physica B+C, 99(1):81–85, 1980.

[14] Winter, M., Besenhard, J. O., Spahr, M. E., and Novk, P. *Insertion Electrode Materials for Rechargeable Lithium Batteries.* Advanced Materials, 10(10):725–763, 1998.

[15] Mizushima, K., Jones, P. C., Wiseman, P. J., and Goodenough, J. B. *Li_xCoO_2 ($0<x<1$): A new cathode material for batteries of high energy density.* Materials Research Bulletin, 15(6):783–789, 1980.

[16] Ohzuku, T., Ueda, A., and Nagayama, M. *Electrochemistry and Structural Chemistry of $LiNiO_2$ ($R\bar{3}m$) for 4 Volt Secondary Lithium Cells.* Journal of the Electrochemical Society, 140(7):1862–1870, 1993.

[17] G., P. B., Armstrong, A. R., and L., R. G. *New intercalation compounds for lithium batteries: layered* $LiMnO_2$. Journal of Materials Chemistry, 9(1):193–198, 1999.

[18] Gu, M., Belharouak, I., Zheng, J., Wu, H., Xiao, J., Genc, A., Amine, K., Thevuthasan, S., Baer, D. R., Zhang, J.-G., Browning, N. D., Liu, J., and Wang, C. *Formation of the Spinel Phase in the Layered Composite Cathode Used in Li-Ion Batteries.* ACS Nano, 7(1):760–767, 2013.

[19] Quartarone, E. and Mustarelli, P. *Electrolytes for solid-state lithium rechargeable batteries: recent advances and perspectives.* Chemical Society Reviews, 40(5):2525–2540, 2011.

[20] Stramare, S., Thangadurai, V., and Weppner, W. *Lithium Lanthanum Titanates: A Review.* Chemistry of Materials, 15(21):3974–3990, 2003.

[21] Harada, Y., Ishigaki, T., Kawai, H., and Kuwano, J. *Lithium ion conductivity of polycrystalline perovskite* $La_{0.67x}Li_{3x}TiO_3$ *with ordered and disordered arrangements of the A-site ions.* Solid State Ionics, 108(14):407–413, 1998.

[22] Ivanov-Schitz, A. K., Kireev, V. V., and Chaban, N. G. *Growth and investigation of lithium-substituted perovskite-type ionic conductor.* Solid State Ionics, 136137(0):501–504, 2000.

[23] Ellis, B. L. and Nazar, L. F. *Sodium and sodium-ion energy storage batteries.* Current Opinion in Solid State and Materials Science, 16(4):168–177, 2012.

[24] Kundu, D., Talaie, E., Duffort, V., and Nazar, L. F. *The Emerging Chemistry of Sodium Ion Batteries for Electrochemical Energy Storage.* Angewandte Chemie International Edition, 54(11):3431–3448, 2015.

[25] Wang, Y., Liu, B., Li, Q., Cartmell, S., Ferrara, S., Deng, Z. D., and Xiao, J. *Lithium and lithium ion batteries for applications in microelectronic devices: A review.* Journal of Power Sources, 286:330–345, 2015.

[26] Kim, Y., Ha, K.-H., Oh, S. M., and Lee, K. T. *High-Capacity Anode Materials for Sodium-Ion Batteries.* Chemistry - A European Journal, 20(38):11980–11992, 2014.

[27] Goodenough, J. B., Hong, H. Y.-P., and Kafalas, J. A. *Fast* Na^+*-ion transport in skeleton structures.* Materials Research Bulletin, 11(2):203–220, 1976.

[28] Han, M. H., Gonzalo, E., Singh, G., and Rojo, T. *A comprehensive review of sodium layered oxides: powerful cathodes for Na-ion batteries.* Energy Environ.Sci., 8(1):81–102, 2015.

[29] Palomares, V., Serras, P., Villaluenga, I., Hueso, K. B., Carretero-Gonzalez, J., and Rojo, T. *Na-ion batteries, recent advances and present challenges to become low cost energy storage systems.* Energy Environ.Sci., 5(3):5884–5901, 2012.

[30] Wang, X., Tamaru, M., Okubo, M., and Yamada, A. *Electrode Properties of P2-*$Na_{2/3}Mn_yCo_{1-y}O_2$ *as Cathode Materials for Sodium-Ion Batteries.* The Journal of Physical Chemistry C, 117(30):15545–15551, 2013.

[31] Vassilaras, P., Toumar, A. J., and Ceder, G. *Electrochemical properties of* $NaNi_{1/3}Co_{1/3}Fe_{1/3}O_2$ *as a cathode material for Na-ion batteries.* Electrochemistry Communications, 38:79–81, 2014.

[32] Kim, D., Lee, E., Slater, M., Lu, W., Rood, S., and Johnson, C. S. *Layered* $Na[Ni_{1/3}Fe_{1/3}Mn_{1/3}]O_2$ *cathodes for Na-ion battery application.* Electrochemistry Communications, 18:66–69, 2012.

[33] Yabuuchi, N., Kajiyama, M., Iwatate, J., Nishikawa, H., Hitomi, S., Okuyama, R., Usui, R., Yamada, Y., and Komaba, S. *P2-type* $Na_xFe_{1/2}Mn_{1/2}]O_2$ *made from earth-abundant elements for rechargeable Na batteries.* Nat Mater, 11(6):512–517, 2012.

[34] Ding, J. J., Zhou, Y. N., Sun, Q., Yu, X. Q., Yang, X. Q., and Fu, Z. W. *Electrochemical properties of P2-phase Na0.74CoO2 compounds as cathode material for rechargeable sodium-ion batteries.* Electrochimica Acta, 87:388–393, 2013.

[35] D'Arienzo, M., Ruffo, R., Scotti, R., Morazzoni, F., Mari, C. M., and Polizzi, S. *Layered* $Na_{0.71}CoO_2$*: a powerful candidate for viable and high performance Na-batteries.* Physical Chemistry Chemical Physics, 14(17):5945–5952, 2012.

[36] Roger, M., Morris, D. J. P., Tennant, D. A., Gutmann, M. J., Goff, J. P., Hoffmann, J. U., Feyerherm, R., Dudzik, E., Prabhakaran, D., Boothroyd, A. T., Shannon, N., Lake, B., and Deen, P. P. *Patterning of sodium ions and the control of electrons in sodium cobaltate.* Nature, 445(7128):631–634, 2007.

[37] Jian, Z., Yu, H., and Zhou, H. *Designing high-capacity cathode materials for sodium-ion batteries.* Electrochemistry Communications, 34:215–218, 2013.

[38] Berthelot, R., Carlier, D., and Delmas, C. *Electrochemical investigation of the* $P_2Na_xCoO_2$ *phase diagram.* Nat Mater, 10(1):74–80, 2011.

[39] Shacklette, L. W., Jow, T. R., and Townsend, L. *Rechargeable Electrodes from Sodium Cobalt Bronzes.* Journal of the Electrochemical Society, 135(11):2669–2674, 1988.

[40] Pandiyan, M. S. *Phase Diagram and Control of Thermoelectric Properties of Sodium Cobaltate*, 2013.

[41] Shu, G. J. and Chou, F. C. *Sodium-ion diffusion and ordering in single-crystal P2* Na_xCoO_2. Phys.Rev.B, 78(5):052101, 2008.

[42] Molenda, J., Baster, D., Gutowska, M. U., Szewczyk, A., Puźniak, R., and Tobola, J. *Electronic origin of the step-like character of the discharge curve for* Na_xCoO_{2-y} *cathode.* Functional Materials Letters, 07(06):1440009, 2014.

[43] Shibata, T. and Wataru Kobayashi and, Y. M. *Sodium Ion Diffusion in Layered* Na_xCoO_2. Applied Physics Express, 6(9):097101, 2013.

[44] Han, S. C., Lim, H., Jeong, J., Ahn, D., Park, W. B., Sohn, K.-S., and Pyo, M. *Ca-doped* Na_xCoO_2 *for improved cyclability in sodium ion batteries.* Journal of Power Sources, 277:9–16, 2015.

[45] Beck, F. R., Cheng, Y. Q., Zhonge, B., Feygenson, M., Bridges, C. A., Moorhead-Rosenberg, Z., Manthiram, A., Goodenough, J. B., Paranthaman, M. P., and Manivannan, A. *Neutron Diffracti on and Electrochemical Studies of Na0.79CoO2and Na0.79Co0.7Mn0.3O2 Cathodes for Sodium-Ion Batteries.* Journal of the Electrochemical Society, 161(6):A961, 2014.

[46] Hempelmann, R. *Quasielastic Neutron Scattering and Solid State diffusion.* OUP Oxford, 1st edition, 2000.

[47] Haus, J. W. and Kehr, K. W. *Diffusion in regular and disordered lattices.* Physics Reports, 150(5):263–406, 1987.

[48] Eyring, H. *The Activated Complex in Chemical Reactions.* Journal of Chemical Physics, 3:107, 1935.

[49] Stearn, A. E. and Eyring, H. *Absolute Rates of Solid Reactions: Diffusion.* The Journal of physical chemistry, 44(8):955–980, 1940.

[50] Murch, G. E. *Diffusion Kinetics in Solids*, pages 171–238. Phase Transformations in Materials. Wiley-VCH Verlag GmbH & Co. KGaA, 2001; 2005. ISBN 9783527602643.

[51] Compaan, K. and Haven, Y. *Correlation factors for diffusion in solids.* Transactions of the Faraday Society, 52(0):786–801, 1956.

[52] Morgan, B. J. and Madden, P. A. *Relationships between Atomic Diffusion Mechanisms and Ensemble Transport Coefficients in Crystalline Polymorphs.* Phys.Rev.Lett., 112(14):145901, 2014.

[53] *International Tables for Crystallography Vol. A.* Springer, 5th edition edition, 2005.

[54] Burns, G. and M., A. G. *Space Groups for Solid State Scientists.* London: Academic Press, New York, 1978.

[55] Wyckoff, W. G., R. *The analytical expression of the results of the theory of space groups.* Carnegie Institution of Washington, 2nd edition, 1930.

[56] Koohpayeh, S. M., Fort, D., Bradshaw, A., and Abell, J. S. *Thermal characterization of an optical floating zone furnace: A direct link with controllable growth parameters.* Journal of Crystal Growth, 311(8):2513–2518, 2009.

[57] Uthayakumar, S., Pandiyan, M. S., Porter, D. G., Gutmann, M. J., Fan, R., and Goff, J. P. *Crystal growth and neutron diffraction studies of LixCoO2 bulk single crystals.* Journal of Crystal Growth, 401:169–172, 2014.

[58] Neutron News, 3(3):29–37, 1992.

[59] Squires, G. L. *Introduction to the theory of Thermal Neutron Scattering.* Cambridge University Press, Cambridge, 1st edition, 1978.

[60] Willis, B. T. M. and Carlile, C. J. *Experimental Neutron Scattering.* Oxford University Press, Oxford, 1st edition, 2009.

[61] Als-Nielsen, J. and McMorrow, D. *Elements of Modern X-Ray Physics.* John Wiley, 2011.

[62] Ashcroft, N. W. and Mermin, N. D. *Solid State Physics.* Harcourt, New York, 1976.

[63] Sivia, D. S. *Magnetic Form Factors*, pages 73–74. Elementary Scattering Theory: For X-ray and Neutron Users. Oxford University Press, first edition, 2011.

[64] R., J. H. and E., H. H. *Solid State Physics.* Wiley, second edition edition, 2005.

[65] Chudley, C. T. and Elliott, R. J. Proc. Phys. Soc., (77):353–361, 1961.

[66] Taylor, A. *PROGRESS at the ISIS Facility.* Physica B: Condensed Matter, 385386, Part 1:728–731, 2006.

[67] Taylor, A. *Welcome to the second target station at ISIS.* Materials Today, 11(12):72, 2008.

[68] Bennington, S. M. *Instruments on the ISIS second target station.* Nuclear Instruments and Methods in Physics Research Section A: Accelerators, Spectrometers, Detectors and Associated Equipment, 600(1):32–34, 2009.

[69] Findlay, D. J. S. *ISIS - pulsed neutron and muon source.* In *2007 IEEE Particle Accelerator Conference (PAC)*, pages 695–699. 2007. ISBN 1944-4680.

[70] Telling, M. T. F. and Andersen, K. H. *Spectroscopic characteristics of the OSIRIS near-backscattering crystal analyser spectrometer on the ISIS pulsed neutron source.* Phys.Chem.Chem.Phys., 7(6):1255–1261, 2005.

[71] *www.isis.stfc.ac.uk/images/instruments/osiris/osiris-design-6096.jpg.*

[72] Sivia, D. S. *Atomic Form Factors*, pages 71–73. Elementary Scattering Theory: For X-ray and Neutron Users. Oxford University Press, first edition edition, 2011.

[73] Fox, A. G., Maslen, E. N., and O'Keefe, M. A. *X-ray scattering*, pages 554–587. International Tables for Crystallography Volume C: Mathematical, physical and chemical tables. Wiley, 3rd edition, 2004.

[74] *Xcalibur, Gemini User Manual.* Agilent Technologies, Inc., version 2.4 edition, 2014.

[75] Giustino, F. *Many-body Schrödinger equation*, pages 19–35. Materials Modelling using Density Functional Theory. Oxford University Press, Oxford, 1st edition, 2014.

[76] Thomas, L. H. *The calculation of atomic fields.* Mathematical Proceedings of the Cambridge Philosophical Society, 23(05):542–548, 1927.

[77] Fermi, E. Zeitschrift fr Physik, 48:73, 1928.

[78] Hohenberg, P. and Kohn, W. *Inhomogeneous electron gas.* Phys.Rev., 136:B864–B871, 1964.

[79] Yang, W. *Preface: Special Topic on Advances in Density Functional Theory.* The Journal of chemical physics, 140(18):18A101, 2014.

[80] Clark, S. J., Segall, M. D., Pickard, C. J., Hasnip, P. J., Probert, M. J., Refson, K., and Payne, M. C. *First principles methods using CASTEP*. Z.Kristall., 220:567–570, 2005.

[81] Hartree, D. R. *The Wave Mechanics of an Atom with a Non-Coulomb Central Field. Part I. Theory and Methods*. Mathematical Proceedings of the Cambridge Philosophical Society, 24(01):89–110, 1928.

[82] Hartree, D. R. *The Wave Mechanics of an Atom with a Non-Coulomb Central Field. Part II. Some Results and Discussion*. Mathematical Proceedings of the Cambridge Philosophical Society, 24(01):111–132, 1928.

[83] Slater, J. C. *The Theory of Complex Spectra*. Phys.Rev., 34(10):1293–1322, 1929.

[84] Kohn, W. and Sham, L. J. *Self-consistent equations including exchange and correlation effects*. Phys.Rev., 140:A1133–A1138, 1965.

[85] Ceperley, D. M. and Alder, B. J. *Ground State of the Electron Gas by a Stochastic Method*. Phys.Rev.Lett., 45(7):566–569, 1980.

[86] Jones, R. O. and Gunnarsson, O. *The density functional formalism, its applications and prospects*. Rev.Mod.Phys., 61(3):689–746, 1989.

[87] Almbladh, C. O. and Pedroza, A. C. *Density-functional exchange-correlation potentials and orbital eigenvalues for light atoms*. Phys.Rev.A, 29(5):2322–2330, 1984.

[88] Becke, A. D. *Density-functional exchange-energy approximation with correct asymptotic behavior*. Phys.Rev.A, 38(6):3098–3100, 1988.

[89] Mattsson, A. E., Schultz, P. A., Desjarlais, M. P., Mattsson, T. R., and Leung, K. *Designing meaningful density functional theory calculations in materials sciencea primer*. Modelling and Simulation in Materials Science and Engineering, 13(1):R1, 2005.

[90] Langreth, D. C. and Perdew, J. P. *Theory of nonuniform electronic systems. I. Analysis of the gradient approximation and a generalization that works.* Phys.Rev.B, 21(12):5469–5493, 1980.

[91] Perdew, J. P., Burke, K., and Ernzerhof, M. *Generalized Gradient Approximation Made Simple.* Phys.Rev.Lett., 77(18):3865–3868, 1996.

[92] Perdew, J. P. and Schmidt, K. *Jacobs ladder of density functional approximations for the exchange-correlation energy.* AIP Conference Proceedings, 577(1):1–20, 2001.

[93] Monkhorst, H. J. and Pack, J. D. *Special points for Brillouin-zone integrations.* Phys.Rev.B, 13(12):5188–5192, 1976.

[94] Payne, M. C., Teter, M. P., Allan, D. C., Arias, T. A., and Joannopoulos, J. D. *Iterative minimization techniques for ab initio total-energy calculations - molecular-dynamics and conjugate gradients.* Rev.Mod.Phys., 64:1045–1097, 1992.

[95] Cooley, J. W. and Tukey, J. W. *An Algorithm for the Machine Calculation of Complex Fourier Series.* Mathermatics of Computation, 19(90):297–301, 1965.

[96] Cooley, J., Lewis, P., and Welch, P. *Historical notes on the fast Fourier transform.* IEEE Transactions on Audio and Electroacoustics, 15(2):76–79, 1967.

[97] Lewis, G. N. *THE ATOM AND THE MOLECULE.* Journal of the American Chemical Society, 38(4):762–785, 1916.

[98] Phillips, J. C. and Kleinman, L. *New Method for Calculating Wave Functions in Crystals and Molecules.* Phys.Rev., 116(2):287–294, 1959.

[99] Giustino, F. *Pseudopotentials*, pages 258–263. Materials Modelling using Density Functional Theory. Oxford University Press, Oxford, 1st edition, 2014.

[100] Garrity, K. F., Bennett, J. W., Rabe, K. M., and Vanderbilt, D. *Pseudopotentials for high-throughput DFT calculations.* Computational Materials Science, 81:446–452, 2014.

[101] Hasnip, P. J., Refson, K., Probert, M. I. J., Yates, J. R., Clark, S. J., and Pickard, C. J. *Density functional theory in the solid state.* Philosophical Transactions of the Royal Society of London A: Mathematical, Physical and Engineering Sciences, 372(2011), 2014.

[102] Kresse, G. and Furthmüller, J. *Efficient iterative schemes for ab initio total-energy calculations using a plane-wave basis set.* Phys.Rev.B, 54(16):11169–11186, 1996.

[103] Marzari, N., Vanderbilt, D., and Payne, M. C. *Ensemble Density-Functional Theory for Ab Initio Molecular Dynamics of Metals and Finite-Temperature Insulators.* Phys.Rev.Lett., 79(7):1337–1340, 1997.

[104] Hellmann, H. Zeitschrift fr Physik, 85:180, 1933.

[105] Feynman, R. P. *Forces in Molecules.* Phys.Rev., 56(4):340–343, 1939.

[106] Pfrommer, B. G., Ct, M., Louie, S. G., and Cohen, M. L. *Relaxation of Crystals with the Quasi-Newton Method.* Journal of Computational Physics, 131(1):233–240, 1997.

[107] Byrd, R. H., Nocedal, J., and Schnabel, R. B. *Representations of quasi-Newton matrices and their use in limited memory methods.* Math.Prog., 63:129–156, 1994.

[108] Henkelman, G. and Jnsson, H. *Improved tangent estimate in the nudged elastic band method for finding minimum energy paths and saddle points.* The Journal of chemical physics, 113(22):9978–9985, 2000.

[109] Halgren, T. A. and Lipscomb, W. N. *The synchronous-transit method for determining reaction pathways and locating molecular transition states.* Chemical Physics Letters, 49(2):225–232, 1977.

[110] Govind, N., Petersen, M., Fitzgerald, G., King-Smith, D., and Andzelm, J. *A generalized synchronous transit method for transition state location.* Computational Materials Science, 28(2):250–258, 2003.

[111] Govind, N., Petersen, M., Fitzgerald, G., King-Smith, D., and Andzelm, J. *A generalized synchronous transit method for transition state location.* Computational Materials Science, 28(2):250–258, 2003.

[112] Verlet, L. *Computer Experiments on Classical Fluids. I. Thermodynamical Properties of Lennard-Jones Molecules.* Phys.Rev., 159(1):98–103, 1967.

[113] Petrenko, R. and Meller, J. *Molecular Dynamics.* Encyclopedia of Life Sciences. John Wiley & Sons, Ltd, 2001.

[114] Car, R. and Parrinello, M. *Unified Approach for Molecular Dynamics and Density-Functional Theory.* Phys.Rev.Lett., 55(22):2471–2474, 1985.

[115] Barnett, R. N., Landman, U., Nitzan, A., and Rajagopal, G. *BornOppenheimer dynamics using densityfunctional theory: Equilibrium and fragmentation of small sodium clusters.* The Journal of chemical physics, 94(1):608–616, 1991.

[116] Gibson, D. A., Ionova, I. V., and Carter, E. A. *A comparison of CarParrinello and BornOppenheimer generalized valence bond molecular dynamics.* Chemical Physics Letters, 240(4):261–267, 1995.

[117] Arias, T. A., Payne, M. C., and Joannopoulos, J. D. *Ab initio molecular dynamics: Analytically continued energy functionals and insights into iterative solutions.* Phys.Rev.Lett., 69(7):1077–1080, 1992.

[118] Alf, D. *Ab initio molecular dynamics, a simple algorithm for charge extrapolation.* Computer Physics Communications, 118(1):31–33, 1999.

[119] Chandrasekhar, S. *Stochastic Problems in Physics and Astronomy.* Rev.Mod.Phys., 15(1):1–89, 1943.

[120] Nos, S. *A molecular dynamics method for simulations in the canonical ensemble.* Molecular Physics, 52(2):255–268, 1984.

[121] Voneshen, D. J., Refson, K., Borissenko, E., Krisch, M., Bosak, A., Piovano, A., Cemal, E., Enderle, M., Gutmann, M. J., Hoesch, M., Roger, M., Gannon, L., Boothroyd, A. T., Uthayakumar, S., Porter, D. G., and Goff, J. P. *Suppression of thermal conductivity by rattling modes in thermoelectric sodium cobaltate.* Nat Mater, 12(11):1028–1032, 2013.

[122] Foo, M. L., Wang, Y., Watauchi, S., Zandbergen, H. W., He, T., Cava, R. J., and Ong, N. P. *Charge Ordering, Commensurability, and Metallicity in the Phase Diagram of the Layered* Na_xCoO_2. Phys.Rev.Lett., 92(24):247001, 2004.

[123] Takada, K., Sakurai, H., Takayama-Muromachi, E., Izumi, F., Dilanian, R. A., and Sasaki, T. *Superconductivity in two-dimensional* CoO_2 *layers.* Nature, 422(6927):53–55, 2003.

[124] Lei, Y., Li, X., Liu, L., and Ceder, G. *Synthesis and Stoichiometry of Different Layered Sodium Cobalt Oxides.* Chemistry of Materials, 26(18):5288–5296, 2014.

[125] Wang, Y., Ding, Y., and Ni, J. *Ground-state phase diagram of* Na_xCoO_2*: correlation of Na ordering with* CoO_2 *stacking sequences.* Journal of Physics: Condensed Matter, 21(3):035401, 2009.

[126] Balsys, R. J. and Davis, R. L. *Refinement of the structure of* $Na_{0.74}CoO_2$ *using neutron powder diffraction.* Solid State Ionics, 93(34):279–282, 1997.

[127] Morris, D. J. P. *Sodium Ordering and the Control of Properties in Sodium Cobaltate*, 2007.

[128] Morris, D. J. P., Roger, M., Gutmann, M. J., Goff, J. P., Tennant, D. A., Prabhakaran, D., Boothroyd, A. T., Dudzik, E., Feyerherm, R., Hoffmann, J. U., and Kiefer, K. *Crystal-to-stripe reordering of sodium ions in* Na_xCoO_2*,* $x \sim 0.75$*.* Phys.Rev.B, 79(10):100103, 2009.

[129] Weller, M., Sacchetti, A., Ott, H. R., Mattenberger, K., and Batlogg, B. *Melting of the Na Layers in Solid* $Na_{0.8}CoO_2$*.* Phys.Rev.Lett., 102(5):056401, 2009.

[130] Carlier, D., Blangero, M., Menetrier, M., Pollet, M., Doumerc, J.-P., and Delmas, C. *Sodium Ion Mobility in* Na_xCoO_2 *(*$0.6<x<0.75$*) Cobaltites Studied by* ^{23}Na *MAS NMR.* Inorganic chemistry, 48(15):7018–7025, 2009.

[131] Medarde, M., Mena, M., Gavilano, J. L., Pomjakushina, E., Sugiyama, J., Kamazawa, K., Pomjakushin, V. Y., Sheptyakov, D., Batlogg, B., Ott, H. R., nsson, M. M., and Juranyi, F. *1D to 2D* Na^+ *Ion Diffusion Inherently Linked to Structural Transitions in* $Na_{0.7}CoO_2$*.* Phys.Rev.Lett., 110(26):266401, 2013.

[132] Yang, H. X., Nie, C. J., Shi, Y. G., Yu, H. C., Ding, S., Liu, Y. L., Wu, D., Wang, N. L., and Li, J. Q. *Structural phase transitions and sodium ordering in* $Na_{0.5}CoO_2$*: a combined electron diffraction and Raman spectroscopy study.* Solid State Communications, 134(6):403–408, 2005.

[133] Zandbergen, H. W., Foo, M., Xu, Q., Kumar, V., and Cava, R. J. *Sodium ion ordering in* Na_xCoO_2*: Electron diffraction study.* Phys.Rev.B, 70(2):024101, 2004.

[134] Chou, F. C., Chu, M. W., Shu, G. J., Huang, F. T., Pai, W. W., Sheu, H. S., and Lee, P. A. *Sodium Ion Ordering and Vacancy Cluster Formation in* Na_xCoO_2 *(*$x = 0.71$ *and 0.84) Single Crystals by Synchrotron X-Ray Diffraction.* Phys.Rev.Lett., 101(12):127404, 2008.

[135] Huang, F. T., Chu, M. W., Shu, G. J., Sheu, H. S., Chen, C. H., Liu, L. K., Lee, P. A., and Chou, F. C. *X-ray and electron diffraction studies of superlattices and long-range three-dimensional Na ordering in* $\gamma-Na_xCoO_2$ *(x=0.71 and 0.84).* Phys.Rev.B, 79(1):014413, 2009.

[136] Zhang, P., Capaz, R. B., Cohen, M. L., and Louie, S. G. *Theory of sodium ordering in* Na_xCoO_2. Phys.Rev.B, 71(15):153102, 2005.

[137] Hinuma, Y., Meng, Y. S., and Ceder, G. *Temperature-concentration phase diagram of* $P2 - Na_xCoO_2$ *from first-principles calculations.* Phys.Rev.B, 77(22):224111, 2008.

[138] Porter, D. G. *Personal communication*, 2016. Diamond, Rutherford Appleton Laboratory.

[139] Porter, D. G. *Control of Electrons through Patterning of Superstructures in Sodium Cobaltate*, 2012.

[140] Porter, D. G., Roger, M., Gutmann, M. J., Uthayakumar, S., Prabhakaran, D., Boothroyd, A. T., Pandiyan, M. S., and Goff, J. P. *Divacancy superstructures in thermoelectric calcium-doped sodium cobaltate.* Phys.Rev.B, 90(5):054101, 2014.

[141] Lee, D. H., Xu, J., and Meng, Y. S. *An advanced cathode for Na-ion batteries with high rate and excellent structural stability.* Physical Chemistry Chemical Physics, 15(9):3304–3312, 2013.

[142] Mo, Y., Ping, S. O., and Ceder, G. *Insights into Diffusion Mechanisms in P2 Layered Oxide Materials by First-Principles Calculations.* Chemistry of Materials, 26(18):5208–2214, 2014.

[143] Tada, M., Yoshiya, M., and Yasuda, H. *Derivation of Interatomic Potentials from Ab-initio Calculations for Molecular Dynamics Simulations of* Na_xCoO_2. Transactions of the Materials Research Society of Japan, 35(2):205–208, 2010.

[144] Li, G., Yue, X., Luo, G., and Zhao, J. *Electrode potential and activation energy of sodium transition-metal oxides as cathode materials for sodium batteries: A first-principles investigation.* Computational Materials Science, 106:15–22, 2015.

[145] Okubo, M., Tanaka, Y., Zhou, H., Kudo, T., and Honma, I. *Determination of Activation Energy for Li Ion Diffusion in Electrodes.* The Journal of Physical Chemistry B, 113(9):2840–2847, 2009.

[146] der Ven, A. V., Ceder, G., Asta, M., and Tepesch, P. D. *First-principles theory of ionic diffusion with nondilute carriers.* Phys.Rev.B, 64(18):184307, 2001.

[147] Su, J., Pei, Y., Yang, Z., and Wang, X. *First-principles investigation on crystal, electronic structures and Diffusion barriers of* $NaNi_{1/3}Co_{1/3}Mn_{1/3}O_2$ *for ad-*

vanced rechargeable Na-ion batteries. Computational Materials Science, 98:304–310, 2015.

[148] Roy, S. and Kumar, P. P. *Influence of Cationic ordering on ion transport in NASICONs: Molecular dynamics study.* Solid State Ionics, 253:217–222, 2013.

[149] Sau, K. and Kumar, P. P. *Ion Transport in $Na_2M_2TeO_6$: Insights from Molecular Dynamics Simulation.* The Journal of Physical Chemistry C, 119(4):1651–1658, 2015.

[150] Sau, K. and Kumar, P. P. *Role of Ion-Ion Correlations on Fast Ion Transport: Molecular Dynamics Simulation of $Na_2Ni_2TeO_6$.* The Journal of Physical Chemistry C, 119(32):18030–18037, 2015.

[151] Bo, S.-H., Wang, Y., Kim, J. C., Richards, W. D., and Ceder, G. *Computational and Experimental Investigations of Na-Ion Conduction in Cubic Na_3PSe_4.* Chemistry of Materials, 28(1):252–258, 2016.

[152] Jalem, R., Natsume, R., Nakayama, M., and Kasuga, T. *First-Principles Investigation of the Na^+ Ion Transport Property in Oxyfluorinated Titanium(IV) Phosphate $Na_3Ti_2P_2O_{10}F$.* The Journal of Physical Chemistry C, 120(3):1438–1445, 2016.

[153] Shakourian-Fard, M., Kamath, G., Smith, K., Xiong, H., and Sankaranarayanan, S. K. R. S. *Trends in Na-Ion Solvation with Alkyl-Carbonate Electrolytes for Sodium-Ion Batteries: Insights from First-Principles Calculations.* The Journal of Physical Chemistry C, 119(40):22747–22759, 2015.

[154] Voneshen, D. J. *Private communication*, 2015. ISIS, Rutherford Appleton Laboratory.

[155] Juranyi, F., Månsson, M., Gavilano, J. L., Mena, M., Pomjakushina, E., Medarde, M., Sugiyama, J., Kamazawa, K., Batlogg, B., Ott, H. R., and Seydel, T. *Dynamics across the structural transitions at elevated temperatures in* $Na_{0.7}CoO_2$. EPJ Web of Conferences, 83:02008,, 2015.

[156] Uthayakumar, S. *Private communication*, 2013. Royal Holloway, University of London.

[157] Arnold, O., Bilheux, J. C., Borreguero, J. M., Buts, A., Campbell, S. I., Chapon, L., Doucet, M., Draper, N., Leal, R. F., Gigg, M. A., Lynch, V. E., Markvardsen, A., Mikkelson, D. J., Mikkelson, R. L., Miller, R., Palmen, K., Parker, P., Passos, G., Perring, T. G., Peterson, P. F., Ren, S., Reuter, M. A., Savici, A. T., Taylor, J. W., Taylor, R. J., Tolchenov, R., Zhou, W., and Zikovsky, J. *Mantid-Data analysis and visualization package for neutron scattering and SR experiments.* Nuclear Instruments and Methods in Physics Research Section A: Accelerators, Spectrometers, Detectors and Associated Equipment, 764:156–166, 2014.

[158] Fallahzadeh, R. and Farhadian, N. *Molecular dynamics simulation of lithium ion diffusion in LiCoO2 cathode material.* Solid State Ionics, 280:10–17, 2015. doi:http://dx.doi.org/10.1016/j.ssi.2015.07.001.

[159] Jak, M. J. G., Verhoeven, V. W. J., de Schepper, I. M., Mulder, F. M., Kelder, E. M., and Schoonman, J. *Neutron and X-ray scattering on Li-doped* BPO_4. Physica B: Condensed Matter, 266(12):108–111, 1999.

[160] Myrdal, J. S. G., Blanchard, D., Sveinbjrnsson, D., and Vegge, T. *Li-ion Conduction in the* $LiBH_4$*:LiI System from Density Functional Theory Calculations and Quasi-Elastic Neutron Scattering.* The Journal of Physical Chemistry C, 117(18):9084–9091, 2013.

[161] Nozaki, H., Harada, M., Ohta, S., Watanabe, I., Miyake, Y., Ikedo, Y., Jalarvo, N. H., Mamontov, E., and Sugiyama, J. *Li diffusive behavior of garnet-type oxides studied by muon-spin relaxation and QENS.* Solid State Ionics, 262:585–588, 2014.

[162] Inaguma, Y., Liquan, C., Itoh, M., Nakamura, T., Uchida, T., Ikuta, H., and Wakihara, M. *High ionic conductivity in lithium lanthanum titanate.* Solid State Communications, 86(10):689–693, 1993.

[163] Bohnke, O., Bohnke, C., and Fourquet, J. L. *Mechanism of ionic conduction and electrochemical intercalation of lithium into the perovskite lanthanum lithium titanate.* Solid State Ionics, 91(12):21–31, 1996.

[164] Shannon, R. D. *Revised effective ionic radii and systematic studies of interatomic distances in halides and chalcogenides.* Acta Crystallographica Section A, 32(5):751–767, 1976.

[165] Inaguma, Y., Chen, L., Itoh, M., and Nakamura, T. *Candidate compounds with perovskite structure for high lithium ionic conductivity.* Solid State Ionics, 70:196–202, 1994.

[166] Itoh, M., Inaguma, Y., Jung, W.-H., Chen, L., and Nakamura, T. *High lithium ion conductivity in the perovskite-type compounds* $Ln_{1/2}Li_{1/2}TiO_3$ *(Ln=La,Pr,Nd,Sm).* Solid State Ionics, 70:203–207, 1994.

[167] Harada, Y., Hirakoso, Y., Kawai, H., and Kuwano, J. *Orderdisorder of the A-site ions and lithium ion conductivity in the perovskite solid solution* $La_{0.67x}Li_{3x}TiO_3$ *(x=0.11).* Solid State Ionics, 121(14):245–251, 1999.

[168] Harada, Y., Ishigaki, T., Kawai, H., and Kuwano, J. *Lithium ion conductivity of polycrystalline perovskite* $La_{0.67x}Li_{3x}TiO_3$ *with ordered and disordered arrangements of the A-site ions.* Solid State Ionics, 108(14):407–413, 1998.

[169] Ruiz, A. I., Lpez, M. L., Veiga, M. L., and Pico, C. *Electrical properties of* $La_{1.33x}Li_{3x}Ti_2O_6$ *(0.1<x<0.3).* Solid State Ionics, 112(34):291–297, 1998.

[170] Ibarra, J., Várez, A., Len, C., Santamara, J., Torres-Martnez, L. M., and Sanz, J. *Influence of composition on the structure and conductivity of the fast ionic conductors* $La_{2/3x}Li_{3x}TiO_3$ *(0.03<x<0.167).* Solid State Ionics, 134(34):219–228, 2000.

[171] Bhuvanesh, N. S. P., Bohnk, O., Duroy, H., Crosnier-Lopez, M. P., Emery, J., and Fourquet, J. L. *Topotactic* H^+/Li^+ *ion exchange on* $La_{2/3x}Li_{3x}TiO_3$*: new metastable perovskite phases* $La_{2/3x}TiO_{33x}(OH)_{3x}$ *and* $La_{2/3x}TiO_{33x/2}$ *obtained by further dehydration.* Materials Research Bulletin, 33(11):1681–1691, 1998.

[172] Fourquet, J. L., Duroy, H., and Crosnier-Lopez, M. P. *Structural and Microstructural Studies of the Series* $La_{2/3x}Li_{3x}\square_{1/32x}TiO_3$. Journal of Solid State Chemistry, 127(2):283–294, 1996.

[173] Bohnke, O., Duroy, H., Fourquet, J.-L., Ronchetti, S., and Mazza, D. *In search of the cubic phase of the* Li^+ *ion-conducting perovskite* $La_{2/3x}Li_{3x}TiO_3$*: structure and properties of quenched and in situ heated samples.* Solid State Ionics, 149(34):217–226, 2002.

[174] Inaguma, Y., Katsumata, T., Itoh, M., and Morii, Y. *Crystal Structure of a Lithium Ion-Conducting Perovskite* $La_{2/3x}Li_{3x}TiO_3$ *(x=0.05).* Journal of Solid State Chemistry, 166(1):67–72, 2002.

[175] Bohnke, O. *The fast lithium-ion conducting oxides* $Li_{3x}La_{2/3-x}TiO_3$ *from fundamentals to application.* Solid State Ionics, 179(16):9–15, 2008.

[176] Šalkus, T., Kazakeviius, E., Kežionis, A., Orliukas, A. F., Badot, J. C., and Bohnke, O. *Determination of the non-Arrhenius behaviour of the bulk conductivity of fast ionic conductors LLTO at high temperature.* Solid State Ionics, 188(1):69–72, 2011.

[177] Mori, K., Tomihira, S., Iwase, K., and Fukunaga, T. *Visualization of conduction pathways in a lanthanum lithium titanate superionic conductor synthesized by rapid cooling.* Solid State Ionics, 268, Part A:76–81, 2014.

[178] h Chen, C. and Du, J. *Lithium Ion Diffusion Mechanism in Lithium Lanthanum Titanate Solid-State Electrolytes from Atomistic Simulations.* Journal of the American Ceramic Society, 98(2):534, 2015.

[179] Jay, E. E., Rushton, M. J. D., Chroneos, A., Grimes, R. W., and Kilner, J. A. *Genetics of superionic conductivity in lithium lanthanum titanates.* Physical Chemistry Chemical Physics, 17(1):178–183, 2015.

[180] Inaguma, Y., Yu, J., Katsumata, T., and Itoh, M. *Lithium Ion Conductivity in a Perovskite Lanthanum Lithium Titanate Single Crystal.* Journal of the Ceramic Society of Japan, 105(1222):548–550, 1997.

[181] Moriwake, H., Gao, X., Kuwabara, A., Fisher, C. A. J., Kimura, T., Ikuhara, Y. H., Kohama, K., Tojigamori, T., and Ikuhara, Y. *Domain boundaries and their influence on Li migration in solid-state electrolyte (La,Li)*TiO_3. Journal of Power Sources, 276:203–207, 2015.

[182] Ruddlesden, S. N. and Popper, P. *The compound* $Sr_3Ti_2O_7$ *and its structure.* Acta Crystallographica, 11(1):54–55, 1958.

[183] Beznosikov, B. V. and Aleksandrov, K. S. *Perovskite-like crystals of the Ruddlesden-Popper series.* Crystallography Reports, 45(5):792–798, 2000.

[184] Rivera, A., Santamara, J., Leon, C., Blochowicz, T., Gainaru, C., and Rossler, A. *Temperature dependence of the ionic conductivity in* $Li_{3x}La_{2/3-x}TiO_3$ *: Arrhenius versus non-Arrhenius.* Applied Physics Letters, 82(15):2425, 2003.

[185] Geng, H., Lan, J., Mei, A., Lin, Y., and Nan, C. W. *Effect of sintering temperature on microstructure and transport properties of* $Li_{3x}La_{2/3x}TiO_3$ *with different lithium contents.* Electrochimica Acta, 56(9):3406–3414, 2011.

[186] Katsumata, T., Inaguma, Y., Itoh, M., and Kawamura, K. *Molecular Dynamics Simulations of the High Lithium Ion Conductor.* $La_{0.6}Li_{0.2}TiO_3$. Journal of the Ceramic Society of Japan, 107(7):615, 1999.

[187] Katsumata, T., Inaguma, Y., Itoh, M., and Kawamura, K. *Influence of Covalent Character on High Li Ion Conductivity in a Perovskite-Type Li Ion Conductor: Prediction from a Molecular Dynamics Simulation of* $La_{0.6}Li_{0.2}TiO_3$. Chemistry of Materials, 14(9):3930–3936, 2002.

[188] Bewley, R. I., Taylor, J. W., and Bennington., S. M. *LET, a cold neutron multi-disk chopper spectrometer at ISIS.* Nuclear Instruments and Methods in Physics Research Section A: Accelerators, Spectrometers, Detectors and Associated Equipment, 637(1):128–134, 2011.

[189] Groitl, F., Graf, D., Birk, J. O., Mark, M., Bartkowiak, M., Filges, U., Niedermayer, C., Regg, C., and Rnnow, H. M. *CAMEA—A novel multiplexing analyzer for neutron spectroscopy.* Review of Scientific Instruments, 87(3):035109, 2016.

[190] Wang, Y., Xiao, R., Hu, Y.-S., Avdeev, M., and Chen, L. *P2-*$Na_{0.6}[Cr_{0.6}Ti_{0.4}]O_2$ *cation-disordered electrode for high-rate symmetric rechargeable sodium-ion batteries.* Nat Commun, 6, 2015.

[191] Hautier, G., Jain, A., Chen, H., Moore, C., Ong, S. P., and Ceder, G. *Novel mixed polyanions lithium-ion battery cathode materials predicted by high-throughput ab initio computations.* Journal of Materials Chemistry, 21(43):17147–17153, 2011. doi:10.1039/C1JM12216A.

[192] Kirklin, S., Meredig, B., and Wolverton, C. *High-Throughput Computational Screening of New Li-Ion Battery Anode Materials.* Advanced Energy Materials, 3(2):252–262, 2013. doi:10.1002/aenm.201200593.

[193] Chu, S., Cui, Y., and Liu, N. *The path towards sustainable energy.* Nat Mater, 16(1):16–22, 2017.

[194] Lu, J., Chen, Z., Ma, Z., Pan, F., Curtiss, L. A., and Amine, K. *The role of nanotechnology in the development of battery materials for electric vehicles.* Nat Nano, 11(12):1031–1038, 2016.

[195] Park, M., Ryu, J., Wang, W., and Cho, J. *Material design and engineering of next-generation flow-battery technologies.* Nature Reviews Materials, 2:16080, 2016.